University of Nottingham
UK | CHINA | MALAYSIA

MULTIPHASE AND MULTICOMPONENT FLOWS SIMULATION USING MESOSCALE METHOD

Wei Gong, BEng.

Thesis submitted to University of Nottingham for the degree of

Doctor of Philosophy

September 2019

Abstract

The main work in this thesis is to use lattice Boltzmann (LB) method to solve multiphase and multi-component problems in mesoscale. The practical problems include water droplet wetting states transitions, oil droplets motions in water under electric field, and three stages of boiling. Besides, a multi-bubble/droplet coexistence problem for single component multiphase (SCMP) LB model has also been investigated.

In the wetting transition work, the free energy curves based on the transition processes are presented and discussed in detail. The existence of energy barriers with or without consideration of the gravity effect, and the irreversibility of wetting transition are discussed based on the presented energy curves. The energy curves show that different routes of the Cassie-to-Wenzel transition and the reverse transition are the main reason for the irreversibility. Numerical simulations are implemented via a phase field LB method of large density ratio, and the simulation results show good consistency with the theoretical analysis. Through the numerical analysis, the proposed energy curves can be verified to a great degree, and it verifies that the Wenzel-to-Cassie transition can happen spontaneously without any external forces if the intrinsic Young's angle is large enough. Besides, the critical state energy in the energy curves can be increased by modifying the micro posts to achieve a much better super-hydrophobicity.

In the oil-in-water work, a multi-component multiphase (MCMP) LB model is proposed by coupling the LB scheme electrostatic field equation to simulate oil droplets motions in water under electrostatic field. Single water droplet deformation and double water droplets attracting each other in oil under strong electric field are accomplished using this model. The numerical simulation results are compared with

previous experiment results and it shows a good agreement between them, which means the proposed model is eligible to be used to study the dielectrophoresis force effect on oil/water separation. The dielectrophoresis force effect on oil droplets in water is studied. The result shows that dielectrophoresis force has effect on oil droplets in water under weak electric field and it can promote the oil droplets coalescence, which can be helpful for down-hole oil water separation (DOWS) in a hydrocyclone. Experiment study has also been carried out, however, the dielectrophoresis force effect is not observed due to devices constraints and the quite weak dielectrophoresis force. Nevertheless, the electroosmosis phenomenon is observed in the experiment and it drives the oil droplets moving in an ordered way.

In the boiling work, a modified improved SCMP LB model for phase change heat transfer is proposed. The boiling phenomenon in three stages: nucleate boiling, transition boiling and film boiling are accomplished using LB model. The numerical model is validated with liquid-vapour coexistent densities, D^2 law for droplets evaporation as well as the three boiling stages. Compared with the original pseudopotential phase change model, the modified model has a better accuracy and can be used to study phase change physics problems including evaporation and boiling heat transfer.

In the multi-bubble/droplet coexistence problem work, the thermal immiscible multiphase flow simulation using pseudopotential LB method is studied. The results show that it is difficult to achieve multi-bubble/droplet coexistence due to a mass transfer phenomenon of “the big eat the small” – the small bubbles/droplets disappear and the big ones getting bigger before a physical coalescence when using an internal energy-based temperature equation for single component multiphase (SCMP)

pseudopotential models. In the present study, the mass transfer phenomenon between vapour phase and liquid phase is investigated, and the possible reason is explored. It is found that there is a spurious flow field formed between two bubbles or droplets with different shapes, and such flow field is exactly the transfer of high-density mass. In addition, it is found that the curvatures of the interfaces determine the direction of the spurious flow field, and for the definition of "the big eat the small", "the big" refers to the interfaces that have larger radii of curvature while "the small" represents the interfaces with smaller radii of curvature. MCMP LBM is also tested in this work and it is found to be free of the unphysical mass transfer. In addition, this unphysical effect can be effectively impeded by coupling an entropy-based temperature field, and the influence on density fields with different energy equations are discussed. This work gives a significant inspiration for solving the mass transfer problem between two phases, which determines whether the SCMP LB model can be used for multi-bubble/droplet systems.

List of Publications during PhD Study

1. Gong W, Yan Y. Investigation of electric field effect on oil-in-water using mesoscale method. Journal of Petroleum Science and Engineering. (under preparation)
2. Gong, Wei, et al. "Local Heat Transfer Characteristic Coincidence in Helically Coiled Tubes Under Different Heating Conditions." Heat Transfer Engineering (2019): 1-9.
3. Gong, Wei, and Yuying Yan. "Advances in modelling of boiling heat transfer using mesoscale method." International Heat Transfer Conference Digital Library. Begel House Inc., 2018.
4. Chen, S., Yang, B., Gong, W., & Yan, Y. (2018). Sedimentation behaviour of two non-isothermal spheres. In International Heat Transfer Conference Digital Library. Begel House Inc.
5. Gong W, Yan Y Y, Chen S, et al. A modified phase change pseudopotential lattice Boltzmann model [J]. International Journal of Heat and Mass Transfer, 2018, 125: 323-329.
6. Chen S, Gong W, Yan Y. Conjugate natural convection heat transfer in an open-ended square cavity partially filled with porous media [J]. International Journal of Heat and Mass Transfer, 2018, 124: 368-380.
7. Gong W, Yan Y, Chen S. A study on the unphysical mass transfer of SCMP pseudopotential LBM [J]. International Journal of Heat and Mass Transfer, 2018, 123: 815-820.
8. Gong W, Chen S, Yan Y. A thermal immiscible multiphase flow simulation by lattice Boltzmann method [J]. International Communications in Heat and Mass Transfer, 2017, 88: 136-138.

9. Gong W, Yan Y, Chen S, et al. Numerical study of wetting transitions on biomimetic surfaces using a lattice Boltzmann approach with large density ratio[J]. Journal of Bionic Engineering, 2017, 14(3): 486-496.
10. Chen S, Yan Y Y, Gong W. A simple lattice Boltzmann model for conjugate heat transfer research [J]. International Journal of Heat and Mass Transfer, 2017, 107: 862-870.
11. Misurati K A, Quan Y, Gong W*, et al. Contrastive study of flow and heat transfer characteristics in a helically coiled tube under uniform heating and one-side heating [J]. Applied Thermal Engineering, 2017, 114: 77-84.
12. Gong W, Zu Y, Chen S, et al. Wetting transition energy curves for a droplet on a square-post patterned surface [J]. Science bulletin, 2017, 62(2): 136-142.

Acknowledgement

First of all, I would like to express my sincere gratitude to my supervisor, Prof. Yuying Yan for his support for my PhD study. Without his help, this thesis would not be finished. He supported me to apply for the PhD candidate position, the China Scholarship Council (CSC) scholarship the FROG scholarship from Faculty of Engineering, University of Nottingham to sort out my financial issue. Moreover, he initialled my PhD research and helped me in all the work I have done with his kind advice and patience.

Besides, I would also like to thank Dr Sheng Chen for his help on lattice Boltzmann method, and the technicians and my colleagues in Fluids and Thermal Engineering Research Group for their timely support and encouragement.

Thanks would also be given to my friends in Nottingham, from whom I got a better and more colourful life when studying abroad in UK.

In addition, the financial supports from China Scholarship Council and Faculty of Engineering, University of Nottingham are gratefully acknowledged as well.

Finally, I would like to thank my parents, parents in law and all others in my family for their sincere support and advice, and my beloved wife Anqi Liu, for her love, support and encouragement during my PhD study.

Table of Contents

List of Figures

List of Tables

Nomenclature

Symbol	Meaning	SI unit
a	post width	m
$\boldsymbol{a}_c$	acceleration	$\mathrm{m} \cdot \mathrm{s}^{-2}$
B_0	electromagnetic field strength unit	-
c	lattice constant	-
c_s	lattice sound speed	-
c_v	specific heat	$\mathrm{J} \cdot \mathrm{m}^{-3} \cdot \mathrm{K}^{-1}$
$\mathbf{c}$	unit vector	-
d	post spacing	m
d'	intermediate dry spacing	m
D	spatial dimension	-
D_i	interface thickness	m
$\mathbf{e}_\alpha$	lattice velocity	-
E	free energy	J
$\tilde{E}$	intermediate free energy	J
$\hat{E}$	critical free energy	J
$\mathbf{E}$	electric field intensity	$\mathrm{V} \cdot \mathrm{m}^{-1}$
f	distribution function	-
f_s	area fraction	-
$\mathbf{f}$	MRT distribution function vector	-
F	phase field LBM constant	-
F'_α	forcing term in pseudopotential model	-
F_x	force in x coordinate	N
F_y	force in y coordinate	N
$\mathbf{F}$	force vector	N

$\mathbf{F_m}$	interaction force	N
$\mathbf{F_b}$	gravity force	N
g	distribution function	-
g_0	gravity acceleration constant	$\mathrm{m \cdot s^{-2}}$
$\mathbf{g}$	gravity acceleration vector	$\mathrm{m \cdot s^{-2}}$
$\mathrm{g_a}$	nondimensional gravity acceleration	-
G	SCMP LBM constant	-
h	post height	m
h'	intermediate wetting height	m
h^*	distribution function	-
H	phase field LBM constant	-
i	denoting a kind of component	-
$\bar{\imath}$	the corresponding components	-
$\mathbf{I}$	unit tenser	-
$\mathrm{k_f}$	phase field LBM constant	-
Kn	Knudsen number	-
L	lattice length	-
L_0	lattice length unit	-
m	iteration number	-
$\mathbf{m}$	MRT vector parameter	-
$\mathbf{m}^*$	MRT vector parameter	-
M	lattice mass	-
M_0	lattice mass unit	-
$\mathbf{M}$	MRT constant matrix	-
p	pressure	Pa
$\mathbf{P}$	pressure tensor	-
r	roughness area ratio	-

r_c	radius of curvature	m
r_f	wetted area ratio	-
R	gas constant	$\mathrm{J \cdot mol^{-1} \cdot K^{-1}}$
R_0	electric resistance unit	-
s	entropy	$\mathrm{J \cdot K^{-1}}$
S	solid/liquid interface area	$\mathrm{m^2}$
$\tilde{S}$	intermediate solid/liquid interface area	$\mathrm{m^2}$
S'	liquid/gas interface area	$\mathrm{m^2}$
$\widetilde{S'}$	intermediate liquid/gas interface area	$\mathrm{m^2}$
$\hat{S}$	critical solid/liquid interface area	$\mathrm{m^2}$
$\hat{S}'$	critical liquid/gas interface area	$\mathrm{m^2}$
t	time	s
T	temperature	K
T_0	lattice time unit	-
T_b	boundary temperature	K
T_c	critical temperature	K
T_s	saturation temperature	K
$\mathrm{T_t}$	lattice time	-
$\mathbf{u}$	velocity vector	$\mathrm{m \cdot s^{-1}}$
$\mathbf{u}'$	predicted velocity	$\mathrm{m \cdot s^{-1}}$
U_0	lattice electric potential unit	-
v_x	velocity in x coordinate	$\mathrm{m \cdot s^{-1}}$
v_y	velocity in y coordinate	$\mathrm{m \cdot s^{-1}}$
$\mathbf{v}$	velocity vector	$\mathrm{m \cdot s^{-1}}$
V	volume	$\mathrm{m^3}$
V_m	molar volume	$\mathrm{m^3}$
W	a temporary variable	-

$\mathbf{x}$	position	m

Greek symbols

α	sequence number	-
β	sequence number	-
β	constant parameter	-
γ	a temporary variable	-
δ_t	time interval	-
ε	a very small value	-
ε_e	permittivity	$\mathrm{F \cdot m^{-1}}$
θ	contact angle	-
λ	a temporary variable	-
λ_f	thermal conductivity	$\mathrm{W \cdot m^{-1} \cdot K^{-1}}$
$\mathbf{\Lambda}$	a diagonal matrix of relaxation times	-
μ	dynamic viscosity	$\mathrm{Pa \cdot s}$
μ_b	bulk chemical potential	Pa
μ_c	chemical potential	Pa
ν	kinematic viscosity	$\mathrm{m^2 \cdot s^{-1}}$
$\boldsymbol{\xi}$	microscopic velocity	$\mathrm{m \cdot s^{-1}}$
$\mathbf{\Pi}$	viscous stress tensor	-
ρ	density	$\mathrm{kg \cdot m^{-3}}$
ρ_0	a constant	$\mathrm{kg \cdot m^{-3}}$
σ	surface tension	$\mathrm{N \cdot m^{-1}}$
σ_0	a constant	-
σ'	equivalent free energy per unit area	$\mathrm{N \cdot m^{-1}}$
τ	relaxation time	-
τ_e	one of the MRT relaxation times	-

τ_ς	one of the MRT relaxation times	-
ϕ	order parameter	-
ϕ_s	order parameter on the wall	-
ϕ_e	electric potential	V
$\Phi(\phi_s)$	fluid/solid interaction contribution to the surface energy	-
χ	a constant	-
ψ	pseudopotential	$\mathrm{kg \cdot m^{-3}}$
Ψ	bulk free-energy density	Pa
Ψ_t	Landau free-energy	J
ω_α	weight	-
Ω	collision term	$\mathrm{kg \cdot m^{-3} \cdot s^{-1}}$
Ω_w	wetting potential	-

Subscripts/superscripts

ads	adhesion
ap	apparent
b	bulk
bar	barrier
c	critical
Cr	critical
CB	Cassie-Baxter
e	electricity
eq	equilibrium state
g	gravity acceleration
G	gas
i	denoting a kind of component
int	interaction

l	liquid
L	liquid
LG	liquid/gas
M	middle
SG	solid/gas
SL	solid/liquid
th	theoretical value
v	vapor
W	Wenzel
Y	Young

Abbreviations

APCA	apparent contact angle
BGK	Bhatnagar-Gross-Krook
CFD	computational fluid dynamics
C-S	Carnahan-Starling
DNS	direct numerical simulation
DPD	dissipative particle dynamics
DSMC	direct simulation Monte Carlo
EOS	equation of state
LB	lattice Boltzmann
LES	large eddy simulation
LGA	lattice gas automata
MCMP	multi-component multiphase
MD	molecular dynamics
MRT	multiple-relaxation-time
PDE	partial differential equation

P-R	Peng-Robinson
RANS	Reynolds-averaged Navier-Stokes equations
SCMP	single-component multiphase
SRT	single-relaxation-time
TRT	two-relaxation-time
vdW	van der Waals
VOF	volume of fluid

Chapter 1: Introduction

1.1 Background

Energy has been one of the hottest topics all around the world as it is associated to almost every aspect of our daily life and also social, scientific and technological progresses. In all the areas related to the exploration, development and application of energy, fluid flow and heat transfer have always been playing an indispensable and important role. The mass transfer and heat transfer phenomena typically involve single/multiphase flow, single/multi-component flow, phase change, and conjugate heat transfer and so forth that occur across different scales including microscale, mesoscale and macroscale. A large number of examples can be found in gas turbines, internal combustion engines, solar power plants, air-conditioning, petroleum exploitation and environment engineering, etc. [1].

Amongst all the complex flows, multiphase flow is particularly popular and has drawn lots of attention because of its broad existence in nature, extensive industrial application and complicated physics mechanism. Multiphase flow means the flow materials involve different states or phases, or the same state or phase but with different chemical properties, including single component multiphase flow, such as water and vapor system in evaporation, boiling and condensation phenomena, and multi-component multiphase flow, for example, oily water and nanofluids [2]. In fact, those natural phenomena that we are familiar with, rain, snow, debris flow, blood flow, are all multiphase flow. The most apparent feature of multiphase flow is the interface between different phases or states, which makes it more complicated than single phase flows.

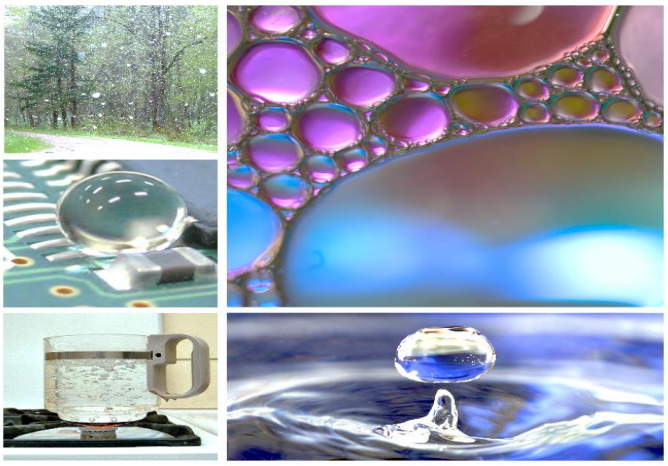

Fig. 1-1 Multiphase flow in our lives

Apart from theoretical analysis and experimental implementation, numerical investigation has also become an extraordinarily important research tool and made great contributions to a good deal of fields. Since the Reynolds-averaged Navier-Stokes equations (RANS) were solved as a basic concept for computational fluid dynamics (CFD) in 1970s by D. B. Spalding and other researchers [3], the numerical tools for computation of heat and mass transfer have been developed and made great achievements. After that, some other CFD models with much higher accuracy such as large eddy simulation (LES) [4] and direct numerical simulation (DNS) [5] have got considerable success with the increasing development of super computers. Those methods are based on continuum assumption and can be applied in macroscopic simulation. For simulation of the micro world and to understand the more fundamental mass transfer mechanism, some particle-based numerical methods have also been proposed and got huge success, for example, the direct simulation Monte Carlo (DSMC) method [6], the dissipative particle dynamics (DPD) method [7] and the most popular molecular dynamics (MD) method [8]. The dimensionless number Knudsen number *Kn*, which is defined by the ratio of the molecular mean free path length to the characteristic length, is usually used to decide whether continuum-based method or

particle dynamics-based method should be used for numerical simulation [9]. The shortcoming for conventional Navier-Stokes equations based CFD approaches is the limitation for its application in flow fields not applicable to the assumption of continuum, usually when Knudsen number *Kn* is greater than 0.1 [10]. While the particle-based methods are quite computationally consuming due to their essential nature of algorithm, to mimic the particles motion in microscope. The method sitting between the macroscopic and microscopic simulation is lattice Boltzmann (LB) method, shown in Fig. 1-2 [11]. On one hand, the LB equation can be regarded as a specific solver of the Boltzmann equation, and on the other hand, it can be seen as a minimal form of Boltzmann equation where the microscopic kinetic nature is preserved for revealing the macroscopic hydrodynamic behaviours [12]. LB method is a bridge connecting the fundamental microscopic physical principles and the macroscopic physical features. Therefore, it has been more and more popular in recent years for mesoscale simulation. Besides, LB method is also one of the most popular numerical approaches so far for multiphase flow simulation because of its unique advantages.

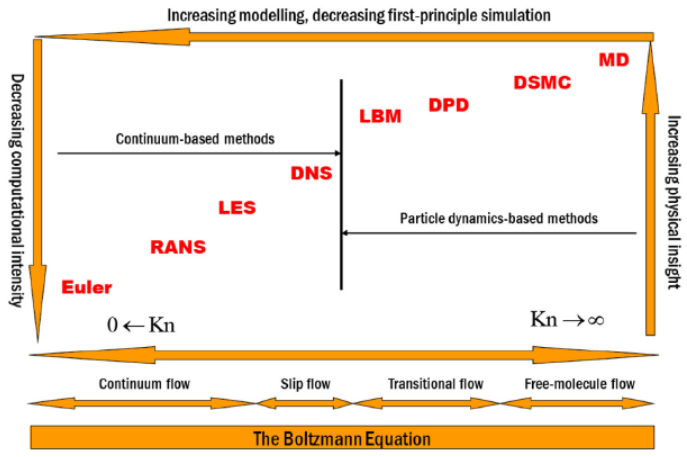

Fig. 1-2 A hierarchy of CFD simulation approaches ([11] copy right permitted)

1.2 Lattice Boltzmann method

1.2.1 Introduction of lattice Boltzmann method

LB method is originated from lattice gas cellular automaton models (LGA), which is an algorithm mimicking the entities' interactions with their neighbour entities and changing their states under specific rules [13]. LB models continued such conception by greatly simplifying Boltzmann kinetic theory of gases. As shown In Fig. 1-3, the particles or clusters of the working fluid in mesoscale point of view are simulated in the form of mass density (or other forms such as number density of molecules) distribution function, which is obtained by Taylor expansion of Maxwell equilibrium distribution function [14, 15]. Similar to LGA, the evolution of particles in LB method can also be separated into two main procedures: collision (see Fig. 1-3 (a)) and streaming (see Fig. 1-3 (b)). The collision and streaming proceed step by step alternatively, causing the flow field's moving. During the evolution, all the macroscopic parameters can be calculated via the distribution function and lattice speed.

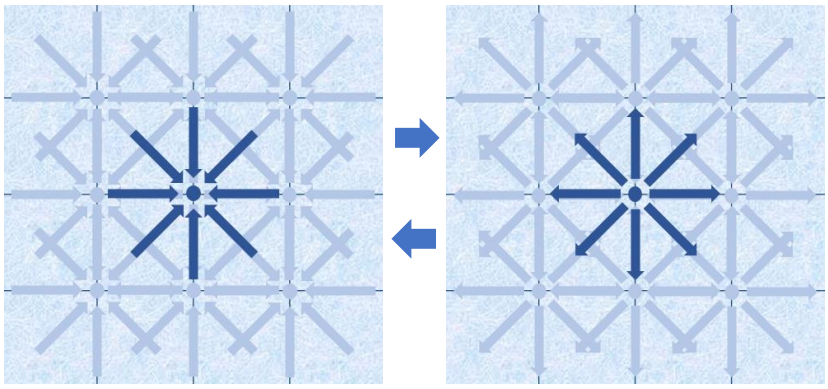

(a) (b)

Fig. 1-3 Schematic diagram of particles evolution in LB method scheme (a) collision process (b) streaming process

Compared with traditional CFD approaches, the distinctive advantages of LB method are mainly as follows [16, 17]. First of all, the convection term in LB is totally linear

whilst that in macroscopic Navier-Stokes equations is nonlinear, which leads to a simpler solver when programming the code to simulate a flow field. The second advantage is in the calculation of pressure field, which in conventional CFD approaches is usually obtained by solving a Poisson equation. However, for LB method the pressure can be calculated via an equation of state, which is explicit, simple and not costly. In addition, the bounce-back boundary conditions or the similar methods (the boundary conditions for LE method will be introduced in Section 1.2.3) in LB method is based on the fundamental mechanical rules of the interactions of particles and the boundaries, and can be easily treated and understood, thus it has a great advantage in dealing with complex boundary conditions, such as curved surfaces or boundaries in porous media. Moreover, from the basic evolution conception of the flow field in Fig. 1-3, we can see that the collision processes are absolutely local, and they occur at the same time for each evolution repetition. Even the streaming processes are also simultaneous. Therefore, parallel computing is perfectly applicable in LB method.

Due to the above-mentioned advantages of LB method, it has been dramatically developed in the recent decades, and a large number of new models were proposed. Amongst all the new proposed models in the LB community, some are presented to improve the original model by improving the collision operator from single relaxation time (SRT) to multiple-relaxation-time (MRT), two-relaxation-time (TRT), entropic LB method and cascaded LB method [18-32], or modifying the forcing scheme [33-38], or coupling with other numerical schemes [39-42], for example. Apart from this, some other models are proposed to use for specific application areas, such as multiphase flow [43-49], thermal flow [50-65], turbulent flow [66-73], as well as electromagnetic hydrodynamics [74, 75]. There are also limitations of LB models,

such as spurious currents, restricted density ratio, limited surface tension range and viscosity ratio restrictions [76]. The details of the LB models development in recent years can be found in some excellent review papers or books [76-78]. Furthermore, as a useful tool [79], the LB method has been applied in a wide range of engineering fields, which involve wettability [80, 81], phase change [82-84], porous media [85-87], conjugate heat transfer [88, 89], batteries [90-92], electroosmosis flow [93-95], viscous fingering phenomenon [96, 97], microchannel flow [98-100], nanofluids [101-105] and so forth. Besides, it has also been used as a numerical tool for solving nonlinear partial differential equations (PDE) [106-108].

1.2.2 Lattice Boltzmann equation

In this section the basic LB equation in Bhatnagar-Gross-Krook (BGK) [109-111] scheme is introduced, which is meanwhile the most popularly used LB model so far. The Boltzmann equation [13] can be simplified as

$$\frac{\partial f}{\partial t} + \boldsymbol{\xi} \cdot \frac{\partial f}{\partial \mathbf{x}} + \boldsymbol{a}_c \cdot \frac{\partial f}{\partial \xi} = \Omega_f, \tag{1-1}$$

where $f = f(\mathbf{x}, \boldsymbol{\xi}, t)$ is the distribution function, t is time, $\boldsymbol{\xi}$ is microscopic velocity, $\mathbf{x}$ is spatial position, $\boldsymbol{a}_c$ is acceleration, and Ω_f is the collision term. In BGK scheme, the collision term can be written as

$$\Omega_f = -\frac{f - f^{eq}}{\tau_f}, \tag{1-2}$$

where τ_f is the relaxation time, while f^{eq} is the equilibrium distribution function

$$f^{eq} = \frac{\rho}{(2\pi RT)^{\frac{D}{2}}} e^{-\frac{(\xi-\mathbf{u})^2}{2RT}}, \tag{1-3}$$

in which R is gas constant, D is spatial dimension, ρ is density, T is temperature, and $\mathbf{u}$ is macroscopic velocity. In LB method the microscopic velocity $\boldsymbol{\xi}$ is discretized into a group of lattice velocities

$$\mathbf{e}_\alpha = \begin{cases} (0,0), \alpha = 0, \\ c\left(\cos\frac{(\alpha-1)\pi}{2}, \sin\frac{(\alpha-1)\pi}{2}\right), \alpha = 1,2,3,4, \\ \sqrt{2}c\left(\cos\frac{(2\alpha-1)\pi}{4}, \sin\frac{(2\alpha-1)\pi}{4}\right), \alpha = 5,6,7,8, \end{cases}, \tag{1-4}$$

as shown in Fig. 1-4, where $\alpha = 0,1,2,\dots 9$ in the D2Q9 scheme, and c is a lattice constant. Via Taylor expansion at the 9 directions, the equilibrium distribution function can be approximated as

$$f_\alpha^{eq}(\mathbf{x}, t) = \omega_\alpha \rho[1 + \frac{\mathbf{e}_\alpha \cdot \mathbf{u}}{c_s^2} + \frac{(\mathbf{e}_\alpha \cdot \mathbf{u})^2}{2c_s^4} - \frac{\mathbf{u}^2}{2c_s^2}], \tag{1-5}$$

where ω_α $(\alpha = 0,1,2,\dots 9)$ are the weights and given by

$$\omega_\alpha = \begin{cases} \frac{4}{9}, \alpha = 0, \\ \frac{1}{9}, \alpha = 1,2,3,4, \\ \frac{1}{36}, \alpha = 5,6,7,8, \end{cases}, \tag{1-6}$$

and $c_s = c/\sqrt{3}$ is the lattice sound speed.

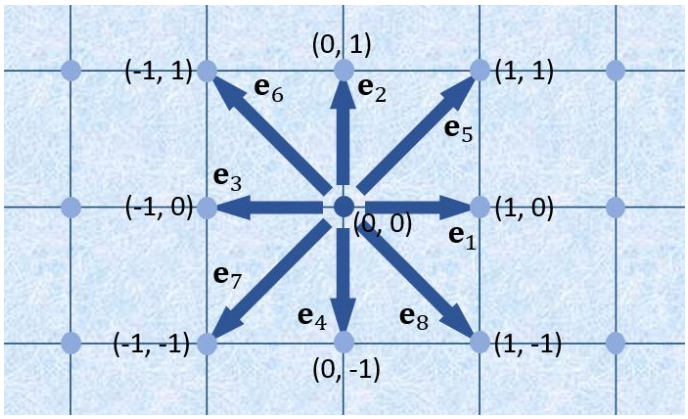

Fig. 1-4 D2Q9 lattice Boltzmann scheme

Replace the collision term in Eq. (1-1) with Eq. (1-2), and neglect external forces, the discrete Boltzmann equation in BGK scheme can be rewritten as

$$\frac{\partial f_\alpha}{\partial t} + \mathbf{e}_\alpha \cdot \nabla f_\alpha = -\frac{f_\alpha - f_\alpha^{eq}}{\tau_f}. \tag{1-7}$$

Integrating Eq. (1-7) on the time interval δ_t, the standard LB-BGK equation can be obtained [112]

$$f_\alpha(\mathbf{x} + \mathbf{e}_\alpha \delta_t, t + \delta_t) - f_\alpha(\mathbf{x}, t) = -\frac{f_\alpha - f_\alpha^{eq}}{\tau}, \tag{1-8}$$

where $\tau = \tau_f / \delta_t$ is the non-dimensional relaxation time. The LB equation contains both collision process and streaming process. The collision process can be written as [113]

$$f_\alpha'(\mathbf{x}, t) = f_\alpha(\mathbf{x}, t) - \frac{f_\alpha - f_\alpha^{eq}}{\tau}, \tag{1-9}$$

while the streaming process can be written as

$$f_\alpha(\mathbf{x} + \mathbf{e}_\alpha \delta_t, t + \delta_t) = f_\alpha'(\mathbf{x}, t). \tag{1-10}$$

The macroscopic parameters density, velocity and pressure can be calculated from the distribution functions and the microscopic lattice velocities by the following relations:

$$\rho = \sum_\alpha f_\alpha, \tag{1-11}$$

$$\rho \mathbf{u} = \sum_\alpha \mathbf{e}_\alpha f_\alpha, \tag{1-12}$$

$$p = \rho c_s^2. \tag{1-13}$$

The LB-BGK equation can be expanded via Chapman-Enskog expansion [114] to the corresponding macroscopic equations, shown as follows

$$\frac{\partial \rho}{\partial t} + \nabla \cdot (\rho \mathbf{u}) = 0, \tag{1-14}$$

$$\frac{\partial (\rho \mathbf{u})}{\partial t} + \nabla \cdot (\rho \mathbf{u}\mathbf{u}) = -\nabla p + \nabla \cdot [\rho \nu (\nabla \mathbf{u} + (\nabla \mathbf{u})^T)], \tag{1-15}$$

where the kinematic viscosity is

$$\nu = c_s^2 \left(\tau - \frac{1}{2}\right) \delta_t. \tag{1-16}$$

1.2.3 Boundary conditions

The easily treated boundary conditions for LB method is its unique feature, which can be treated following the fundamental mechanical rules of the interactions of particles and the boundaries. In this part the most basic and particularly simple boundary condition, standard bounce-back scheme [115] is introduced, as shown in Fig. 1-5 (a). After one streaming step, those particles reaching the non-slipping solid boundary do not involve in the collision step, instead, they just go back to their original positions. The beauty of such treatment lies in that we just need to designate and distinguish the solid obstacle nodes and fluid flow region nodes, and no need to treat each boundary. This is also one of the reasons that LB method is quite popular in porous media flow study, which has the most complex boundaries.

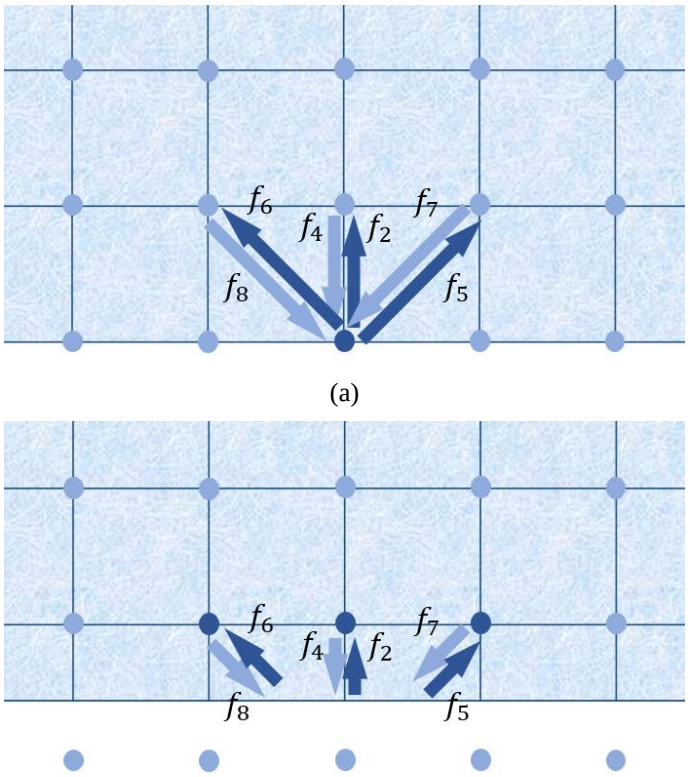

Fig. 1-5 LB basic boundary conditions (a) standard bounce-back scheme (b) half-way bounce-back scheme

The standard bounce-back scheme is particularly simple and able to strictly guarantee the mass conservation and momentum conservation, however it only gives the first order accuracy in boundaries while the LB method solved fluid flow problems with second order accuracy both in space and time [115]. To solve this problem, some more boundaries conditions with second order accuracy were proposed, such as the modified bounce-back scheme [10] and the half-way bounce-back scheme (see Fig. 1-5 (b)) [116]. In addition to these non-slipping solid boundary conditions, there are other boundary conditions based on kinetic scheme or extrapolation scheme, for dealing with both solid boundary and open boundaries such as velocity boundary or pressure boundary. Those approaches include nonequilibrium bounce-back scheme [117], counter-slip velocity scheme [118], nonequilibrium extrapolation scheme [119], etc.

The above-mentioned boundary conditions are mainly used for straight boundaries, for curved boundaries, the boundaries conditions can be found in references [120-124].

1.2.4 Multiphase and multi-component models

Amongst macroscopic numerical methods, the volume of fluid (VOF) [125] or level set [126] are both very popular multiphase flow methods for interface tracking and successfully built in commercial software such as Ansys Fluent or COMSOL. However, in these methods, the interface reconstruction step or interface reinitialization step should be conducted, which might be non-physical or very complex for programming [127]. Moreover, when dealing with surface-tension-dominated multiphase flows with complex boundaries there may be numerical instabilities [128]. Along with the rapid development of LB method, its application in multiphase flows has also drawn quite a lot attention. A large number of multiphase flow models have been proposed and most of them have been successfully applied to relevant fields. In general, the published multiphase models in literature can be classified into four main categories [113]: the colour-gradient LB model [129], the pseudopotential LB model [130, 131], the free-energy LB model [132, 133] and the phase-field LB model [134].

The first multiphase model in LB community might be the colour-gradient model which is proposed by Gunstensen et al. [129] in 1991. In this model two distribution functions are adopted for the evolution of two different fluids. Apart from the standard collision processes within the LB equations for each fluid, an additional collision operator should be implemented which is related to the surface tension between the two fluids. In addition, a recolouring step is needed in this model in order to realize the phase segregation and keep the interface [135, 136]. One advantage of the colour-

gradient model is that the surface tension and the viscosity ratio can be adjusted independently [137]. The shortcoming of this model is that the cases with large density ratio can be hardly achieved [138].

The free-energy LB multiphase model was proposed by [132, 133]. This model takes the thermodynamics into consideration by incorporating a non-ideal thermodynamic pressure tensor into the revised equilibrium distribution function. However, the original free-energy model suffers the problem of Galilean invariance because of the non-Navier-Stokes terms introduced when modifying the equilibrium distribution function. To solve the problem of Galilean invariance, some researchers modified the model by redefining the stress tensor or incorporating some correction terms and then the issue can be finally covered [133, 139].

The pseudopotential model, which was first proposed by Shan and Chen [130, 131] has shown superiority because of its simplicity, versatility and the distinctive feature of automatic phase separation without any specific techniques for interface capturing or tracking. The most important feature of this model is the pseudo- potential that applied to particles to accomplish the interaction forces. The ideal equation of state (EOS) is replaced by a non-ideal non-monotonic EOS so that there are the coexisting densities under one temperature condition for both liquid phase and vapour phase. The model for single-component multiphase (SCMP) model adopted one distribution function for both two phases of one fluid component while two or more distribution functions are used for multi-component multiphase (MCMP) model for different components.

For phase-field model, the Cahn-Hilliard equation or a Cahn-Hilliard-like equation should be considered to capture the liquid-vapor interface [140], which is based on the

phase field theory. One order parameter that obeys the phase field theory should be solved in an LB equation. And the order parameter which is integrated from the corresponding distribution function represent the different phases and the interface between them. The most significant feature of this model is that the high-density ratio can be easily achieved using the phase-field model. At the meantime it is more complex as one more interface treatment governing equation should be solved.

Amongst the above mentioned models in the field of multiphase flow, pseudopotential LB model and the phase-field model have been the most popular approaches and are becoming increasingly significant roles in multiphase flow and phase change heat transfer modelling [113].

1.3 Research objectives

The aim of this work is the development and applications of the mesoscale numerical simulation method, lattice Boltzmann method, which is used to resolve some cutting-edge problems in multiphase flow and heat transfer which are difficult to be investigated in experiment or other macroscopic or microscopic numerical methods. Three practical physical problems in regard to wetting phenomenon, oil/water separation and boiling heat transfer, and one LB model issue for multiphase flow are investigated. Although having been broadly applied in a great number of engineering or industrial applications, the mechanisms of the problems are still not completely understood by researchers, as they involve complicated physical problems such as multi-component flow, multiphase flow, phase change or electromagnetic field.

The objectives of the work are as follows:

1) Accomplishing the wetting transition processes to have a deeper understanding of the wetting transition principles between Cassie-Baxter wetting state and Wenzel state and proposing new mathematical model to describe the transitions from the free surface energy viewpoint; studying the irreversibility of wetting transitions; designing and validating new micro structures to increase the energy barrier between two wetting states to achieve a higher and more stable contact angle for superhydrophobic surfaces.
2) Proposing new multi-component multiphase mesoscale models to study the oil-in-water problems; studying the dielectrophoresis force effect on oil droplets in water and investigating the feasibility of applying electric field in down hole oil water separation technology, i.e. hydrocyclones.
3) Proposing and verifying new mesoscale models for phase change and boiling heat transfer and accomplishing three boiling stages using the proposed numerical model.
4) Studying the multi-bubble/droplet problem of single component multiphase pseudopotential lattice Boltzmann method; analysing possible reasons and finding approaches to solve this problem.

1.4 Thesis structure

Each work of the four mentioned parts are written in one chapter. Therefore, the structure of this thesis is arranged as follows:

Chapter 1 presents the introduction of lattice Boltzmann method, including the history and development of LB method in the last three decades, LB equations, boundary conditions and multiphase/multi-components models.

Chapter 2 is the whole work on studying the droplet wetting transitions on biomimetic surfaces. A literature review is given first, following by the theoretical analysis of the free surface energy between Cassie-Baxter wetting state and Wenzel wetting state. Numerical simulation is conducted using a phase field LB method to simulate the processes of the wetting transitions to verify the proposed mathematical model, i.e. the energy curves. According to the theoretical analysis, the micro structure of posts with truncated pyramid shape is studied instead of the square-post micro roughness surfaces and is verified to have a better superhydrophobicity property in the last section of this chapter.

In Chapter 3, the literature review and problems are illustrated for cutting-edge down hole oil water separation technologies. Then the proposed multi-component multiphase model coupling with the discrete electrostatic field equation is presented. The numerical simulation for validation of the model and studying the dielectrophoresis force effect on oil droplets are then given. Finally, the experiment study for electric field effect on oil-water mixture is presented and discussed.

The mesoscale of boiling heat transfer is discussed in Chapter 4. The literature review is give firstly as well, and then followed by the detailed numerical algorithm. The validation part is given in three parts: liquid-vapour coexistent densities, D^2 law for droplet evaporation and the three boiling stages.

The multi-bubble/droplet coexistence problem is studied in Chapter 5. The features of the problem which we call it “the big eat the small” is firstly stated, and then a deeply study on this feature is conducted, finally the thermal models’ effect on the problem is investigated.

In the last chapter Chapter 6 the detailed conclusions of each part of work and the corresponding outlook for future work are given.

Chapter 2: Droplet Wetting Transition Study on Patterned Roughness Surface

2.1 Introduction

Surface roughness, which can be found in the form of micro or hierarchical structures in nature, has been widely investigated for its enhancement to hydrophobicity [141-144]. Through mimicking natural superhydrophobic surfaces including plant leaves and animals such as lotus leaves, rice leaves and water strider legs, manmade superhydrophobic surfaces via various of methodologies have been presented and applied in industrial applications, for instance, coating, self-cleaning surfaces, microfluidic devices with surface-tension-induced drop motion and so forth [145, 146]. Among all the natural water-repellence examples, lotus leaves are the most impressive for their superhydrophobic characteristic which is also known as “lotus effect”. Due to the micrometre order length scales of the micro posts on the surfaces, the apparent contact angle (APCA) of lotus leaves is approximately 160° while the hysteresis angle is just about 4° [147].

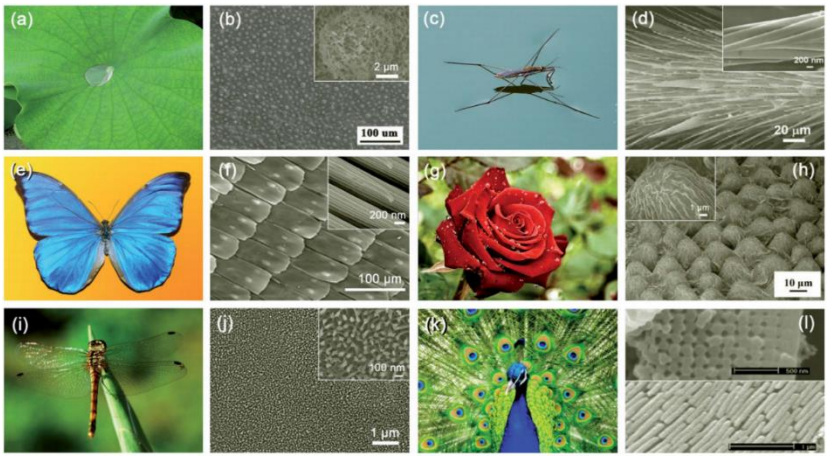

Fig. 2-1 Superhydrophobic surface in nature and micro roughness structures ([148] copy right permitted)

As the wetting phenomena have been investigated over the past decades, significant progress on theoretical models has also been achieved with considerable attention. The starting point of wetting on an ideal rigid, flat and homogeneous surface is characterized by the well-known Young's Equation [149]:

$$\cos\theta_Y = \frac{\sigma_{SG}-\sigma_{SL}}{\sigma_{LG}} \tag{2-1}$$

where σ is the surface tension which represents the energy per unit area of the interface between solid/gas, solid/liquid or liquid/gas, and θ_Y is the Young's contact angle. Young's Equation reveals the relationship between surface tensions and contact angle in the ideal situation, however, it cannot be applied to most real surface conditions due to the existence of surface roughness. For the surface roughness, a new correlation where the apparent contact angle is related to surface roughness was presented by Wenzel [150]:

$$\cos\theta_w = r\frac{\sigma_{SG}-\sigma_{SL}}{\sigma_{LG}} \tag{2-2}$$

which is also normally written as the following reformed equation:

$$\cos\theta_w = r\cos\theta_Y \tag{2-3}$$

where r, the roughness parameter corresponding to the "roughness factor", which is also referred to as roughness area ratio, denotes as the ratio of the actual surface area with respect to the projected structure surface, and θ_w is the Wenzel's angle. The Wenzel equation is associated with the homogeneous wetting states, where the grooves caused by the surface roughness are penetrated with water. Apart from the homogeneous wetting state, there is another stable state, the heterogeneous wetting

state, and the corresponding equation to the heterogeneous wetting regime was proposed by Cassie and Baxter [151]:

$$cos\theta_{CB} = f_s cos\theta_Y + f_s - 1 \tag{2-4}$$

If the roughness ratio, r_f, the ratio of the actual wetted area over the projected area is considered, Eq. (2-4) can be modified to the following form [152]:

$$cos\theta_{CB} = r_f f_s cos\theta_Y + f_s - 1 \tag{2-5}$$

where f_s is the area fraction on the horizontal projected plane of the liquid-solid contact area over the total area of solid-liquid and liquid-gas contact. Eq. (2-5) would become the same form with Wenzel's equation when $f_s = 1$ and $r_f = r$. By equating Eq. (2-3) and Eq. (2-5), the critical contact angle theoretically used to separate the two wetting states can be calculated as [153]:

$$cos\theta_C = \frac{1-f_s}{r_f f_s - r} \tag{2-6}$$

It should be noted that when $\theta_C > 90°$, both two wetting states exist. Then the homogeneous wetting state is preferable only if $\theta_Y < \theta_C$, otherwise the droplet stays at a heterogeneous wetting state, theoretically [154]. However, it has been observed that, even the Young's angle is smaller than the critical angle, the Cassie-Baxter wetting state can exist, which means that Wenzel and Cassie Baxter states may stay on the same specific surface at the same time [155-158].

Bormashenko reviewed the main experimental and theoretical approaches to wetting transitions in 2010 and 2015 respectively [159, 160]. Experiments to study the wetting transitions were implemented by giving external factors such as pressure [161], initial velocity [162], evaporation of droplets [163], vibration [164], and electric field [165,

166]. And the role of gravity in wetting transitions was also discussed [152]. Neelesh A. Patankar [152] and Zu et al [167] theoretically analysed the wetting transition from Cassie-Baxter state to Wenzel state from the free energy point of view, and the energy barrier was discussed both in their work. Whyman et al. [168] theoretically investigated the interfacial free energy and discussed the irreversibility of Cassie-to-Wenzel transition. Ren [169] computed the transition states, the energy barriers and the minimum energy paths for Cassie-to-Wenzel transition using the string method. Pashos et al. [170, 171] developed a numerical method to investigate the minimum energy paths and the free energy changes were presented in their works. S. Prakash et al. [172] studied the spontaneous recovery of superhydrophobicity on nanotextured surfaces using molecular simulations. Bico et al. [173] and Bormashenko et al. [174] studied the Cassie impregnating state apart from the Cassie-Baxter state and Wenzel state, and Gibbs free energy curves of the three wetting states were presented. In their work the impregnating state was observed via vibration so that the liquid can impregnate the grooves outside of the droplet/solid interface. In this work, the transition between the more regular Cassie-Baxter and Wenzel wetting states is focused on.

Wenzel's equation and Cassie and Baxter's equation can describe the stable wetting states on real rough surfaces to a great extent when the droplet size is much larger than the typical roughness scale. Nevertheless, there are still points of the theory of wetting states which are not fully understood. For instance, when a droplet stays in a stable wetting state, and how the transition between the two wetting states occurs [154]. It is crucial to understand the mechanism of wetting transition process for the design and manufacturing of devices with highly stable superhydrophobic surfaces. This work

focuses on the wetting transition process as well as the different wetting states on the simplest model, the square-post patterned surface from the free energy point of view.

Study of wetting phenomena using LB method is also a popular topic. Dupuis and Yeomans [175] firstly used the lattice Boltzmann method to study the droplet motions on superhydrophobic surfaces, and then followed by other researchers who studied the Cassie-to-Wenzel transition [176], contact angle hysteresis [177], droplet morphology [178], droplet influence [179] and droplet motion on hydrophobic surfaces [180, 181]. A significant issue in most of their models is that the unwanted spurious currents cannot be eliminated and a large density ratio for liquid/gas system cannot be achieved. Swift et al. [132] proposed a new implementation of boundary conditions for the complex geometry in simulations of droplets on superhydrophobic surfaces, which can eliminate spurious currents, however, they did not accurately capture the transition between wetting states. Among all the lattice Boltzmann models, the phase field lattice Boltzmann model has been successfully applied in two phase flow simulation with large density ratio [182]. Yan et al. [134] presented a phase field lattice Boltzmann scheme for two-phase flows involving partial wetting surfaces and large density ratio up to 1000 which combines the advantages of the two models presented by Briant [183, 184] and Inamuro [185]. This model has been successfully used in simulation of the droplet motion on micro-structured rough surfaces [186, 187]. Tanaka et al. [188] used this phase field model to conduct a 2-D simulation of dynamic behaviour of droplet on flat solid surfaces.

The aim of this work is theoretical analysis of the surface free energy change during wetting transitions and using the phase field lattice Boltzmann method for large density ratio to study the wetting transitions between Wenzel state and Cassie-Baxter state on

a square-post textured surface in mesoscale and to help understand the mechanism of wetting transitions. Besides, the gravity effect and irreversibility of wetting transitions, as well as the shape of micro posts effect are also discussed in this work.

2.2 Theoretical analysis

In the present study, the substrate patterned by square posts as the roughness surface is considered as shown in Fig. 2-2, where a, d and h are the post width, post spacing, and post height respectively. It should be pointed out that the droplet size scale is much larger than the size scale of micro posts in the theoretical analysis. Under this assumption, the theoretical analysis can be conducted based on a single unit of patterned substrate with periodical pattern and the Wenzel and Cassie-Baxter equations can be used for the calculation of the apparent contact angles. In the presented pattern, r_f equals to 1.

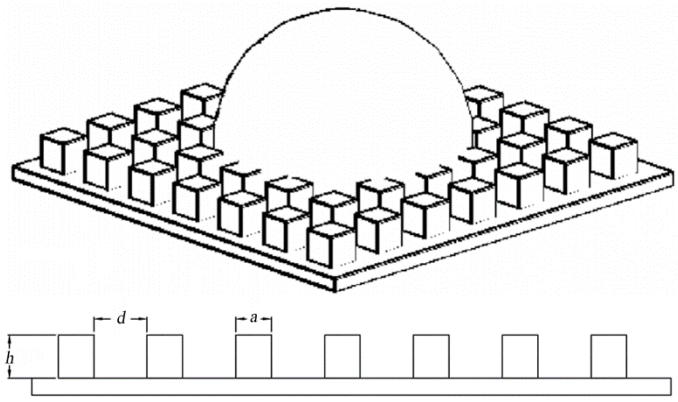

Fig. 2-2 Structure of the micro roughness surface

2.2.1 The model of net free energy

All the parameters needed for the following theoretical analysis are presented in Fig. 2-3 in three typical wetting state cases. Firstly, considering a droplet staying steady on

a flat ideal surface as shown in Fig. 2-3 (a), the equilibrium free energy can be calculated as [154]:

$$E_Y = S(\sigma_{SL} - \sigma_{SG}) + S'\sigma_{LG} \tag{2-7}$$

where S and S' represent the solid/liquid interface area and the liquid/gas interface area respectively. Similarly, the equilibrium free energy equations for Cassie-Baxter and Wenzel states are:

$$E_{CB} = S_{CB}(\sigma'_{SL} - \sigma_{SG}) + S'_{CB}\sigma_{LG} \tag{2-8}$$

$$E_W = S_W(\sigma'_{SL} - \sigma_{SG}) + S'_W\sigma_{LG} \tag{2-9}$$

where σ'_{SL} is the equivalent free energy per unit area of the solid/liquid interfaces for both of the two states, while S_{CB} and S_W both represent the projected horizontal areas. Considering the equivalent surface tension, Young's equation can be applied into the heterogeneous and homogeneous wetting states:

$$\cos\theta_{CB} = \frac{\sigma_{SG} - \sigma'_{SL}}{\sigma_{LG}} \tag{2-10}$$

$$\cos\theta_W = \frac{\sigma_{SG} - \sigma'_{SL}}{\sigma_{LG}} \tag{2-11}$$

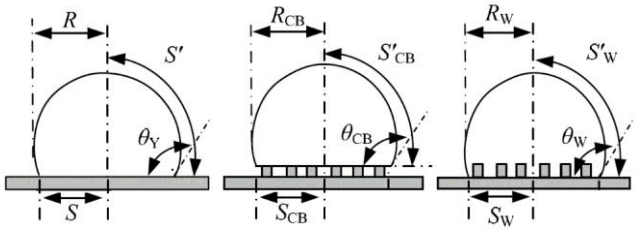

(a) (b) (c)

Fig. 2-3 Parameters of the droplet in (a) flat surface (b) Cassie-Baxter state and (c) Wenzel state

By combining the above equations, the free energy equations for Cassie-Baxter and Wenzel states can be expressed as:

$$E_{CB} = S_{CB}[f(\sigma_{SL} - \sigma_{SG}) + (1-f)\sigma_{LG}] + S'_{CB}\sigma_{LG} \tag{2-12}$$

$$E_W = S_W r(\sigma_{SL} - \sigma_{SG}) + S'_W \sigma_{LG} \tag{2-13}$$

2.2.2 Cassie-to-Wenzel wetting transition

Usually, the transition process from Cassie-Baxter state to Wenzel state can be easily observed, however, the reverse process is hard to be achieved. Thus it is generally agreed that the wetting transition from Cassie-Baxter state to Wenzel state is irreversible [160]. Fig. 2-4 shows the two main processes of wetting transitions: (a) water starting to penetrate the posts intervals without touching the bottom surface; (b) water immersing the bottom surface. The position of the air pocket in Fig. 2-4 (b) can be neglected because the immersing-bottom process just lowers the free energy and does not hinder the transition regarding the following analysis. $\tilde{E}_{CB}$ and $\tilde{E}_W$ are used to represent the intermediate free energy of the droplet. According to Eq. (2-7), there are:

$$\tilde{E}_{CB} = \tilde{S}_{CB}\left\{\left[f + (r-1)\frac{h'}{h}\right](\sigma_{SL} - \sigma_{SG}) + (1-f)\sigma_{LG}\right\} + \tilde{S}'_{CB}\sigma_{LG} \tag{2-14}$$

$$\tilde{E}_W = \tilde{S}_W\left[r - (1-f)\frac{d'}{d}\right](\sigma_{SL} - \sigma_{SG}) + \left[\tilde{S}'_W + \tilde{S}_W(1-f)\frac{d'}{d}\right]\sigma_{LG} \tag{2-15}$$

When h' and d' are on their extreme values h and d, the critical free energy states can be achieved:

$$\hat{E}_{CB} = \hat{S}_{CB}\{[f + (r-1)](\sigma_{SL} - \sigma_{SG}) + (1-f)\sigma_{LG}\} + \hat{S}'_{CB}\sigma_{LG} \quad (2\text{-}16)$$

$$\hat{E}_W = \hat{S}_W[r - (1-f)](\sigma_{SL} - \sigma_{SG}) + \left[\hat{S}'_W + \hat{S}_W(1-f)\right]\sigma_{LG} \quad (2\text{-}17)$$

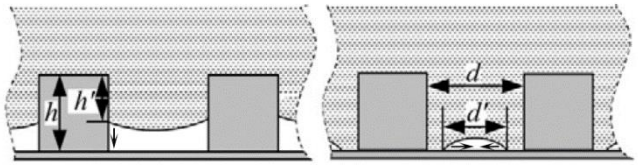

(a) (b)

Fig. 2-4 Intermediate states for transition (a) water starting to penetrate the posts intervals without touching the bottom surface (b) water immersing the bottom surface

It has been proved that the differences of the liquid/gas area and the droplet bottom projected area when transition happens are negligible owing to the much larger size scale compared to that of the surface roughness, which means $\hat{S}_{CB} \approx S_{CB}$, $\hat{S}_W \approx S_W$, $\hat{S}'_{CB} \approx S'_{CB}$ and $\hat{S}'_W \approx S'_W$ [152, 189]. Hence there is $\hat{E}_{CB} = \hat{E}_W = E_{Cr}$ for the same droplet in different states. And the energy barriers for the two transitions process can be calculated as:

$$E_{bar}^{CB-Cr} = \hat{E}_{CB} - E_{CB} = S_{CB}(r-1)(\sigma_{SL} - \sigma_{SG}) \quad (2\text{-}18)$$

$$E_{bar}^{\mathrm{Cr}-W} = E_W - \hat{E}_W = S_W(f-1)(\sigma_{LG} - \sigma_{SL} + \sigma_{SG}) \quad (2\text{-}19)$$

For hydrophobic surfaces, i.e. $\theta_Y > 90°$, according to the Young's equilibrium equation, there are $\sigma_{SL} - \sigma_{SG} > 0$ and $\sigma_{LG} - \sigma_{SL} + \sigma_{SG} > 0$, therefore

$$E_{bar}^{CB-Cr} > 0 \tag{2-20}$$

$$E_{bar}^{\mathrm{Cr}-W} < 0 \tag{2-21}$$

Correspondingly, for hydrophilic water, i.e. $\theta_Y < 90°$, there are $\sigma_{SL} - \sigma_{SG} < 0$and $\sigma_{LG} - \sigma_{SL} + \sigma_{SG} > 0$, therefore

$$E_{bar}^{CB-Cr} < 0 \tag{2-22}$$

$$E_{bar}^{\mathrm{Cr}-W} < 0 \tag{2-23}$$

Whether the transition can occur depends on the sign of the differential of free energy at the beginning of the process. For transitions from Cassie-Baxter state to Wenzel state and the reverse, the free energy differentials can be given as:

$$\frac{\delta E^{CB-Cr}}{\delta h'}\Big|_{h'=0} = \frac{S_{CB}(r-1)(\sigma_{SL}-\sigma_{SG})}{h} \tag{2-24}$$

Consequently, without considering the gravity effect or other external forces, the free energy curves can be drawn in Fig. 2-5. Fig. 2-5 (a) and Fig. 2-5 (b) show the case of $\theta_Y > 90°$, when two main roughness surface features exist: (a) $90° < \theta_Y < \theta_C$, $E_{CB} > E_W$, according to the assumption that the equilibrium state occurs when the free energy is minimized [152], both of the two states exist, however, the Wenzel state is stable while Cassie-Baxter state is not; (b) $\theta_Y > \theta_C, E_W > E_{CB}$, the droplet would stay in the Cassie-Baxter state, but may not in the Wenzel state and the analysis relating to this is in the next section. This means the energy barrier always exists for the Cassie-to Wenzel transition for $\theta_Y > 90°$. In addition, $\frac{\delta E^{CB-W}}{\delta h'}\Big|_{h'=0} > 0$ denotes that the transition processes cannot happen spontaneously without any external stimuli

triggering event. Fig. 2-5 (c) indicates that Cassie-Baxter state cannot be achieved if $\theta_Y < 90°$, when $E_{CB} > E_W$ and $\frac{\delta E^{CB-W}}{\delta h'}\Big|_{h'=0} < 0$ thus the droplet can only stays at the Wenzel state. It should be noted that all the free energy curves presented in this work are qualitatively constructed because there exist uncertainties for the wetting transitions, for example, the bottom droplet surface moving down along the posts is not definitely horizontal and when and which part of the droplet touches the bottom solid surface first is indeterminate.

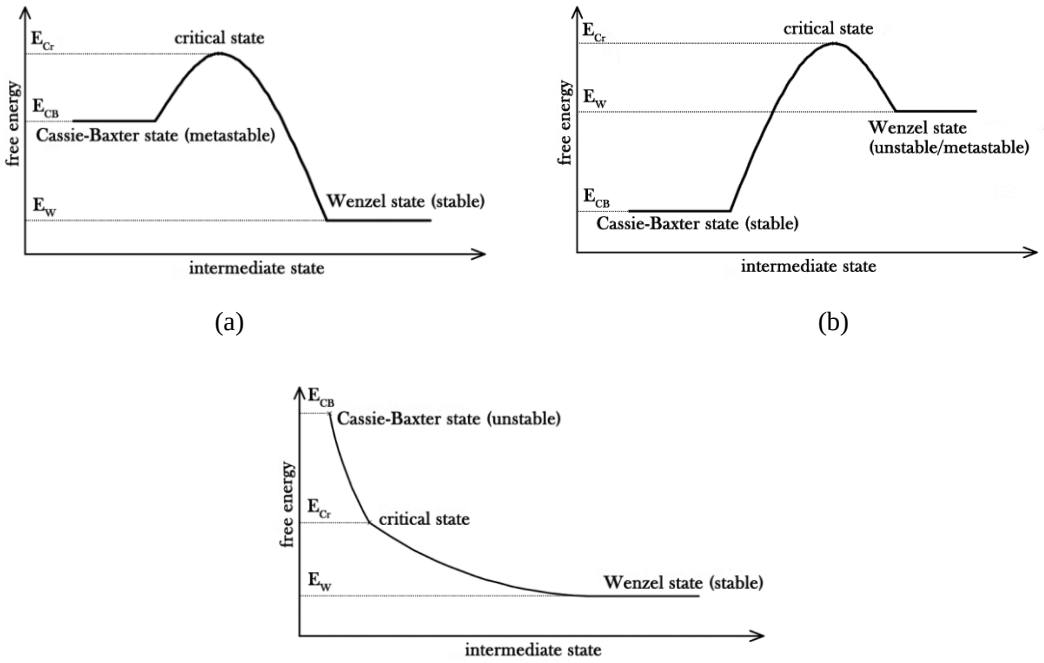

Fig. 2-5 Free energy curves without gravity effect for (a) $90° < \theta_Y < \theta_C$ (b) $\theta_Y > \theta_C$ and (c) $\theta_Y < 90°$

The gravity does not affect the shape and the wetting state of a droplet significantly when the drop radius is much smaller than $(\sigma_{LA}/\rho g)^{1/2}$. However, its influence on transition may be nonnegligible [152]. When a droplet transits from the Cassie-Baxter state to the Wenzel state, the potential energy of gravity E_G declines as well. Since the potential energy change occurs along with the transition process between Cassie-

Baxter state and the critical state when the droplet is about to immerse the air pockets completely but have not yet reached the bottom surface, the energy curves can be modified by adding the potential energy change of which the sign is negative. When $\theta_Y < 90°$, the energy curve is similar to Fig. 2-5 (c), where the energy change is monotonous. However, for $\theta_Y > 90°$, one more case appears as shown in Fig. 2-6:

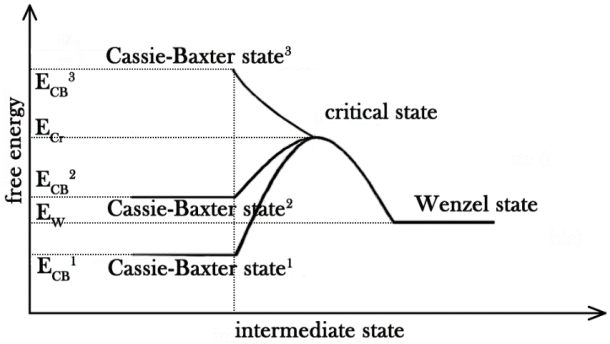

Fig. 2-6 Energy curves with gravity effect for $\theta_Y > 90°$

Fig. 2-6 shows the extra curve of case 3 when considering the gravity effect with a monotonous energy change, which denotes that the transition can occur spontaneously. In this case, the source of potential energy change ΔE_G can overcome the energy barrier E_{bar}^{CB-Cr}, and the conclusion is the same with that from Patankar [152] which is achieved via comparing the theoretical analysis with experimental data from Yoshimitsu et al [190]. To avoid the spontaneous wetting transition triggered by gravity, the surface intrinsic Young's angle θ_Y and the surface pattern (r_f and f_s) should be modified to increase the energy barrier.

2.2.3 Discussion about the irreversibility of wetting transition

As mentioned above, it is generally thought that the transition from Cassie-Baxter state to Wenzel state is irreversible. From Fig. 2-6 it can be seen that the gravity potential energy can decrease the energy barrier E_{bar}^{CB-W} or even overcome it. Besides, other

external stimuli such as initial velocity, pressure and vibration can also be also used to overcome the energy barrier. Therefore, in most cases the Cassie-to-Wenzel transition is easier to be achieved, and more attention is paid on this transition due to its importance to superhydrophobic surfaces development.

Without considering the gravity effect, the reverse Wenzel-to-Cassie transition would take a different route. It is reasonable to assume the transition happens on the bottom from the vicinity of the gas-liquid-solid triple line, since air cannot be generated from the void, as shown in Fig. 2-7. Therefore, the triple lines may move simultaneously in the horizontal and vertical directions. The energy decreased as solid-liquid contact area decreases may overcome the energy increased as liquid-gas contact area and solid-gas contact area increase, and if not, the reversible transition cannot occur spontaneously. Fig. 2-8 presents the different routes of wetting transitions. It should be noticed that the reverse energy change may not be monotonous in Fig. 2-8 (a) in the case that the droplet is separated from the bottom but the vertical process has not finished yet, and in Fig. 2-8 (b) the critical Young's angle for the Wenzel-to-Cassie transition may not be the same with the critical angle in Eq. (2-6).

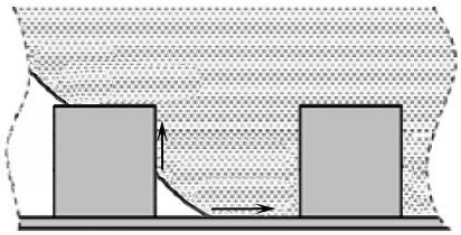

Fig. 2-7 Intermediate states for Wenzel-to-Cassie transition

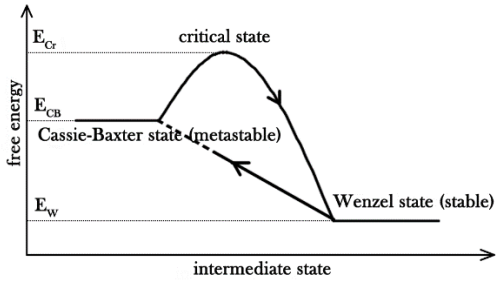

(a)

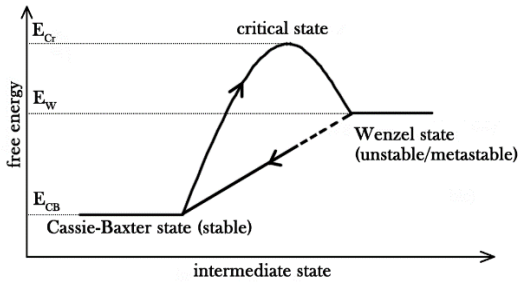

(b)

Fig. 2-8 Free energy curves without gravity effect for (a) $90° < \theta_Y < \theta_C$ (b) $\theta_Y > \theta_C$

Gravity potential can be considered as a part of the energy barrier needed to overcome. It is much more difficult to trigger the reverse transition than the Cassie-to-Wenzel transition due to the different transition routes, which can explain the irreversibility of wetting transition. Experiments to achieve the reverse transition were carried out by heating the substrate [191] or transmitting a short pulse of electrical current [166], and both of the two experiments appeared to be conducted by the evaporation of the droplet in the vicinity of their gas-liquid-solid triple line, changing liquid phase to vapor phase to break the reverse energy barrier and complete the reverse transition. Thus, a metastable Cassie-Baxter wetting state can be achieved as shown in Fig. 2-8 (a).

The energy curves shown in Fig. 2-8 can be very helpful to understand the wetting transition mechanism and develop superhydrophobic surfaces. Some surfaces with topographic features involving specialized geometries such as inverse trapezoidal [192], T-shape [193] and serif-T [194] are the typical examples to impede Cassie-to-

Wenzel wetting transition by increasing the energy barrier during Cassie-to-critical process, namely raising the critical state energy in Fig. 2-8. However, few papers were found to focus on the critical-to-Wenzel process, which could also be a crucial factor to affect wetting transition because no matter how high the critical state energy is the Cassie-to-Wenzel transition can be finished when the energy barrier is overcame by external forces. Such work relating to the bottom surface as well as the critical-to-Wenzel process will be investigated in the future.

2.3 Methodology

In this work, the simulation is based on the phase field lattice Boltzmann approach for incompressible two-phase flows with large density ratio involving partial wetting surface [186]. As shown in Fig. 2-9, the model is in three dimension and based on D3Q15 scheme, in which 15 directions are adopted for streaming. The velocity vectors are:

$$[\mathbf{c}_0, \mathbf{c}_1, \mathbf{c}_2, \mathbf{c}_3, \mathbf{c}_4, \mathbf{c}_5, \mathbf{c}_6, \mathbf{c}_7, \mathbf{c}_8, \mathbf{c}_9, \mathbf{c}_{10}, \mathbf{c}_{11}, \mathbf{c}_{12}, \mathbf{c}_{13}, \mathbf{c}_{14}] = \begin{bmatrix} 0 & 1 & 0 & 0 & -1 & 0 & 0 & 1 & -1 & 1 & 1 & -1 & 1 & -1 & -1 \\ 0 & 0 & 1 & 0 & 0 & -1 & 0 & 1 & 1 & -1 & 1 & -1 & -1 & 1 & -1 \\ 0 & 0 & 0 & 1 & 0 & 0 & -1 & 1 & 1 & 1 & -1 & -1 & -1 & -1 & 1 \end{bmatrix} \tag{2-25}$$

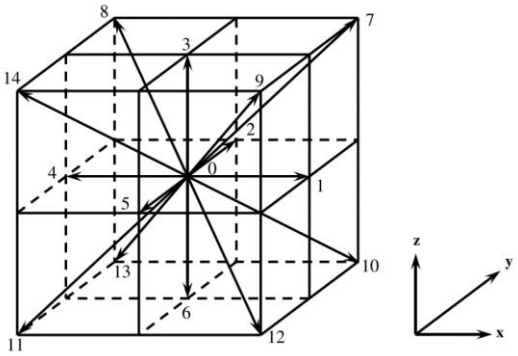

Fig. 2-9 D3Q15 scheme

Two velocity distribution functions, f_α and g_α, are applied in this phase field model. The distribution function f_α is applied for the calculation of the order parameter ϕ which is used to distinguish the gas/liquid two phases. While distribution function g_α is employed as the distribution function of the predicted velocity $\mathbf{u}'$, which needs to be corrected by pressure gradient of the two-phase system. The lattice Boltzmann equations including streaming and collision steps of particles can be written as:

$$f_\alpha(\mathbf{x}+\mathbf{c}_{\boldsymbol{\alpha}}\delta_t, t+\delta_t) = f_\alpha(\mathbf{x},t) - \frac{1}{\tau_f}\left(f_\alpha(\mathbf{x},t) - f_\alpha^{eq}(\mathbf{x},t)\right) \tag{2-26}$$

$$g_\alpha(\mathbf{x}+\mathbf{c}_{\boldsymbol{\alpha}}\delta_t, t+\delta_t)$$

$$= g_\alpha(\mathbf{x},t) - \frac{1}{\tau_g}\left(g_\alpha(\mathbf{x},t) - g_\alpha^{eq}(\mathbf{x},t)\right) + 3\omega_\alpha\frac{1}{\rho}\nabla\cdot[\mu(\nabla\mathbf{u}+\mathbf{u}\nabla)]\cdot\mathbf{c}_{\boldsymbol{\alpha}} \tag{2-27}$$

Where $\mathbf{x}$ and t are space position and time; $\mathbf{u}$, μ, and ρ are the macroscopic parameters, representing velocity, dynamic viscosity and density; τ_f and τ_g are dimensionless single relaxation times; $\delta_t = 1$ is the time step; f_α^{eq} and g_α^{eq} are the equilibrium distribution functions for equilibrium states and defined as:

$$f_\alpha^{eq}(\mathbf{x},t)$$

$$= \mathrm{H}_\alpha\phi + \mathrm{F}_\alpha\left[p_0 - \mathrm{k_f}\phi\nabla^2\phi - \frac{\mathrm{k_f}}{6}|\nabla\phi|^2\right] + 3\omega_\alpha\phi(\mathbf{c}'_\alpha\cdot\mathbf{u}) + \omega_\alpha\mathrm{k_f}\mathbf{c}'_\alpha\cdot\boldsymbol{G}(\phi)\cdot\mathbf{c}_{\boldsymbol{\alpha}} \tag{2-28}$$

$$g_\alpha^{eq}(\mathbf{x},t)$$

$$= \omega_\alpha\left[1 + 3(\mathbf{c}'_\alpha\cdot\mathbf{u}) + \frac{9}{2}(\mathbf{c}'_\alpha\cdot\mathbf{u})^2 - \frac{3}{2}\mathbf{u}^2 + \frac{3}{2}\left(\tau_g - \frac{1}{2}\right)\mathbf{c}'_\alpha\cdot(\nabla\mathbf{u} + \mathbf{u}\nabla)\cdot\mathbf{c}_{\boldsymbol{\alpha}}\right] +$$

$$\omega_\alpha\frac{k_f}{\rho}\mathbf{c}'_\alpha\cdot\boldsymbol{G}(\phi)\cdot\mathbf{c}_{\boldsymbol{\alpha}} - \frac{2}{3}\mathrm{F}_\alpha\frac{\mathrm{k_f}}{\rho}|\nabla\phi|^2 \tag{2-29}$$

where

$$\omega_\alpha = \begin{cases} \frac{2}{9} & \alpha = 0 \\ \frac{1}{9} & \alpha = 1,\dots 6 \\ \frac{1}{72} & \alpha = 7,\dots,14 \end{cases} \tag{2-30}$$

$$\mathrm{F}_\alpha = \begin{cases} -\frac{7}{3} & \alpha = 0 \\ \frac{1}{3} & \alpha = 1,\dots 6 \\ \frac{1}{24} & \alpha = 7,\dots,14 \end{cases} \tag{2-31}$$

$$\mathrm{H}_\alpha = \begin{cases} 1, & \alpha = 0 \\ 0, & \alpha = 1,\dots,14 \end{cases} \tag{2-32}$$

and

$$\boldsymbol{G}(\phi) = \frac{9}{2}(\nabla\phi)(\phi\nabla) - \frac{3}{2}|\nabla\phi|^2\mathbf{I} \tag{2-33}$$

and as a constant, $\mathrm{k_f}$ is related to the strength of surface tension as well as the width of interface.

With $\Psi(\phi)$ as the bulk free-energy density, the equation of state of the fluid is:

$$p_0 = \phi \frac{\partial \Psi}{\partial \phi} - \Psi \tag{2-34}$$

The macroscopic variables ϕ, $\mathbf{u}'$, ρ and μ can be computed from the distribution functions by:

$$\phi = \sum_\alpha f_\alpha \tag{2-35}$$

$$\mathbf{u}' = \sum_\alpha \mathbf{c}_{\boldsymbol{\alpha}} g_\alpha \tag{2-36}$$

$$\rho = \begin{cases} \rho_G, & \phi < \phi_G \\ \frac{\phi - \phi_G}{\phi_L - \phi_G}(\rho_L - \rho_G) + \rho_G, & \phi_G \le \phi \le \phi_L \\ \rho_L, & \phi > \phi_L \end{cases} \tag{2-37}$$

$$\mu = \frac{\rho - \rho_G}{\rho_L - \rho_G}(\mu_L - \mu_G) + \mu_G \tag{2-38}$$

where the subscript L means liquid and G represents gas.

In this model, the precalculated velocity $\mathbf{u}'$ does not meet the continuity condition ($\nabla \cdot \mathbf{u} = 0$), so $\mathbf{u}'$ should be modified for a divergence free velocity by:

$$\mathbf{u} - \mathbf{u}' = -\frac{\nabla p}{\rho} \tag{2-39}$$

$$\nabla \cdot \mathbf{u}' = \nabla \cdot \left(\frac{\nabla p}{\rho}\right) \tag{2-40}$$

where p is the pressure. The Poisson equation is solved in this work in the framework of lattice Boltzmann method:

$$h_\alpha^*(\mathbf{x} + \mathbf{c}_{\boldsymbol{\alpha}}, m+1) = h_\alpha^*(\mathbf{x}, m) - \frac{1}{\tau_{h^*}}[h_\alpha^*(\mathbf{x}, m) - \omega_\alpha p(\mathbf{x}, m)] - \frac{\omega_\alpha}{3}\nabla \cdot \mathbf{u}' \tag{2-41}$$

where $\tau_{h^*} = 0.5 + 1/\rho$, and m is the iteration number. The iterated pressure can be calculated as:

$$p(\mathbf{x}, m+1) = \sum_{\alpha} h_{\alpha}^{*}(\mathbf{x}, m+1) \tag{2-42}$$

and the iteration residual should meet the following condition before the modified velocity can be used for calculation:

$$|p(\mathbf{x}, m+1) - p(\mathbf{x}, m)| < \varepsilon \tag{2-43}$$

Landau free-energy equation [183, 184] is used in this model for partial wetting boundary condition:

$$\Psi_t = \int_V dV \left[\Psi(\phi) + \frac{\mathrm{k_f}(\nabla\phi)^2}{2}\right] \tag{2-44}$$

where $\Psi(\phi)$ is the bulk free-energy, while the term $\frac{\mathrm{k_f}(\nabla\phi)^2}{2}$ is the free energy contribution from density gradients in an inhomogeneous system. In this model, a new form of free energy is applied instead of the traditional van der Walls free energy. The free-energy density $\Psi(\phi)$ is assumed to be as follows in terms of isothermal system:

$$\Psi(\phi) = \beta(\phi - \phi_G)^2(\phi - \phi_L)^2 + \mu_b\phi - p_b \tag{2-45}$$

where β is a constant parameter concerned with the interfacial thickness; p_b is the bulk pressure. The chemical potential is defined as

$$\mu_c = \frac{\partial\Psi}{\partial\phi} = 4\beta(\phi - \phi_L)(\phi - \phi_G)(\phi - \phi_M) + \mu_b \tag{2-46}$$

where $\phi_M = (\phi_L + \phi_G)/2$; μ_b is the bulk chemical potential.

By combination of Eq. (2-46) and Eq. (2-34), here is

$$p_0 = \beta(\phi - \phi_L)(\phi - \phi_G)(3\phi^2 - \phi\phi_L - \phi\phi_G - \phi_L\phi_G) + p_b \tag{2-47}$$

The interface thickness D_i is represented as

$$D_i = \frac{4}{\phi_L - \phi_G}\sqrt{\frac{k_f}{2\beta}} \tag{2-48}$$

The liquid-gas surface tension σ_{LG} is given by

$$\sigma_{LG} = \frac{(\phi_L - \phi_G)^3}{6}\sqrt{2k_f\beta} \tag{2-49}$$

Cahn [195] reported that the solid/liquid interactions could be quite short-range, thus contributing a surface integral to the total free energy of the droplet. Therefore, the total free energy should be rewritten as

$$\Psi_t = \int_V dV\left[\Psi(\phi) + \frac{k_f(\nabla\phi)^2}{2}\right] + \int_S dS\,\Phi(\phi_s) \tag{2-50}$$

where ϕ_s is the order parameter on the wall, $\Phi(\phi_s)$ is the fluid/solid interaction contribution to the surface energy and S is the solid/liquid contact area.

Considering the one-dimensional problem, for $z > 0$ liquid or vapour phase is in this region, while for $z = 0$ there is the solid wall. Therefore, the order parameter will be ϕ_L or ϕ_G for the liquid/vapour phase and ϕ_s for the solid phase. Using $-\lambda\phi_s$ to replace $\Phi(\phi_s)$ for first order term of power series expansion, Eq. (2-50) can be modified as

$$\Psi_t = \int_V dV\left[\Psi(\phi) + \frac{k_f(\nabla\phi)^2}{2}\right] - \lambda\phi_s \tag{2-51}$$

Minimizing the total free energy equation Eq. (2-60)(2-51) via variational calculus with respect to boundary conditions for a droplet on a solid surface gives the following conditions:

$$\frac{\partial\Psi}{\partial\phi} - k_f\frac{d^2\phi}{dz^2} = \mu_b, \quad z > 0 \tag{2-52}$$

$$k_f\left(\frac{d\phi}{dz}\right) = \frac{d\Phi(\phi_s)}{d\phi_s} = -\lambda, \quad z = 0 \tag{2-53}$$

where λ is the wetting potential. Integrating Eq. (2-52) together with Eq. (2-45) results in

$$\frac{k_f}{2}\left(\frac{d\phi}{dz}\right)^2 = \beta(\phi - \phi_G)^2(\phi - \phi_L)^2 = W(\phi) \tag{2-54}$$

Incorporating Eq. (2-54) and Eq. (2-53), the order parameter on the wall can be determined as

$$-\lambda = \pm\sqrt{2k_f W(\phi_s)} \tag{2-55}$$

By solving Eq. (2-55), four solutions for ϕ can be obtained as

$$\phi_1 = \frac{\phi_L+\phi_G}{2} - \frac{\phi_L-\phi_G}{2}\sqrt{1+|\Omega_w|} \tag{2-56}$$

$$\phi_2 = \frac{\phi_L+\phi_G}{2} - \frac{\phi_L-\phi_G}{2}\sqrt{1-|\Omega_w|} \tag{2-57}$$

$$\phi_3 = \frac{\phi_L+\phi_G}{2} + \frac{\phi_L-\phi_G}{2}\sqrt{1+|\Omega_w|} \tag{2-58}$$

$$\phi_4 = \frac{\phi_L+\phi_G}{2} + \frac{\phi_L-\phi_G}{2}\sqrt{1-|\Omega_w|} \tag{2-59}$$

where Ω_w is the dimensionless wetting potential

$$\Omega_w = \frac{4\lambda}{(\phi_L-\phi_G)^2\sqrt{2k_f\beta}} \tag{2-60}$$

The surface tension between solid wall and fluid, σ_{SF}, can be written as

$$\sigma_{SF} = -\lambda\phi_s + \int\sqrt{2k_f W}\,d\phi \tag{2-61}$$

Then the following equations for surface tensions can be obtained as

for $\lambda > 0$

$$\sigma_{SG} = -\lambda\phi_2 + \int_{\phi_G}^{\phi_2} \sqrt{2\mathrm{k_f}W}\,\mathrm{d}\phi = -\lambda\frac{\phi_L+\phi_G}{2} + \frac{\sigma_{LG}}{2} - \frac{\sigma_{LG}}{2}(1-\Omega_w)^{\frac{3}{2}} \tag{2-62}$$

$$\sigma_{SL} = -\lambda\phi_4 + \int_{\phi_L}^{\phi_4} \sqrt{2\mathrm{k_f}W}\,\mathrm{d}\phi = -\lambda\frac{\phi_L+\phi_G}{2} + \frac{\sigma_{LG}}{2} - \frac{\sigma_{LG}}{2}(1+\Omega_w)^{\frac{3}{2}} \tag{2-63}$$

and for $\lambda < 0$

$$\sigma_{SG} = -\lambda\phi_1 + \int_{\phi_1}^{\phi_G} \sqrt{2\mathrm{k_f}W}\,\mathrm{d}\phi = -\lambda\frac{\phi_L+\phi_G}{2} + \frac{\sigma_{LG}}{2} - \frac{\sigma_{LG}}{2}(1-\Omega_w)^{\frac{3}{2}} \tag{2-64}$$

$$\sigma_{SL} = -\lambda\phi_3 + \int_{\phi_3}^{\phi_L} \sqrt{2\mathrm{k_f}W}\,\mathrm{d}\phi = -\lambda\frac{\phi_L+\phi_G}{2} + \frac{\sigma_{LG}}{2} - \frac{\sigma_{LG}}{2}(1+\Omega_w)^{\frac{3}{2}} \tag{2-65}$$

The wetting angle then can be determined as

$$\cos\theta_Y = \frac{\left[(1+\Omega_w)^{\frac{3}{2}} - (1-\Omega_w)^{\frac{3}{2}}\right]}{2} \tag{2-66}$$

For a given wetting angle the wetting potential Ω_w can be calculated as

$$\Omega_w = 2\mathrm{sgn}\left(\frac{\pi}{2} - \theta_Y\right)\left\{\cos\left(\frac{\gamma}{3}\right)\left[1-\cos\left(\frac{\gamma}{3}\right)\right]\right\}^{\frac{1}{2}} \tag{2-67}$$

where

$$\gamma = \arccos(\sin^2\theta_Y) \tag{2-68}$$

and $\mathrm{sgn}(x)$ is to give the sign of x.

To implement the partial wetting boundary condition for the phase field lattice Boltzmann model, the order parameter gradient near the wall should satisfy the follow condition:

$$\frac{\partial \phi}{\partial z}|_{z=0} = -\frac{\lambda}{\mathrm{k_f}} \tag{2-69}$$

$$\frac{\partial^2 \phi}{\partial z^2}|_{z=0} \approx \frac{1}{2}(-3\frac{\partial \phi}{\partial z}|_{z=0} + 4\frac{\partial \phi}{\partial z}|_{z=1} - \frac{\partial \phi}{\partial z}|_{z=2}) \tag{2-70}$$

The term $\frac{\partial \phi}{\partial z}|_{z=2}$ can be obtained using the following expression

$$\frac{\partial \phi}{\partial z}|_{z=2} \approx \frac{1}{2}(3\phi|_{z=0} - 4\phi|_{z=1} + \phi|_{z=2}) \tag{2-71}$$

For numerical simulation, the Young's angle θ_Y is pre-defined firstly, and then the wetting potential λ, which is used for partial wetting boundaries in Eq. (2-69), can be calculated from Eq. (2-67) and Eq. (2-60). The internal flow field can be solved by the phase field LB model with Eq. (2-26) – Eq. (2-43).

2.4 Results and discussion

The droplet motion on a square-post patterned micro surface, as shown in Fig. 2-2, is simulated in a liquid/gas two-phase system. The roughness parameters in this model are set as $a = d = h = 5\mu\mathrm{m}$. $-3\omega_\alpha \mathbf{c}_{\alpha 3}\left(1 - \frac{\rho_G}{\rho}\right)\mathrm{g_a}$ is added to the right side of Eq. (2-29) for simulation of gravity effect, and $\mathrm{g_a}$ means the nondimensional gravitational acceleration. The densities of liquid and gas are $\rho_L = 1000, \rho_G = 1.29$, and the viscosities of the two-phase fluids are $\mu_L = 10, \mu_G = 0.1935$, respectively. To achieve the real liquid/gas two phase system, the physical parameters are calculated with the transformational relations between the lattice units and the physical units: the lattice

length unit $L_0 = 1 \times 10^{-6}$m, the lattice time unit $T_0 = 1 \times 10^{-8}$s, and the lattice mass unit $M_0 = 1 \times 10^{-18}$kg. With the transformational relations, the natural dimensional physical parameters can be obtained: $\overline{\rho_L} = 1000\text{kg m}^{-3}, \overline{\rho_G} = 1.29\text{kg m}^{-3}, \overline{\mu_L} = 1 \times 10^{-3}\text{kg m}^{-1}\text{s}^{-1}, \overline{\mu_G} = 1.935 \times 10^{-5}\text{kg m}^{-1}\text{s}^{-1}$ and $\bar{g} = 9.8\text{m s}^{-2}$. The initial diameter of a spherical droplet is 60μm. The computational domain including solid surface and liquid droplet surrounded by gas are divided into $37 \times 37 \times 75$, which is quarter of the whole simulation region with symmetrical boundary condition applied. Unless otherwise specified, within a cuboid computational domain, the boundary conditions for the following simulation are set as: free outflow/inflow boundary conditions on the left, front and upper surfaces, symmetrical boundary conditions on the right and back surfaces, and non-slip boundary condition on the solid surfaces. The residual in Eq. (16) is $\varepsilon = 1 \times 10^{-6}$. The apparent contact angles for a droplet can be calculated by Eq. (2-1), Eq. (2-2), Eq. (2-4) and Eq. (2-6).

The critical Young's angle calculated by Eq. (2-6) in the model is 115.4°, therefore Young's angles of 105° for Wenzel state preferable and 130° for Cassie-Baxter state preferable are tested in this work. The figures in 2-D view in the rest of this chapter are the density distributions on the cross section where y-coordinate is 36μm.

2.4.1 Validation of the numerical model

To validate the numerical model, firstly the apparent contact angles of water droplets on a flat surface are tested after the two-phase systems reach static equilibrium in a $37 \times 37 \times 56$ computational domain, and the domain size has no effect on the simulated contact angle. As shown in Fig. 2-10, the apparent equilibrium contact angles are approximately 105° and 130°, which are almost the same as previously set. Following the apparent contact angles of water droplets on a square-post patterned

surface are tested as well, as shown in Fig. 2-11. For the first case where Young's angle is 105°, smaller than the critical angle, the wetting state is Wenzel state with the apparent contact angle of 119° in Fig. 2-11 (a), and the theoretical contact angle calculated by Eq. (2-2) is 121.2°; while when Young's angle is 130° and the wetting state is Cassie-Baxter state preferable, the simulated equilibrium apparent contact angle in Fig. 2-11 (b) is 160°, which is also very close to the theoretical value of 155.6° by Eq. (2-4). Fig. 2-11 (c) and Fig. 2-11 (d) present the droplets in 3-D view, from where it can be clearly seen that the grooves caused by roughness is waterlogged for the Wenzel state, while there is gas trapped between water liquid and solid surface for the Cassie-Baxter state. Hence, the numerical model can be used to study the wetting phenomena.

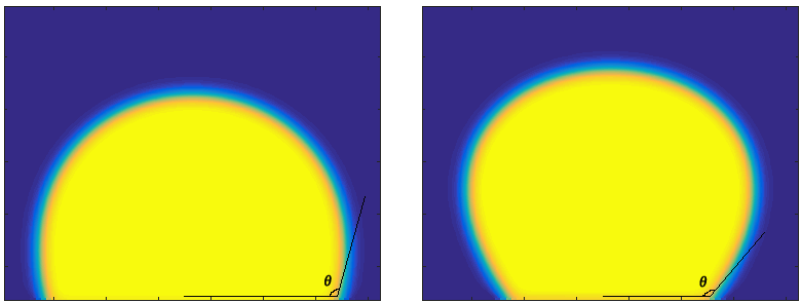

(a) (b)

Fig. 2-10 Droplets on flat surfaces with different Young's angles (a) $\theta_Y = 105°$, $\theta_{ap} \approx 105°$ (b) $\theta_Y = 130°$, $\theta_{ap} \approx 130°$

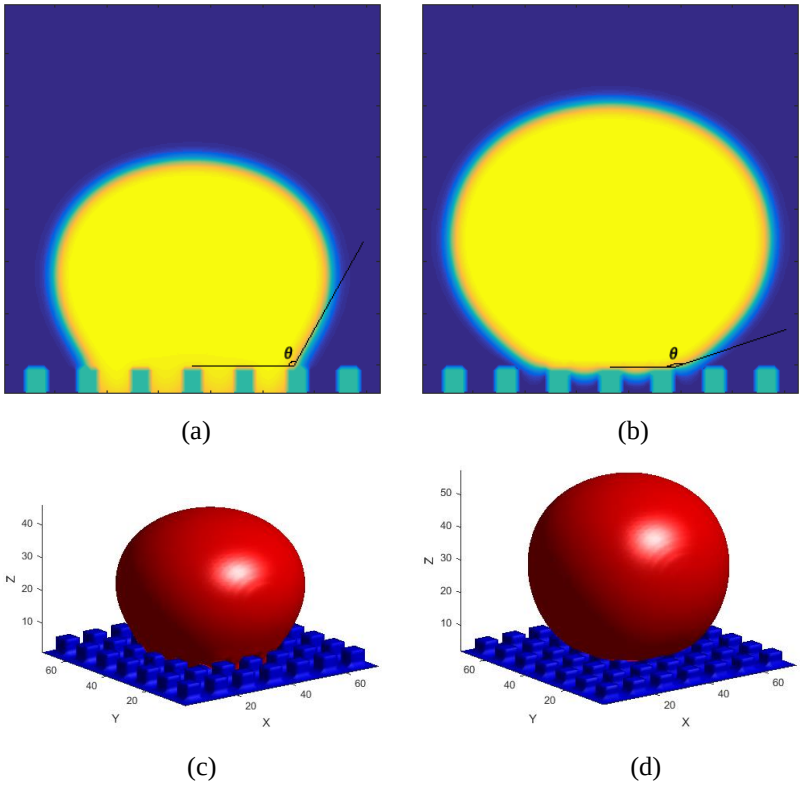

Fig. 2-11 Droplets on square-post patterned surfaces with different Young's angles (a) $\theta_Y = 105°$, $\theta_{ap} \approx 119°$, $\theta_{th} \approx 121.2°$, 2-D view (b) $\theta_Y = 130°$, $\theta_{ap} \approx 160°$, $\theta_{th} \approx 155.6°$, 2-D view (c) $\theta_Y = 105°$, 3-D view (d) $\theta_Y = 130°$, 3-D view

2.4.2 Wetting transitions

The Cassie-to-Wenzel wetting state transition is firstly simulated with a Wenzel state preferable Young's angle of $105°$, as shown in Fig. 2-12. To overcome the energy barrier [196], an initial velocity of $0.001\mathrm{m/s}$ is given and the initial height of the centre of the droplet is $60\mu\mathrm{m}$. From the pictures it can be seen that after about 1ms of the initial condition the droplet touches the upper surface of the square posts, presenting a Cassie-Baxter wetting state, and then the transition occurs. While the transition is in process, the droplet lower surface moves downward, keeping nearly horizontal until the inner parts touch the bottom solid surface. After approximately 2.4ms the transition process is completed. In the 1.4ms of the wetting transition process from Cassie-Baxter state to Wenzel state (1.00ms – 2.40ms), the time spent in moving down is about 1.34ms while the remaining 0.06ms is for soaking the bottom solid

surface, which means the latter process diminishes the free energy much more, in another word, the energy barrier mainly exists in the moving down process. This is consistent with the theoretical analysis in Patankar [152] Moreover, in the simulation the Cassie-to-Wenzel transition occurs only by depinning of the three-phase line, but the "sag transition" with pinning the three-phase line, which was predicted by Patankar [197] was not observed.

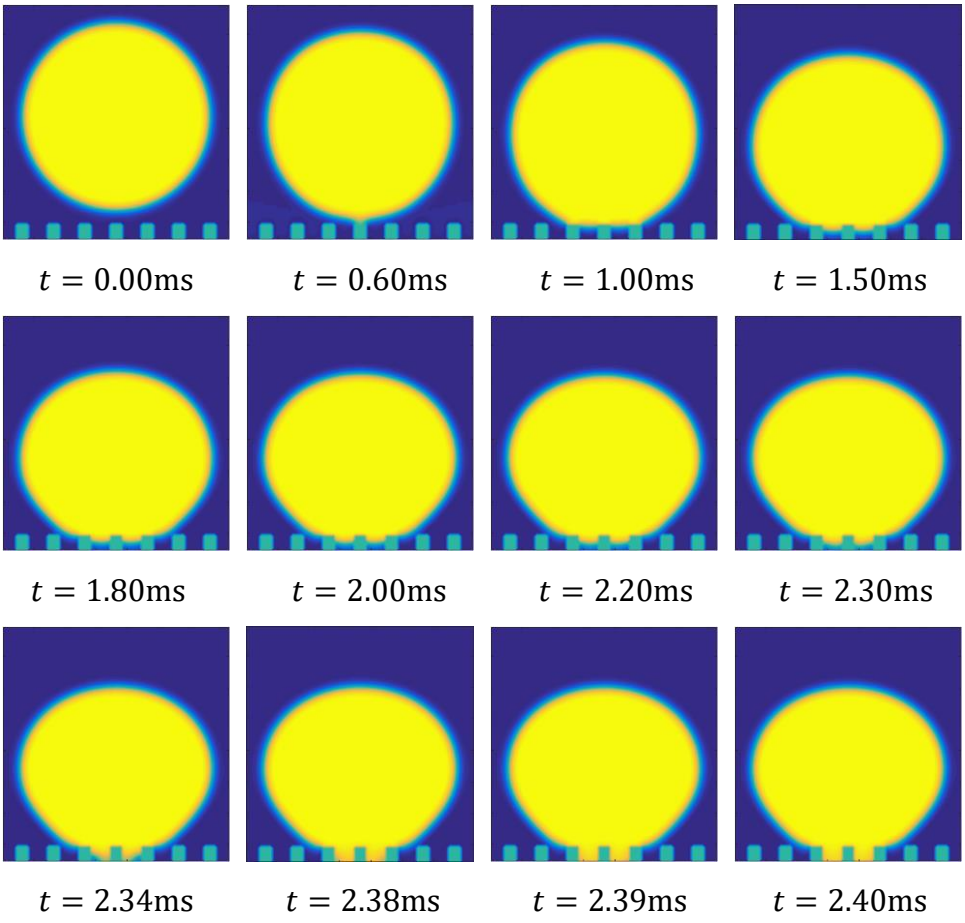

Fig. 2-12 Cassie-to-Wenzel wetting transition process, $\theta_Y = 105°$

The reverse transition from Wenzel state to Cassie-Baxter state, which is difficult to implement by experiment due to the unachievable initial state, is then tested with a Cassie-Baxter state preferable Young's angle of 130° in the numerical simulation, as shown in Fig. 2-13. The droplet is placed on the patterned surface with an initial condition of Wenzel state with water filled in the grooves, as shown in the first picture

when $t = 0\text{ms}$. It can be seen that the reverse transition route is quite different from the Cassie-to-Wenzel transition, which has a moving down process followed by the soaking bottom surface process. The reverse transition proceeds from the outer side of the post grooves to the inner side, and the liquid-solid-gas triple line moves in both horizontal and vertical directions. The whole transition takes places in around 1.60ms. This result indicate that the Wenzel-to-Cassie wetting transition process can occur spontaneously without any external forces such as heating so long as the inherent contact angle is large enough.

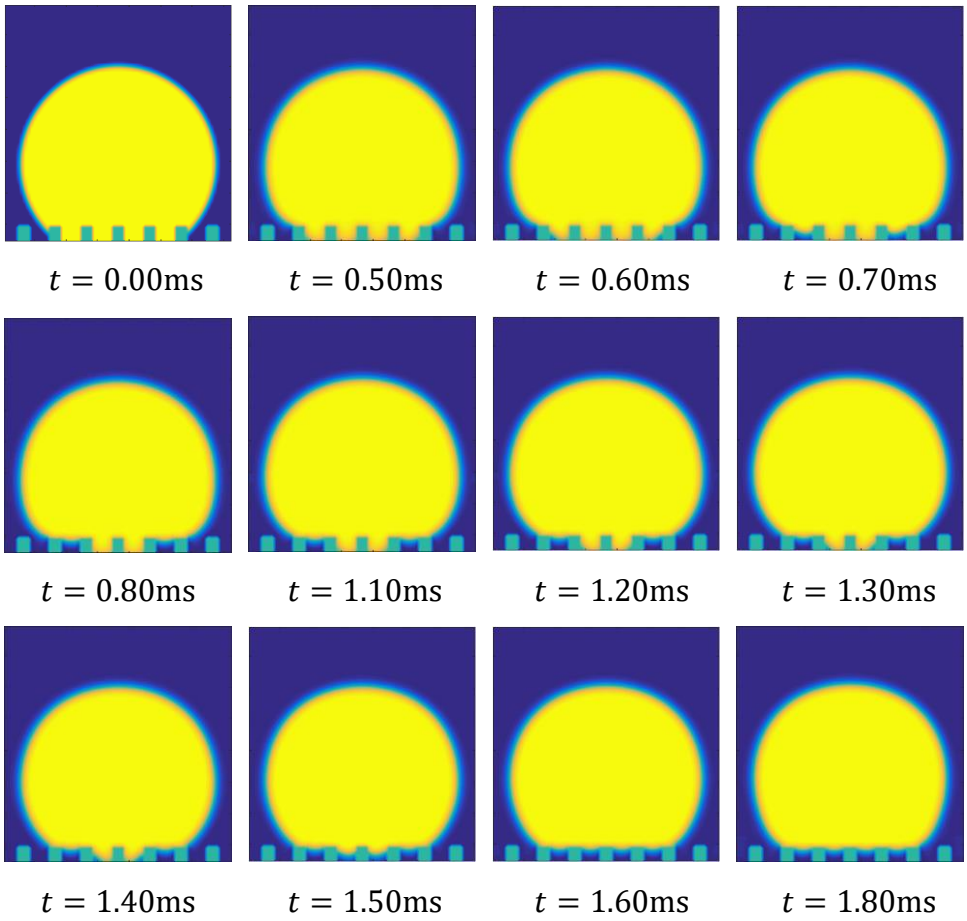

Fig. 2-13 Wenzel-to-Cassie wetting transition process, $\theta_Y = 130°$

It is generally agreed that the wetting transitions are irreversible [160]. For each case of the simulation work, the transition occurs along the same direction, from Cassie-

Baxter state to Wenzel state for a large Young's angle or the reverse transition for a smaller Young's angle, irreversible when no extra forces are loaded to the droplets.

2.4.3 Energy barrier

Although it has been observed in experiments that the Wenzel state and Cassie-Baxter state of droplets can coexist on the same surface [198], the manufactured surface cannot be as ideal as people expect, and the roughness of the manufactured posts or the hierarchy structure that cannot be eliminated completely may have influence on the existence of the energy barrier. However, in the numerical simulation there is no such a problem, as all the posts are ideally patterned. Two droplets are placed on the same surface with the same Young's angle of $105°$, with Wenzel wetting state and Cassie-Baxter wetting sate as the initial wetting conditions, respectively. No external forces such as initial velocity or pressure but gravity is loaded to the droplets. When achieving equilibrium states, as shown in Fig. 2-14, the Wenzel state and Cassie-Baxter state coexist, and no wetting transition happens spontaneously between the two droplets. This wetting phenomenon is firstly achieved by numerical simulation in this work, and it proves that the energy barrier exists from the simulation point of view by eliminating the factor of roughness on each post of any manufactured surface.

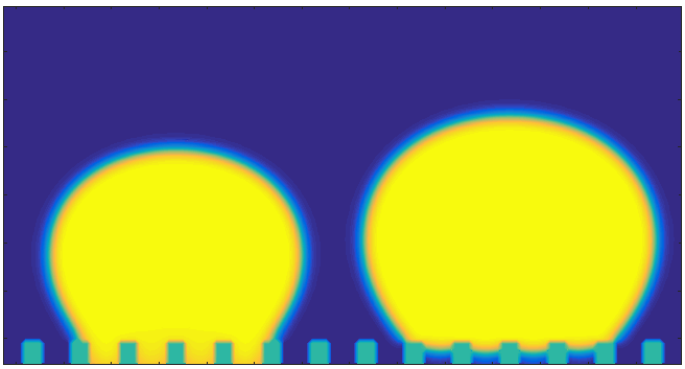

Fig. 2-14 Wenzel state and Cassie-Baxter state coexist on the same surface, $\theta_Y = 105°$

2.4.4 Gravity effect on wetting transition

In the microscale, gravity does not have an significant effect on the shape of a water droplet, but may be crucial to wetting transition [152]. During the Cassie-to-Wenzel transition process, the barycentre of the droplet declines, causing a decrease of the energy of the droplet, which can be a factor that overcomes the energy barrier. However, the gravity effect on wetting transition cannot be approved by experiments. In the numerical simulation, gravity can be loaded on the droplet or not just by changing the value of acceleration of gravity. Fig. 2-15 presents a specific case that the wetting transition is affected by the gravity effect when $\theta_Y = 102°$ after 0.90ms. Gravity is not loaded to the system in Fig. 2-15 (a) and loaded in Fig. 2-15 (b). It can be seen that after the same period of time, the wetting transition occurs for the droplet involving gravity but the other droplet is still in a Cassie-Baxter state. Although in the simulation the droplet without gravity in Fig. 2-15 (a) finally transited to Wenzel state, which may be triggered by the pseudo currents on the wall or a small velocity field caused by initialization, the results still indicate that gravity has a significant effect on wetting transition because the transition occurs much faster for the droplet with gravity.

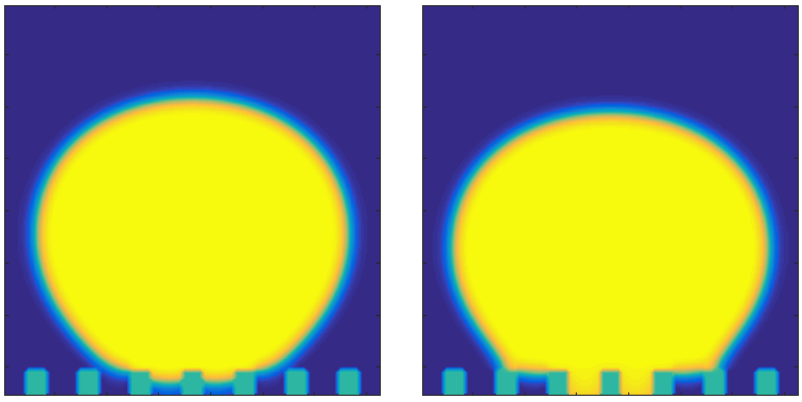

(a) (b)

Fig. 2-15 Gravity effect on wetting transition, $\theta_Y = 102°$, $t = 0.90$ms (a) without gravity (b) with gravity

2.5 Improving the micro structure of rough surface with truncated pyramid shape to impede wetting transition

2.5.1 Theoretical analysis

In this section the modified micro structure surface with truncated pyramid shape posts is applied to study the water droplet wetting states transitions, as shown in Fig. 2-16. Via the same process of theoretical analysis as previously introduced in Section 2.2, it can easily be concluded that by such modification of the micro structure posts, the critical state free energy could be raised up, which means the energy barrier between Cassie-Baxter wetting state and Wenzel wetting state is increased. In addition, from the theoretical analysis it can also be found that even when the intrinsic contact angle is lower than 90°, Cassie-Baxter state could also be achieved without any other extra external force.

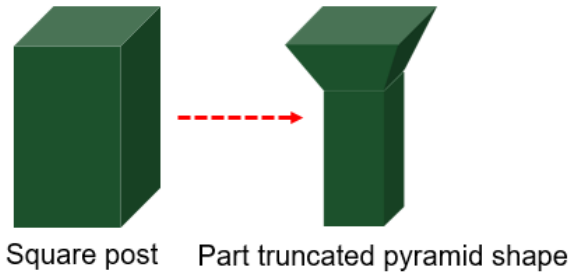

Fig. 2-16 From square post to the part truncated pyramid shape micro structure

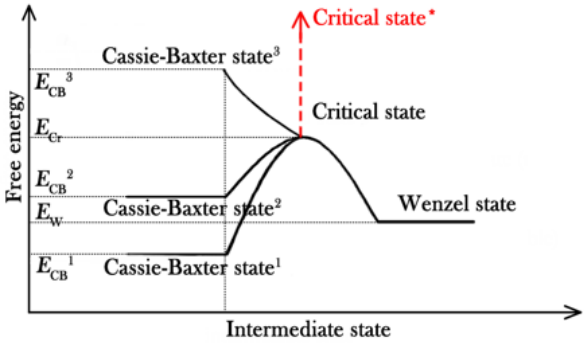

Fig. 2-17 Raising the critical state free energy and the energy barrier

2.5.2 Numerical simulation and discussion

Fig. 2-18 shows a group of 3D simulation results for water droplet on the modified micro structure surface with truncated pyramid shape posts. The intrinsic Young's angle is set as 85°, and there is no initial velocity loaded on the water droplet. It can be seen when the system is in steady state the Cassie-Baxter wetting state is still kept on the surface. The minimum intrinsic Young's angle for a steady Cassie-Baxter wetting state is 82° in this simulation work. This work indicates that the micro structure surface with truncated pyramid shape posts can impede the wetting transition, which is consistent with previous studies by other researchers [199].

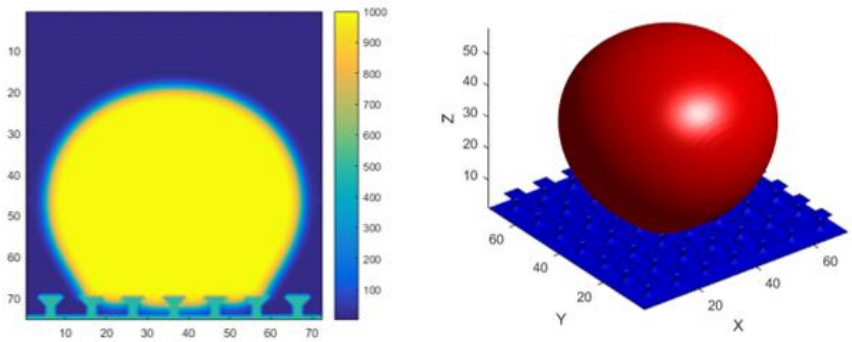

Fig. 2-18 3D simulation of a water droplet on the modified surface ($\theta_Y = 85°$)

2.6 Summary

In this work, the wetting transitions for a droplet on a square-post patterned surface are theoretically analysed. Numerical simulations with a phase field lattice Boltzmann method were carried out, and the results show good agreement with the theoretical analysis. The main finding of this work is that the energy curves during wetting transitions are proposed for Cassie-to-Wenzel transition together with the reverse transition via the theoretical analysis of the free energy changes during the transitions processes. The energy curves give a clear description of the conditions in which the transitions occur and the energy barriers exist for both transition processes. Gravity

effect for wetting transition is considered, and the energy curves illustrate that the gravity can be a driving force to trigger the transition. The irreversibility is discussed based on the energy curves presented. The Wenzel-to-Cassie transition can occur spontaneously only if the inherent contact angle is large enough. It can also be concluded from the curves that different routes of the Cassie-to-Wenzel transition and the reverse transition are the main reason for the irreversibility of wetting transitions. The work is mainly based on the regular square-post patterned surface, which is also the basis of most complicated rough surfaces. Therefore, the presented energy curves can be very helpful to understand the mechanism of complex wetting phenomena. Furthermore, the micro structure with truncated pyramid shape posts are studies using the theoretical analysis with the wetting transition energy curves, and the numerical simulation results show a good agreement with the theoretical analysis.

Chapter 3: Enhanced Oil-water Separation under Electric Field

3.1 Introduction

With the exploitation of oil fields, most of the early oil fields in the world have entered the high water cut or super high water cut stage, and the water content of the production liquid has reached 90% or even higher [200]. At present, the treatment of high-water-containing oil wells is to separate oil and water on the ground. Common oil-water separation methods include gravity separation, centrifugal separation, electric separation, air separation, etc. Although the ground oil-water separation technology has high separation efficiency and large processing capacity, in the above treatment methods, the oil-water mixture needs to be first lifted from the oil well to the ground, and then separated on the ground, which will bring a lot of problems. Those problems include the increase of storage cost, energy consumption as well as environmental pollution [201].

In recent years, the downhole oil-water separation (DOWS) technology has been developed to overcome the above-mentioned disadvantages of oil exploitation. In this technology, the water separated from the well is injected directly into the water injection layer of the well, while the oil is carried out simultaneously, and the separated rich oil with trace water is lifted to the ground surface [202, 203]. The DOWS technology presents an economic advantage in terms of reduction of water handling costs, providing extra capacity in surface facilities, and reduction of surface pollution [204]. Therefore, this approach is considered to be one of the viable options for achieving stable, economical and environmentally friendly mining of high water-

containing wells. There are three main approaches for the DOWS technology: gravity separation, hydrocyclone separation and membrane separation. Gravity separation takes advantage of the density difference of oil and water, and allows oil to rise upward, while it takes much time for separation process and the efficiency is relatively low. Hydrocyclone separation is also based on the difference of oil and water densities, but the separation is driven by the centrifugal force generated by the spinning fluid and the drag force on the moving droplets. The cost of hydrocyclone is relatively high and very small oil droplets are not easy to be separated using this technology. Membrane separation is the technology that fluid is driven through the membrane under significant fluid pressure, and the membrane is permeable to some specific components and impermeable to the others. However, it is limited in industrial applications due to the shortcomings such as membrane fouling, and different membranes needed for different wells [204, 205].

Although with relatively high expenses, hydrocyclone separation is the most widely used technology for DOWS [206]. The schematic diagram of hydrocyclones can be seen in Fig. 3-1. The oily water mixture enters from the upper part of the hydrocyclone and performs high-speed rotary motion in the cyclone. Under the action of centrifugal force, the heavier fluid, water, spins to the outside of the hydrocyclone and move towards the lower outlet of the cone. It flows out from the downstream outlet and is injected back into the water injection layer. While the oil with lower density enters the centre of the cyclone under centrifugal force to form a reflux, moves out from the upper outlet, and is pumped to the ground after being pressurized by the pump. Compared with the gravity separation DOWS system, the hydrocyclone has the advantages of immobile mechanical parts, light weight, high separation efficiency and stable performance, and for the same treated oil water mixture, it is much smaller than

the gravity separator and is more suitable for high water-containing oil wells [207]. However, because some oil droplets, especially some small droplets, are carried out along with the water downstream, the separation of oil and water in a hydrocyclone cannot be perfect. Therefore several hydrocyclones can be connected in series of in parallel to achieve better separation efficiency [208].

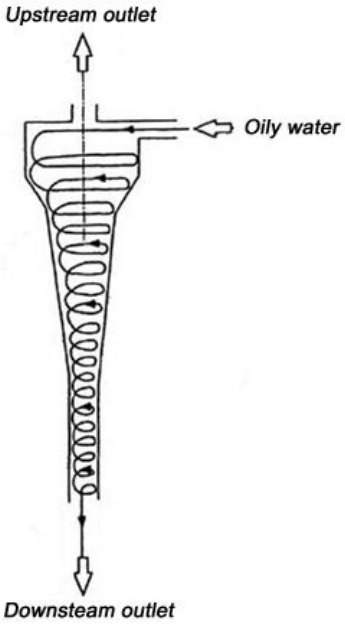

Fig. 3-1 Schematic diagram of hydrocyclones

The aim of this work is to enhance the oil water separation efficiency in hydrocyclone separation DOWS technology by focusing on the mechanism of oil droplets motions in hydrocyclones under electric fields. Mesoscale method is used to numerically study the dielectrophoresis force effect on oil droplets in water. Besides, experiment study is conducted as well to study the oil droplets motions under electric field.

3.2 Problem statement

In a high water cut well, the oil concentration in the hydrocyclone is very low, and the particle size of the oil droplets is usually under 100 micrometres. Considering that the

particle size and mass of the oil droplets are very small, and the water velocity in the cyclone is relatively high, the water carrying effect on the droplets then is obvious, and the movement of the oil droplets is seriously affected by the water movement. Therefore, the key to improve the separation efficiency of the cyclone is to reduce the carrying effect of water on the movement of small particle size droplets, and promote the reflux of small particle size oil droplets into the centre of the cyclone, so that it flows back from the upper outlet of the cyclone. Fig. 3-2 gives the hydrocyclone DOWS separation efficiency with respect to oil droplet diameter. It can be seen that the smaller the droplet size is, the lower the separation efficiency would be. The small oil droplets collide less because of their smaller cross-sectional area, and they have less momentum to overcome the energy barrier for coalescence during collision. Therefore, the improvement of small oil droplets separation efficiency has been a main issue for the hydrocyclone separation DOWS technology. In addition, because the flow in the hydrocyclone is quite complex, it is particularly important to further understand theoretical study of the separation mechanism and principle.

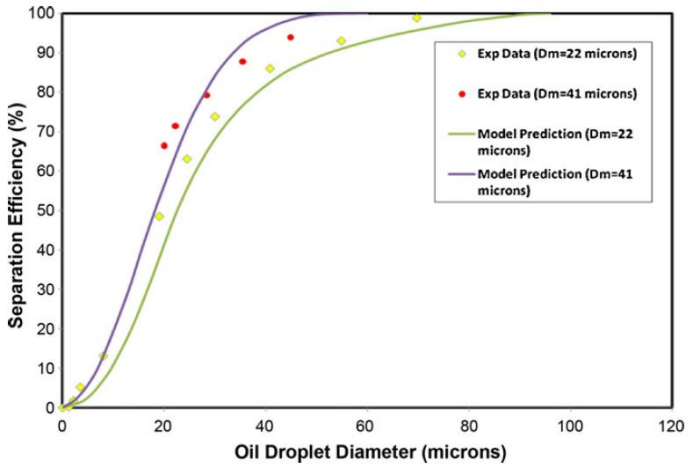

Fig. 3-2 Hydrocyclone DOWS separation efficiency with respect to oil droplet diameter [246] (copy right permitted)

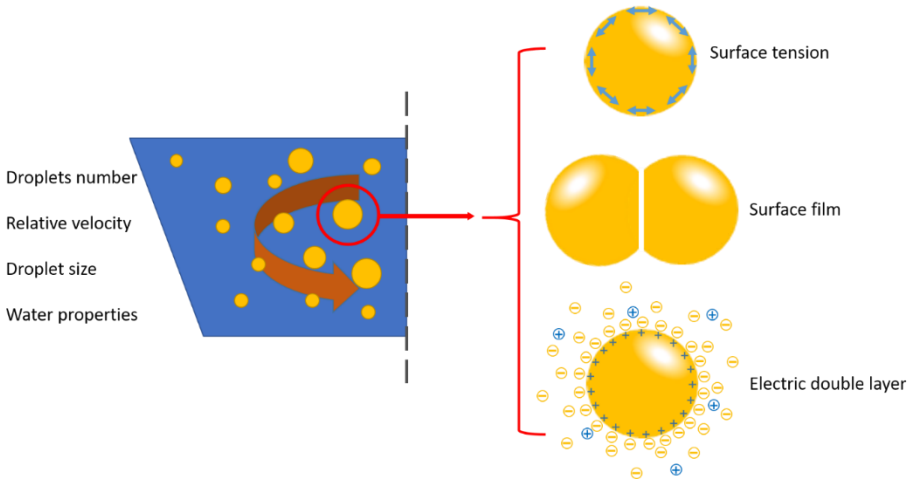

Fig. 3-3 Factors that affects droplets coalescence

3.3 Methodology

3.3.1 Numerical model

In this work the multicomponent multiphase (MCMP) lattice Boltzmann method is adopted for oil/water two-phase system. The lattice Boltzmann equations are solved under D2Q9 scheme for a 2-D simulation. The lattice step and time step are $\Delta x = \Delta t = 1$, and lattice sound speed $c_s = \frac{c}{\sqrt{3}}$, where $c = \frac{\Delta x}{\Delta t}$.

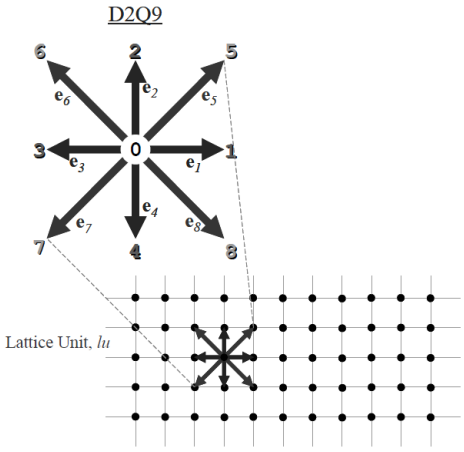

Fig. 3-4 D2Q9 lattice Boltzmann scheme

The lattice Boltzmann equation for multicomponent multiphase flow can be described as follows:

$$f_\alpha^i(\mathbf{x}+\mathbf{e}_\alpha\Delta t, t+\Delta t) = f_\alpha^i(\mathbf{x},t) - \frac{f_\alpha^i(\mathbf{x},t)-f_\alpha^{i,eq}(\mathbf{x},t)}{\tau_i} \tag{3-1}$$

where $f_\alpha^i(\mathbf{x},t)$ is the density distribution function of component i in the αth direction. The unit vector $\mathbf{e}_\alpha$ is given as

$$\mathbf{e}_\alpha = \begin{bmatrix} 0 & 1 & 0 & -1 & 0 & 1 & -1 & -1 & 1 \\ 0 & 0 & 1 & 0 & -1 & 1 & 1 & -1 & -1 \end{bmatrix} \tag{3-2}$$

And the distribution function is defined as

$$f_\alpha^{i,eq}(\mathbf{x},t) = w_\alpha \rho_i \left[1 + 3\frac{\mathbf{e}_\alpha \mathbf{u}_i^{eq}}{c^2} + \frac{9}{2}\frac{(\mathbf{e}_\alpha \mathbf{u}_i^{eq})^2}{c^4} - \frac{3}{2}\frac{\mathbf{u}_i^{eq^2}}{c^2}\right] \tag{3-3}$$

The macroscopic densities and velocities can be obtained by

$$\rho_i = \sum_\alpha f_\alpha^i \tag{3-4}$$

$$\mathbf{u}_i^{eq} = \mathbf{u}' + \Delta\mathbf{u} = \mathbf{u}' + \frac{\tau_i \mathbf{F}_i}{\rho_i} \tag{3-5}$$

where

$$\mathbf{u}' = \frac{\sum_i \sum_\alpha \frac{f_\alpha^i \mathbf{e}_\alpha}{\tau_i}}{\sum_i \frac{1}{\tau_i}\rho_i} \tag{3-6}$$

$$\mathbf{F}_i = \mathbf{F}_{int,i} + \mathbf{F}_{ads,i} + \mathbf{F}_{g,i} + \mathbf{F}_{e,i} \tag{3-7}$$

where $\mathbf{u}'$ is the mutual velocity of the two components, and $\mathbf{F}_i$ is the force acting on the single component, including particles interaction force $\mathbf{F}_{int,i}$, adhesion force between liquid phase and solid phase $\mathbf{F}_{ads,i}$, gravity acceleration $\mathbf{F}_{g,i}$ and electrical force $\mathbf{F}_{e,i}$.

The particles interaction force for this multi-component model is

$$\mathbf{F}_{int,i}(\mathbf{x}) = -G\,\Psi_i(\mathbf{x},t)\sum_{\alpha=1}^{8} w_\alpha \Psi_{\bar{i}}(\mathbf{x}+\mathbf{e}_\alpha\Delta t, t)\mathbf{e}_\alpha \tag{3-8}$$

where G is the interaction force intensity, $\Psi_i = \rho_i$ is the pseudopotential of component *i*, and w_α is the weight for αth direction, which is

$$w_\alpha = \begin{cases} \frac{4}{9} & \alpha = 0 \\ \frac{1}{9}\alpha = 1,2,3,4 \\ \frac{1}{36}\alpha = 5,6,7,8 \end{cases} \tag{3-9}$$

The governing equation for static electric field is

$$\nabla \cdot (\varepsilon_e \nabla \phi_e) = 0 \tag{3-10}$$

$$\mathbf{E} = -\nabla \phi_e \tag{3-11}$$

where ϕ_e is the electric potential, $\mathbf{E}$ is the electric field intensity, ε_e is the permittivity. The electric field equation is a Poisson equation, which can be solved using different numerical methods. In this work for a unified solution, the equation is also discrete using LB scheme, and the corresponding LB equation is shown as follow

$$h_\alpha(\mathbf{x} + \mathbf{e}_\alpha, m+1) = h_\alpha(\mathbf{x}, m) - \frac{h_\alpha(\mathbf{x},m) - h_\alpha^{eq}(\mathbf{x},m)}{\tau_e} \tag{3-12}$$

where m is iteration number, and there are

$$h_\alpha^{eq}(\mathbf{x}, m) = w_\alpha \phi_e(\mathbf{x}, m) \tag{3-13}$$

$$\tau_e = \varepsilon_e + 0.5 \tag{3-14}$$

The electric potential can be expressed as

$$\phi_e(\mathbf{x}, m+1) = \sum_\alpha h_\alpha(\mathbf{x}, m+1) \tag{3-15}$$

Then the electric field force can be described as

$$\mathbf{F}_{e,i} = -\frac{1}{2}\mathbf{E}^2 \nabla \varepsilon_e + \frac{1}{2}\nabla \left[\mathbf{E}^2 \left(\frac{\partial \varepsilon_e}{\partial \rho} \right)_T \rho \right] \tag{3-16}$$

where the first term in the right hand of the equation is dielectrophoresis force, and the second term is the electrostrictive components of the electric body force [209].

3.3.2 Experiment setup

Experiment study was carried out to investigate the electric field effect on oil/water separation. Fig. 3-5 shows the experiment process for mixing oil and water. 10% tap water and 90% Petronas Syntium 5000 DM 5W-30 Oil were used for the oil/water mixture. Gallenkamp magnetic stirrer and Sonics CV334 ultrasonic liquid processor were used together to mix the liquid. Fig. 3-6 is the experiment setup for observation. ISO-TECH IPS4303 latoratoru DC power supply is adopted to provide the electric field, and Optika 4083.CL5 microscope is used for observing the oil/water mixture motions. Two copper electrodes are pasted on a glass slide, and the oily water droplet is dript onto a glass slide and then covered with another glass slide, which makes the viewing zone under microscope, as shown in Fig. 3-7.

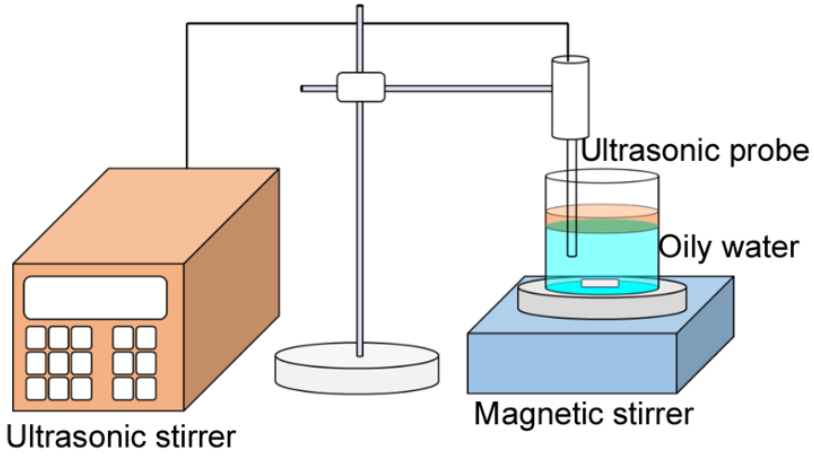

Fig. 3-5 Experiment setup schematic diagram for mixing oil and water

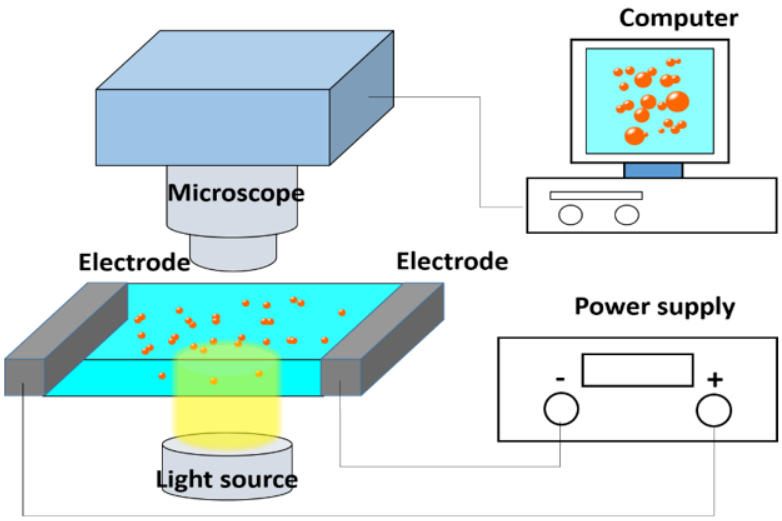

Fig. 3-6 Experiment setup schematic diagram for oil-in-water motion under electric field

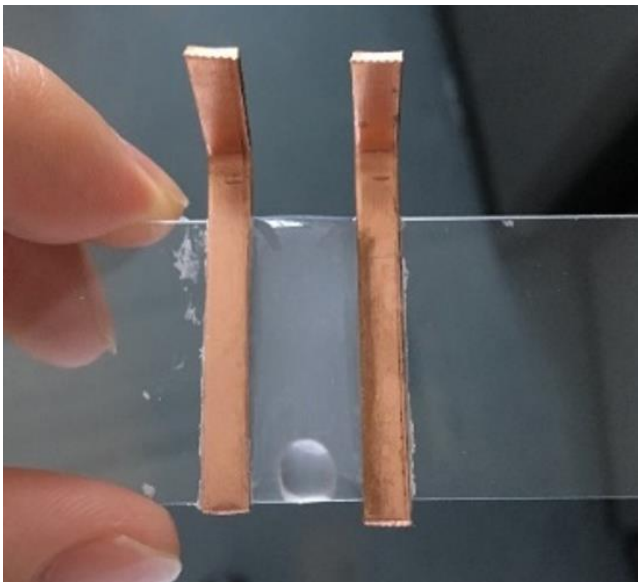

Fig. 3-7 viewing zone with oily water between copper electrodes

3.4 Results and discussion

3.4.1 Validation of the numerical model

The numerical calculations in this work are all carried out under the standard lattice unit. The physical quantity can be obtained by the conversion between the lattice unit and the physical unit. The conversion relationship is the length unit $L_0 = 1 \times 10^{-7}$m, the mass unit $M_0 = 5 \times 10^{-19}$kg, time unit $T_0 = 1.33 \times 10^{-9}$s, electric potential unit $U_0 = 5.3355\text{V}$, electric resistance unit $R_0 = 1.3395 \times 10^{7}\Omega$, electromagnetic field

strength unit $B_0 = 7.1 \times 10^5$T. The simulation area is $20\mu m \times 15\mu m$. The electrodes are located on the upper and lower sides of the simulation domain, and the electric charges are evenly distributed. The upper and lower boundaries are solid non-slip boundary, and the left and right are periodic boundaries, as shown in Fig. 3-8.

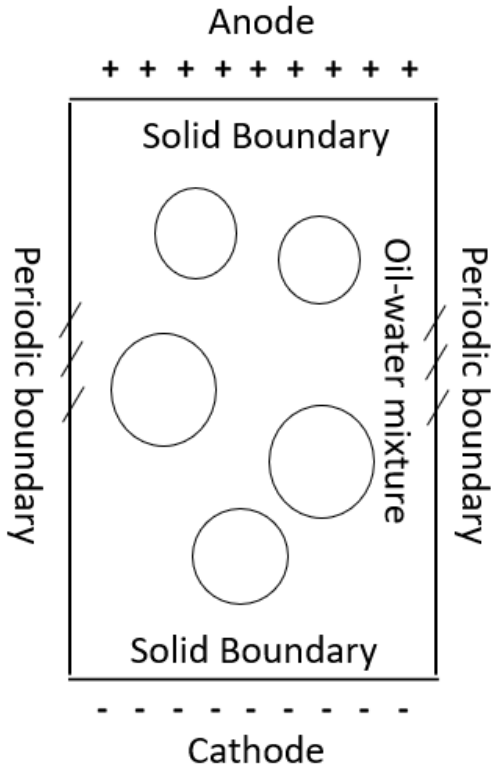

Fig. 3-8 Numerical model settings for oil/water two phase system

The deformation of a single water droplet under the action of a strong electric field was simulated, as shown in Fig. 3-9. The initial diameter of the water droplet was $8\ \mu m$, the applied voltage was $266.8\ V$, and the electric field strength was $0 - 133.4\ kV/cm$. It can be seen that the water droplet is deformed under the action of the electric field, which is consistent with the experimental phenomenon shown in Fig. 3-10. The droplet diameter measured in Fig. 3-10 was $3.15\ mm$, and the electric field intensity was $0 - 1.2\ kV/cm$. The deformation of water droplet is related to the polarization of water molecules under the action of an electric field, and the direction of extension is parallel

to the direction of the electric field. It can be known from previous research work that the smaller the diameter of the water droplet, the less likely it is to deform. The diameter of the droplet in Fig. 3-10 is about 400 times the diameter of the droplet in Fig. 3-9 and the electric intensity is around 110 times, which produces a similar deformation of water droplet. Besides, the different conditions between the simulation and experiment might be the reason that the deformation speed of the simulation is rapider than that from the experiment.

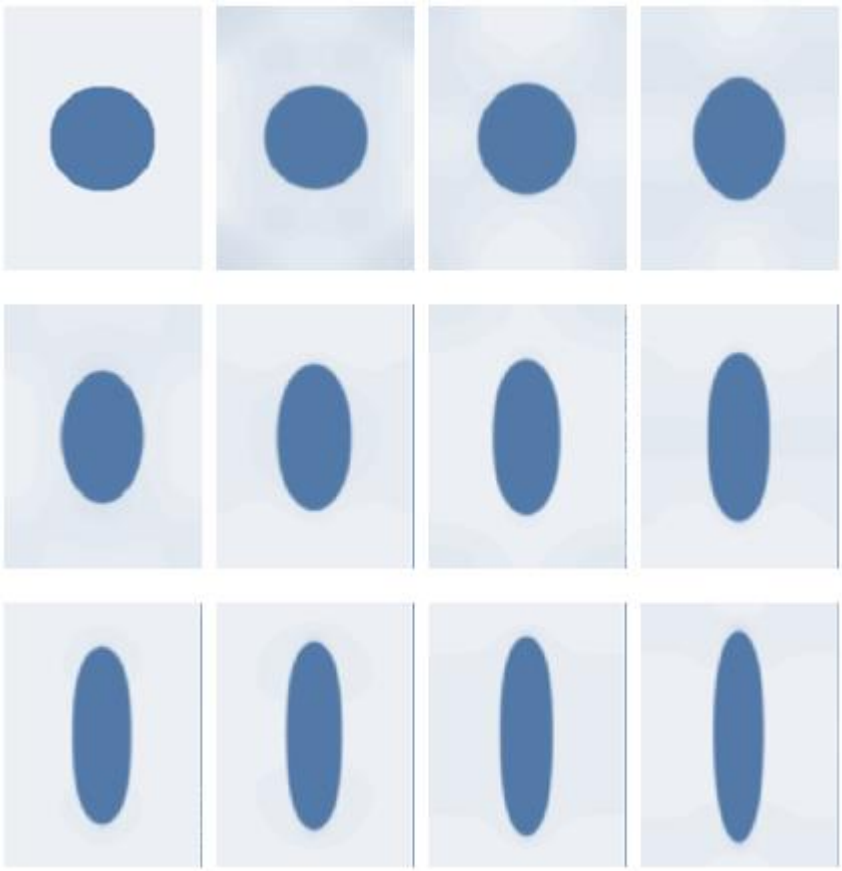

Fig. 3-9 Simulation for the deformation of a water droplet in oil under electric field

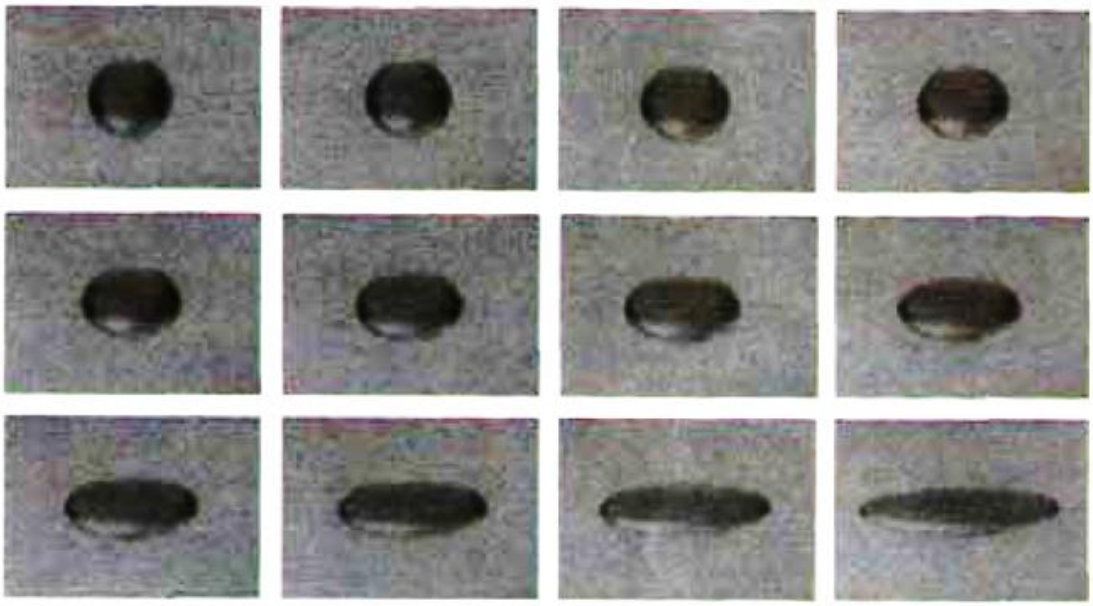

Fig. 3-10 Experiment for the deformation of a water droplet in oil under electric field [210] (copy right permitted)

Fig. 3-11 simulates the motion of two water droplets under the action of an electric field. It can be seen from the figure that the water droplets are polarized, resulting in a relative motion. Finally, the two droplets attract each other from the initial velocity of 0 and merge into one large one. The simulated droplets motion is consistent with previous experimental studies [211].

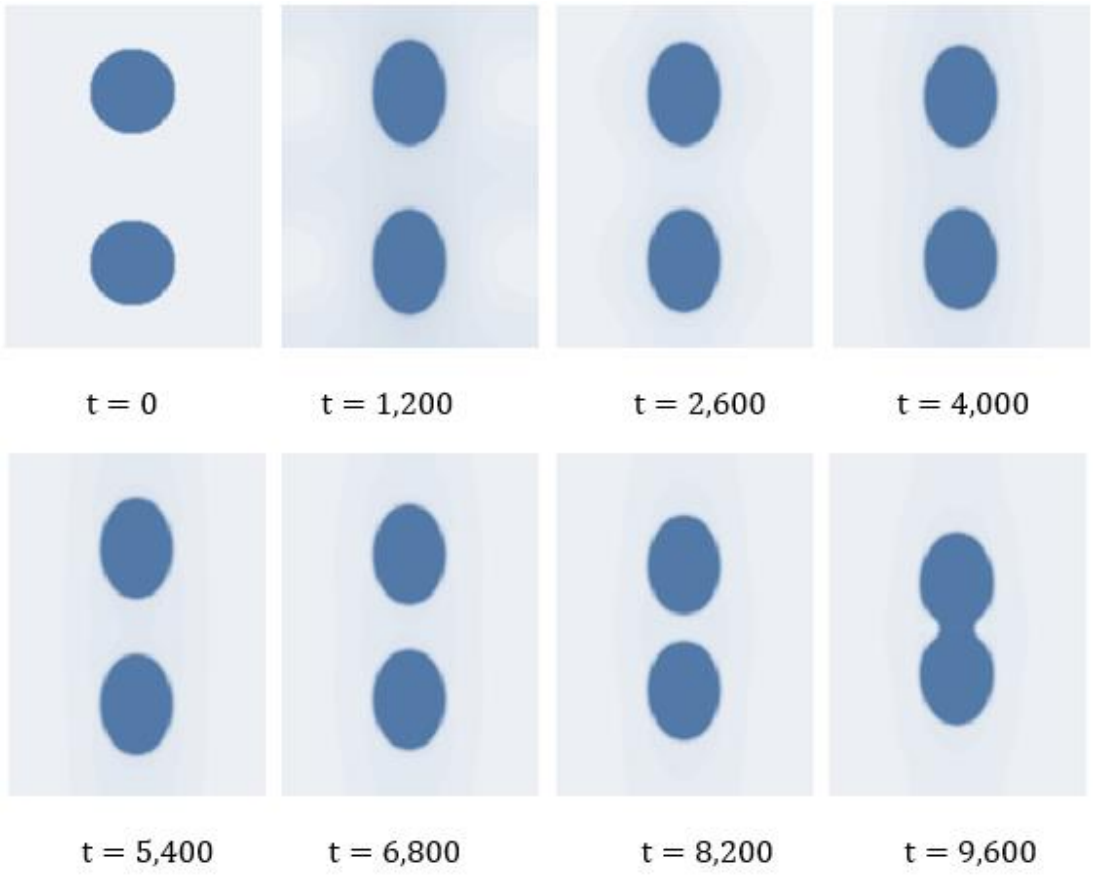

Fig. 3-11 Simulation for two water droplets moving towards each other under electric field

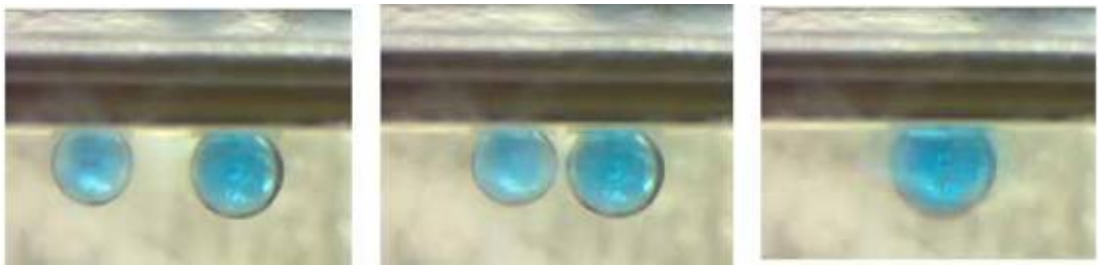

Fig. 3-12 Experiment for two water droplets moving towards each other under electric field [211] (copy right permitted)

In order to separately investigate the effect of water molecules on the movement of oil droplets under electric field, it is assumed that there is no free charge in water, so that the motion of water is completely caused by the polarization of water molecules. As shown in Fig. 3-13, four oil droplets are placed in the calculation area of 20μm × 15μm, the initial speed of the system is set to 0, and the upper and lower electrodes are added

with a voltage of 0.004V. After a period of electric field action, the oil droplets aggregated into one large oil droplet.

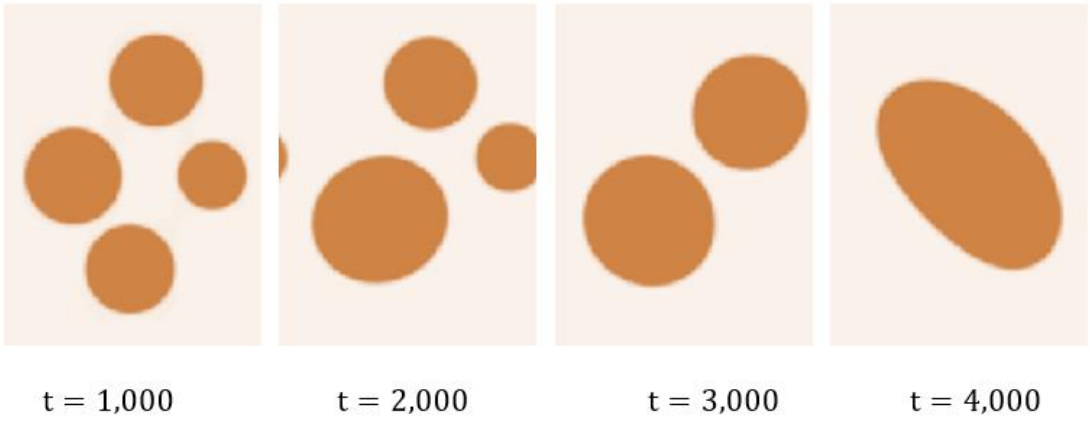

Fig. 3-13 Dielectrophoresis force effect on oil droplets, $\mathrm{E} = 200\mathrm{V/m}$

Fig. 3-14 shows the electric field potential and the electric force distribution of the oil/water mixture system at $\mathrm{t} = 1{,}000$. As can be seen from the figure, since the water phase has a strong polarity compared to the oil, the electric intensity is much lower in the water compared to that in the oil phase. The heterogeneous distribution of the electric field generates an electric field force in the water, especially near the oil-water interface, and it drives the movement of the water molecules, thereby causing the oil droplets to move passively. This phenomenon can be explained by Fig. 3-15. Water molecules are polarized under the action of an electric field, and weak electric field forces exist between polarized water molecules. In order to reach the most stable state, water molecules move and thus drive oil droplets movement. The oil/water interface decreases after oil droplets aggregation, and the system energy is reduced, which makes it more stable. The simulation also found that under strong electric field (on the order of $1\mathrm{kV/cm}$), oil droplets would deform and stretch toward the poles (see Fig. 3-11). This phenomenon can also explain the role of water molecules after polarization. The oil droplet's stretching is consistent with the total system energy decreasing, and

when the oil droplet's surface tension is in balance with the electric force the system reaches equilibrium state.

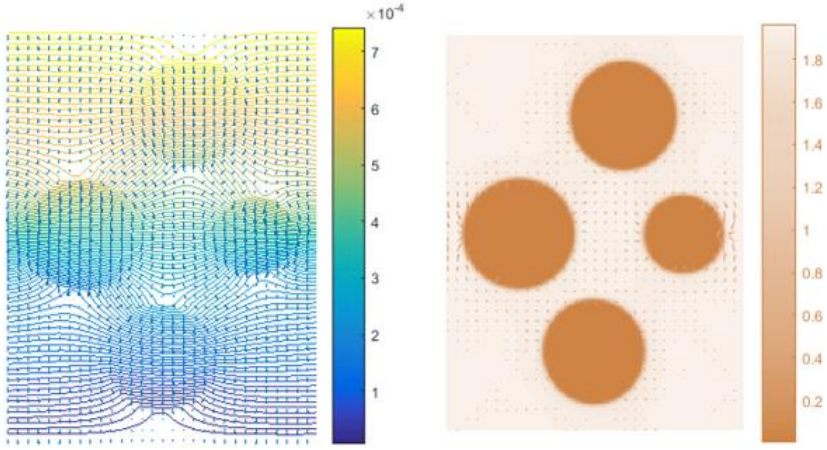

(a) (b)

Fig. 3-14 Electric field effect on oil/water system (a) electric potential distribution (b) electric force distribution

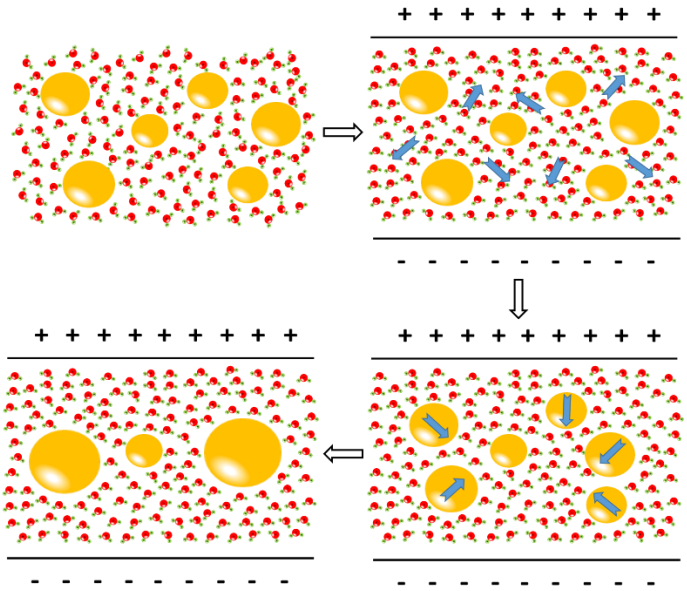

Fig. 3-15 Dielectrophoresis schematic diagram in an oil-in-water system

3.4.2 Oil droplets motion under electrical field

The oil/water system is mixed by 20 minutes using the magnetic stirrer and the ultrasonic liquid processor to make sure the two phases are fully mixed. Fig. 3-16 is a sample of the mixed oily water with 10% oil inside. Fig. 3-17 shows the microscope

view of the oil/water mixture. It can be seen in the picture that almost all of the oil droplets diameters are smaller than 100μm, which are hard to be separated in the DOWS hydrocyclone.

Fig. 3-16 Oil/water mixture sample

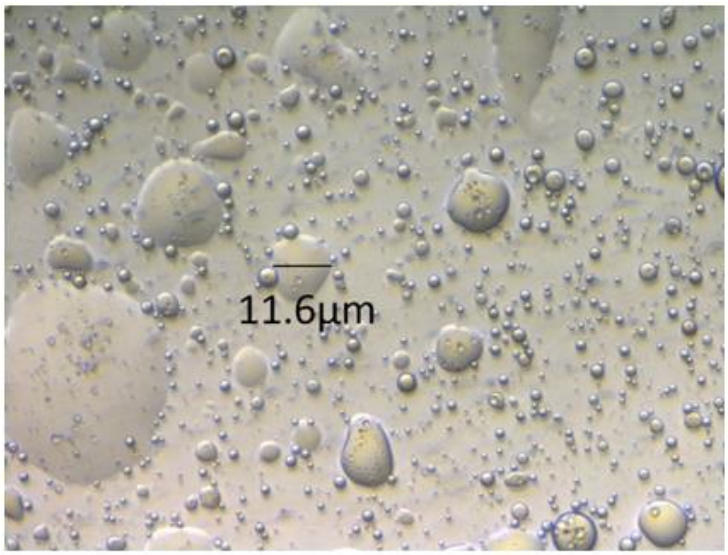

Fig. 3-17 The oil/water mixture under microscope

The arrows in Fig. 3-18 give the oil droplets motion directions. After power is turned on, the oil droplets start to move towards the anode immediately. Fig. 3-19 shows the test section change after 7 minutes under a 5V electric voltage, where it can be seen the oily water in clearer than its initial state. The light blue line in the middle of the test section after 7 minutes of electric field applied might be $Cu(OH)_2$, because it is

blue floc and the cathode is copper. The oil droplets moving towards anode is electroosmosis phenomenon, which occurs because the two glass slides form a narrow fluid conduit, and the cations are absorbed by the glass surfaces due to its chemical properties for chemical equilibrium, and the remaining anions cause an apparent negative electric property. Therefore, the oil/water mixture moves towards anode induced by the resulting Coulomb force from the electric field applied.

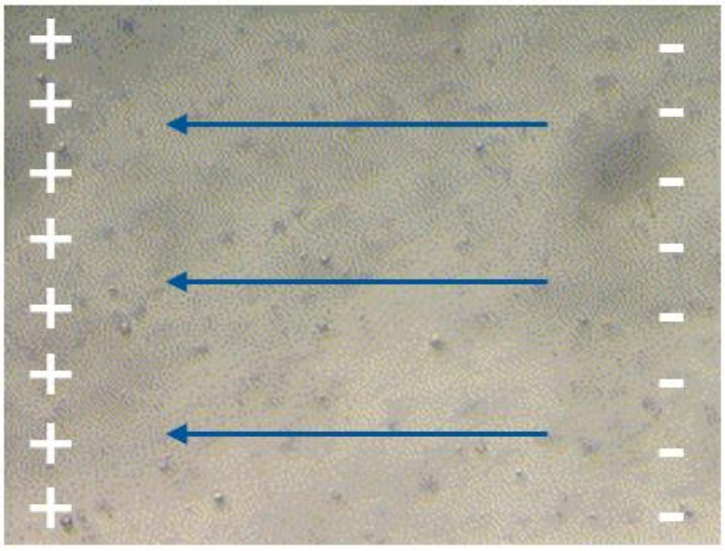

Fig. 3-18 The oil droplets motions under electric field

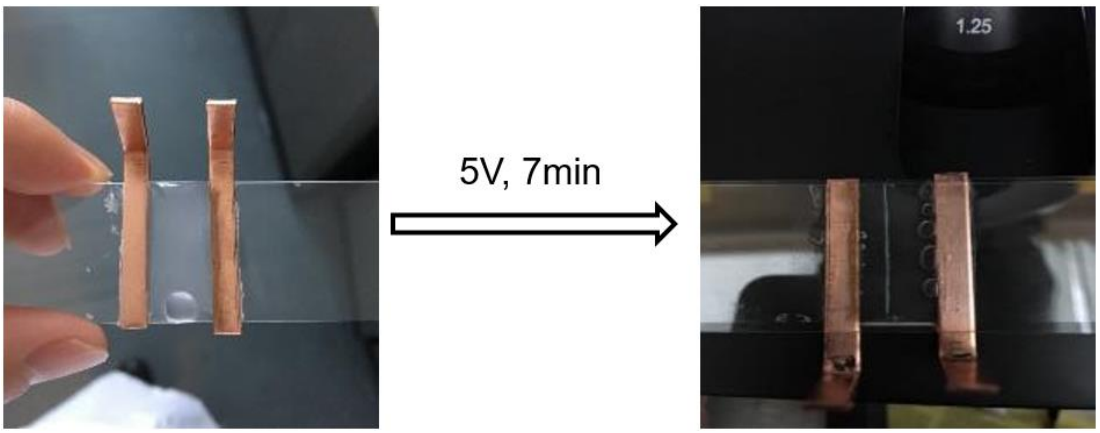

Fig. 3-19 Oil/water mixture change after loading electric field

It should be noted that the electroosmosis phenomenon here in this experiment is different from the common electroosmosis phenomenon where the oil droplets should move towards cathode through the same glass slides conduit. The reason is that the

common electroosmosis occurs when the fluid is connected with external fluid, and there is electric equilibrium in the fluid far from the conduit surfaces, thus the electric double layers become the leading factor that drives the fluid to flow towards the cathode. However, in this case in the experiment, there are limited ions in the test section and it is a closed system, so when the cations are absorbed by the glass slides surfaces, the remaining anions become the main factor that drives the fluid to flow towards the anode.

In addition, the dielectric force effect simulated in the previous section is not observed in the experiment, since the dielectrophoresis phenomenon is quite weak and hard to be observed under a low applied electric voltage. Due to safety and economy issue a strong voltage in DOWS technology is unpractical.

3.5 Summary

In this work a multicomponent multiphase (MCMP) lattice Boltzmann method is proposed for oil/water two-phase system under electric field by coupling the electrostatic field equation, which is also resolved in lattice Boltzmann scheme. The numerical model is firstly verified by simulating the single water droplet deformation and double droplets attracting each other in oil under strong electric field and comparing with experiment results. Both numerical and experiment studies are carried out to study the electric field force on oil droplets motions in water.

Chapter 4: Mesoscale Simulation of Boiling Heat Transfer

4.1 Introduction

Boiling heat transfer is a very common way for heat transfer enhancement both in our daily life as well as in industrial applications and nucleate boiling has been recognized as one of the most effective heat transfer approach which has been utilized in an extensive field of applications in energy conversion and heat exchange systems. Experimental studies about boiling heat transfer have been conducted for decades [212], but it is still a quite hot research topic all over the world due to its extremely complex physical process. Apart from experimental investigation, numerical simulations have also been conducted. Some numerical models based on Navier-Stokes equations such as volume of fluid (VOF) model or level set (LS) have been reviewed in references [213, 214].

The first liquid-vapour phase change LB model based on pseudopotential model might be attributed to Zhang and Chen [215], who presented the model which has the capability of thermodynamic multiphase flow simulation and successfully achieved liquid-vapour boiling process. Then Hazi and Markus [216] proposed another thermal pseudopotential model in which an energy equation depicting the local balance law for entropy was coupled. They derived the target temperature equation from the entropy-based energy equation and the thermodynamic relationship of non-ideal gases, and gave the corresponding thermal LB equation. Evaporation through a plane interface and two-phase Poiseuille flow were simulated using their thermal LB model [217]. Biferale et al. [218] presented an LB based thermal model in multiphase flow (boiling) and performed a series of 3D simulations at the Rayleigh number $Ra \sim 10^7$. The

exponential-form pseudopotential was adopted in their model and the non-ideal equation of state was not employed. Gong and Cheng [219, 220] proposed an LB phase change model for simulation of pool boiling. This model has been used to study bubble nucleation, growth, departure, and surface wettability effects on pool boiling heat transfer [221, 222], and also been applied to simulate film condensation [223]. Study from Li and Luo [224] showed that the error term in the recovered energy equation by thermal LB equation can generate nonnegligible numerical errors, and then Li et al. [225] developed a new thermal pseudopotential LB model in a hybrid scheme where the entropy-based temperature equation was solved by a finite-difference method. Recently Li et al. [226] points out the replacement of $\nabla \cdot (\lambda \nabla T)/\rho c_v$ with $\nabla \cdot (\alpha \nabla T)$ in some existing thermal LB models is not appropriate. They then improved the thermal LB model for liquid-vapour phase change and some error terms existing in the recovered macroscopic temperature equation in some models are also eliminated in their model. Gong and Cheng [227] studied boiling heat transfer with conjugate thermal boundary condition, and the thermal energy equation is addressed in this work. It has also been reported [228] that using the entropy-based energy equation can effectively slow down the small bubble shrinkage issue. Zhang et al. [229] focused on the effects of surface wettability on boiling heat transfer and found an optimal relation between temperature and surface wettability. A list of recent development of pseudopotential boiling heat transfer models can be found in Table 1.

The boiling models has also been developed based on phase field LB model. In 2009, Dong et al. [230] proposed a new thermal model to study a single rising bubble. The model was based on Zheng et al.'s phase-field model [231] for large density ratio, and a source term $-\frac{\rho_l(\rho_l-\rho_v)}{\rho_v}\frac{Ja}{Pe}\nabla^2 T$ is added to the recovered Cahn-Hilliard equation, where $Ja = c_{p,l}(T_{sat} - T_\infty)/h_{lv}$ and $Pe = UL/\alpha$ is the Peclet number, in which h_{lv} is

the latent heat of vaporization, U is the characteristic velocity, L is thechracteristic length. This model was developed to 3D model by Sun and Li [232] in 2013. Tanaka et al. [233] and Sattari et al. [234] achieved nucleate boiling simulation using the model proposed by Inamuro et al. [185], where a Cahn-Hilliard-like equation is employed. Begmohammadi et al. [235] accomplished the pool boiling using the liquid-vapour phase change model developed by Safari et al. [236]. In this model, the source term $-\frac{m'}{\rho_l}$ where $m' = \lambda \nabla T \cdot \nabla \phi / h_{lv}$ is added to the Cahn-Hilliard equation. They then extended this model to accomplish film boiling for the first time using phase-field LB model [237]. Sadeghi et al. [238] modified this model to 3d simulation, and in their work effects of different parameters including, Jacob number, gravitational acceleration and surface tension on bubble departure diameter were all considered. A list of recent development of pseudopotential boiling heat transfer models can be found in Table 2.

This work focuses on the pseudopotential LB models for phase change heat transfer simulation. The term $\frac{\partial p_{EOS}}{\partial T}$ is simplified in Li et al. [226], and it is found that such simplification could bring an error of 42.8% for liquid and 16.1% for vapour. In this work the model is modified and the term $\frac{\partial p_{EOS}}{\partial T}$ is kept as its original analytical solution. Maxwell construction, D^2 law as well as the three boiling stages are simulated to verify this modified pseudopotential phase change model.

Table 1 Recent pseudopotential LB investigations for boiling heat transfer

Authors	Year	Key words of the study
Zhang and Chen	2003	New force expression, nucleate boiling

Hazi and Markus	2009	Local balance law for entropy, nucleate boiling, bubble departure diameter and frequency
Markus and Hazi	2011	New model, cavity boiling
Biferale et al.	2012	New model, 3D, high Rayleigh number
Gong and Cheng	2013	New model, pool boiling
Li et al.	2015	New hybrid model, boiling curve, wettability
Mu et al.	2017	MRT, cavity shape
Fang et al.	2017	MRT, large density ratio
Zhang and Cheng	2017	Improved Gong-Cheng model, heating conditions
Li et al.	2017	Improved model
Gong and Cheng	2017	Conjugate thermal boundary
Zhang et al.	2018	Temperature-dependent wettability

Table 2 Recent phase-field LB investigations for boiling heat transfer

Authors	Year	Main investigation subjects
Dong et al.	2009	New model, single rising bubble
Tanaka et al.	2011	New model, nucleate boiling, wettability
Sun and Li	2013	3D simulation
Safari et al.	2013	New model for evaporation
Sattari et al.	2014	Nucleate boiling, departure diameter
Begmohammadi et al.	2015	Pool boiling
Begmohammadi et al.	2016	Film boiling, Rayleigh Taylor instability
Sadeghi et al.	2016	3D simulation

4.2 Methodology

It has been reported that the multi-relaxation-time (MRT) model can effectively reduce the spurious currents and increase the numerical stability [129]. The MRT LBM equation can be given as follows:

$$f_\alpha(\mathbf{x}+\mathbf{e}_\alpha\delta_t, t+\delta_t) = f_\alpha(\mathbf{x},t) - (\mathbf{M}^{-1}\mathbf{\Lambda}\mathbf{M})_{\alpha\beta}\left(f_\beta - f_\beta^{eq}\right) + \delta_t F'_\alpha \tag{4-1}$$

where $\mathbf{M}$ is an orthogonal transformation matrix, $\mathbf{\Lambda}$ is a diagonal matrix, and F'_α is the forcing term in D2Q9 scheme.

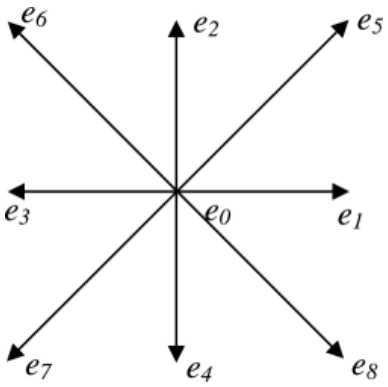

Fig. 4-1 D2Q9 lattice Boltzmann scheme

$\mathbf{e_\alpha}$, $\mathbf{M}$ and $\mathbf{\Lambda}$ can be given as

$$[\mathrm{e}_0, \mathrm{e}_1, \mathrm{e}_2, \mathrm{e}_3, \mathrm{e}_4, \mathrm{e}_5, \mathrm{e}_6, \mathrm{e}_7, \mathrm{e}_8] = \begin{bmatrix} 0 & 1 & 0 & -1 & 0 & 1 & -1 & -1 & 1 \\ 0 & 0 & 1 & 0 & -1 & 1 & 1 & -1 & -1 \end{bmatrix} \tag{4-2}$$

$$\mathbf{M} = \begin{pmatrix} 1 & 1 & 1 & 1 & 1 & 1 & 1 & 1 & 1 \\ -4 & -1 & -1 & -1 & -1 & 2 & 2 & 2 & 2 \\ 4 & -2 & -2 & -2 & -2 & 1 & 1 & 1 & 1 \\ 0 & 1 & 0 & -1 & 0 & 1 & -1 & -1 & 1 \\ 0 & -2 & 0 & 2 & 0 & 1 & -1 & -1 & 1 \\ 0 & 0 & 1 & 0 & -1 & 1 & 1 & -1 & -1 \\ 0 & 0 & -2 & 0 & 2 & 1 & 1 & -1 & -1 \\ 0 & 1 & -1 & 1 & -1 & 0 & 0 & 0 & 0 \\ 0 & 0 & 0 & 0 & 0 & 1 & -1 & 1 & -1 \end{pmatrix} \tag{4-3}$$

$$\Lambda = \mathrm{diag}\left(\tau_\rho^{-1}, \tau_e^{-1}, \tau_\varsigma^{-1}, \tau_j^{-1}, \tau_q^{-1}, \tau_j^{-1}, \tau_q^{-1}, \tau_v^{-1}, \tau_v^{-1}\right) \tag{4-4}$$

The details of relaxation times in Eq. (4-4) can be found in reference [239].

The evolution equation including the streaming step and collision step involving an MRT collision operator can be rewritten as follows:

$$\mathbf{m}^* = \mathbf{m} - \mathbf{\Lambda}(\mathbf{m} - \mathbf{m}^{\mathrm{eq}}) + \delta_t \left(\mathbf{I} - \frac{\mathbf{\Lambda}}{\mathbf{2}}\right)\mathbf{S} \tag{4-5}$$

where $\mathbf{m} = \mathbf{M}\mathbf{f}$, $\mathbf{m}^{eq} = \mathbf{M}\mathbf{f}^{eq}$, and $\mathbf{f}$ and $\mathbf{f}^{eq}$ are the velocity distribution functions and the corresponding equilibrium distribution functions respectively, $\mathbf{I}$ is the unit tenser and $\mathbf{S}$ is the forcing term.

The equilibrium $\mathbf{m}^{eq}$ is given as

$$\mathbf{m}^{eq} = \rho\left(1, -2 + 3|\mathbf{v}|^2, 1 - 3|\mathbf{v}|^2, v_x, -v_x, v_y, -v_y, {v_x}^2 - {v_y}^2, v_x v_y\right) \tag{4-6}$$

where $\mathbf{v} = \left(v_x, v_\mathrm{y}\right)$ is the macroscopic velocity. The macroscopic density and velocity are obtained by

$$\rho = \sum_\alpha f_\alpha \tag{4-7}$$

$$\rho\mathbf{v} = \sum_\alpha \mathbf{e}_\alpha f_\alpha + \frac{\delta_t}{2}\mathbf{F} \tag{4-8}$$

where $\mathbf{F} = \left(F_x, F_y\right)$ is the total force acting on a particle. In this work the interaction force $\mathbf{F_m}$ and the gravity force $\mathbf{F_b}$ are considered. The interaction force is the most important force in the pseudopotential LB model, which can be written by

$$\mathbf{F}_\mathrm{m}(\mathbf{x}, t) = -G\Psi(\mathbf{x}) \sum_\alpha w_\alpha \Psi(\mathbf{x} + \mathbf{e}_\alpha \delta_t)\mathbf{e}_\alpha \tag{4-9}$$

where G is a parameter that determines the strength of the interaction force, w_α are the weights used to calculate the isotropic interaction force. The weights in the D2Q9 scheme is

$$w_\alpha = \left[\frac{4}{3}, \frac{1}{3}, \frac{1}{3}, \frac{1}{3}, \frac{1}{3}, \frac{1}{12}, \frac{1}{12}, \frac{1}{12}, \frac{1}{12}\right] \tag{4-10}$$

The buoyant force is given by

$$\mathbf{F_b} = (\rho - \rho_{ave})\mathbf{g} \tag{4-11}$$

where ρ_{ave} is average density of the computational domain and $\mathbf{g} = (0, -g_0)$ is the gravitational acceleration.

The Peng-Robinson (P-R) non-ideal EOS is used for calculation of the pseudopotential Ψ, which is given by

$$p_{EOS} = \frac{\rho RT}{1-b\rho} - \frac{a\varphi(T)\rho^2}{1+2b\rho-b^2\rho^2} \tag{4-12}$$

where $\varphi(T) = \left[1 + (0.37464 + 1.54226\omega - 0.26992\omega^2)\left(1 - \sqrt{T/T_c}\right)\right]^2$, $a = 0.45724R^2{T_c}^2/p_c$, $b = 0.0778RT_c/p_c$ and the subscript c means critical value. Following the settings in reference [240], $\omega = 0.334$, $a = 3/49$, $b = 2/21$ and $R = 1$.

Moreover, the forcing term in Eq. (4-5) is expressed as

$$\mathbf{S} = \begin{bmatrix} 0 \\ 6\mathbf{v}\cdot\mathbf{F} + \frac{\sigma_0|\mathbf{F_{int}}|^2}{\psi^2\delta_t(\tau_e-0.5)} \\ -6\mathbf{v}\cdot\mathbf{F} - \frac{\sigma|\mathbf{F_{int}}|^2}{\psi^2\delta_t(\tau_\varsigma-0.5)} \\ F_x \\ -F_x \\ F_y \\ -F_y \\ 2\left(v_xF_x - v_yF_y\right) \\ v_xF_y - v_yF_x \end{bmatrix} \tag{4-13}$$

where $\sigma = 1.2$ is applied for the sake of the thermodynamic consistency.

Through Chapman-Enskog [237] analysis, the LB model can cover the macroscopic Navier-Stokes equations:

$$\partial_t\rho + \nabla\cdot(\rho\mathbf{v}) = 0 \tag{4-14}$$

$$\partial_t(\rho\mathbf{v}) + \nabla\cdot(\rho\mathbf{v}\mathbf{v}) = -\nabla\cdot\mathbf{P} + \nabla\cdot\mathbf{\Pi} + \mathbf{F_b} \tag{4-15}$$

where **P** is the pressure tensor and **Π** is the viscous stress tensor. The pressure tensor **P** is given by

$$\mathbf{P} = \left(p_{Eos} + \frac{G^2c^4}{6}\sigma|\nabla\psi|^2 + \frac{Gc^4}{12}\psi\nabla^2\psi\right)\mathbf{I} + \frac{Gc^4}{6}\psi\nabla\nabla\psi \tag{4-16}$$

Next the focus moves on to the thermal model. The entropy equation without considering the viscous heat dissipation can be given by [238]

$$\rho T\frac{Ds}{Dt} = \nabla\cdot(\lambda\nabla T) \tag{4-17}$$

where s is the entropy, and with the thermodynamic relation [235]

$$Tds = c_v dT + T\left(\frac{\partial p_{EOS}}{\partial T}\right)_\rho d\left(\frac{1}{\rho}\right) \tag{4-18}$$

the temperature equation can be obtained

$$\rho c_v \frac{DT}{Dt} = \nabla \cdot (\lambda \nabla T) - T\left(\frac{\partial p_{Eos}}{\partial T}\right)_\rho \nabla \cdot \mathbf{v} \tag{4-19}$$

where λ is the heat conductivity, c_v is the specific heat at constant volume.

As mentioned above, the source term of the thermal LB equation can bring about computational errors, thus in this work the energy equation is solved directly using the classical fourth-order Runge-Kutta scheme [241], and the energy equation is equivalent to

$$\partial_t T = -\mathbf{v} \cdot \nabla T + \frac{1}{\rho c_v} \nabla \cdot (\lambda \nabla T) - \frac{T}{\rho c_v}\left(\frac{\partial p_{EOS}}{\partial T}\right)_\rho \nabla \cdot \mathbf{v} \tag{4-20}$$

The classical fourth-order Runge-Kutta scheme can be given by

$$T^{t+\delta t} = T^t + \frac{\delta t}{6}(h_1 + 2h_2 + 2h_3 + h_4) \tag{4-21}$$

where

$$h_1 = K(T^t) \tag{4-22}$$

$$h_2 = K\left(T^t + \frac{\delta t}{2} h_1\right) \tag{4-23}$$

$$h_3 = K\left(T^t + \frac{\delta t}{2} h_2\right) \tag{4-24}$$

$$h_4 = K(T^t + \delta t h_3) \tag{4-25}$$

and $K(T)$ denotes the right-hand side of Eq.(4-21) (4-20).

The term $\frac{\partial p_{EOS}}{\partial T}$ in Eq. (4-20) is simplified as $\frac{\rho R}{1-b\rho}$, however, it is found in this work that such simplification could bring an error of 42.8% for liquid and 16.1% for vapour.

Therefore, the original time derivative of Eq. (4-12) without any simplification is adopted in this work.

4.3 Validation of the numerical model

4.3.1 Liquid-vapour coexistent densities

In thermodynamic equilibrium, one basic consistency is that pressure cannot increase with volume, however, this is always violated in analytic models for ideal gases, for example, in the Peng-Robinson equation of state used in the thermal LB model as shown in Fig. 4-2. Then the Maxwell construction was utilized to correct this deficiency [242]. Fig. 4-2 gives the Maxwell construction for a steady droplet (diameter 60) with vapour surrounded in a 20×20 computational domain at saturated temperature $T_s = 0.86T_c$. Following the work from Li et al. [240], the kinematic viscosities for liquid and vapour two phases are set as $\nu_L = 0.1$ and $\nu_V = \frac{0.5}{3}$, the specific heat is taken as a constant $c_v = 6$, and the conductivity is $\lambda = \rho c_v \chi$ with $c_v \chi = 0.028$. All the parameters are given in the lattice unit. With the definition of the relations between lattice units and the physical units, lattice mass $\mathrm{M} = 4.1 \times 10^{-10}\mathrm{kg}$, lattice length $\mathrm{L} = 1.675 \times 10^{-6}\mathrm{m}$ and lattice time $\mathrm{T_t} = 2.264 \times 10^{-6}\mathrm{s}$, the physical values can be obtained as $\rho_L = 950\mathrm{kg/m^3}$, $\nu_L = 1.239 \times 10^{-7}\mathrm{m^2/s}$. All the other physical values can also be obtained via simple calculations. In Fig. 4-2, the curve for ideal equation of state and the straight line for Maxwell construction enclose two regions which have the same area $A1 = A2$, and the two intersections in the left side and in the right side correspond to the coexistent liquid density and vapour density respectively under the same pressure. The asterisks are the coexistent liquid-vapour densities obtained by simulation. The results show that the simulation agrees well with

the theoretical analysis for liquid-vapour coexistent densities and the coexistent densities are about $\rho_L \approx 6.50$ and $\rho_V \approx 0.38$, respectively.

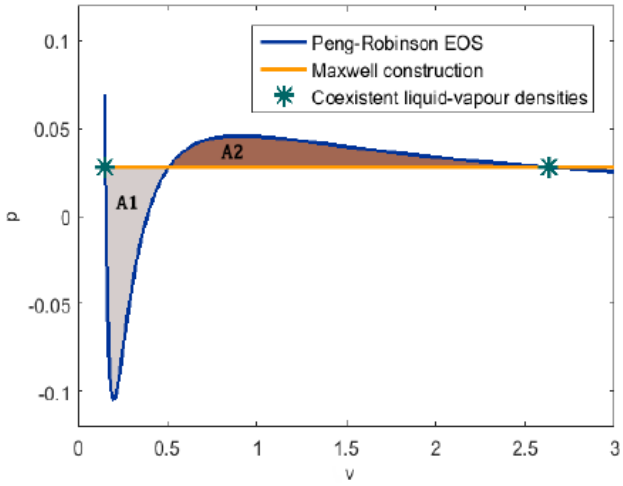

Fig. 4-2 Liquid-vapour coexistent densities and Maxwell construction at $T_s = 0.86T_c$.

The Maxwell construction in Fig. 4-2 can also explain the mechanism of phase change in this pseudopotential LB model. In this model, the pseudopotential force in Eq. (4-9) is the key factor that causes the phase segregation, and the non-ideal equation of state in Eq. (4-12) determines the phase change – while temperature changes, the $p - v$ diagram and the density distribution (including coexistence densities) in Fig. 4-2 change as well, so the phase change can be realized. Therefore, from the mechanism of phase change in pseudopotential LB model it can be seen that there is no apparent difference between evaporation and boiling, and the difference is the phase change speed which is caused by the temperature difference.

4.3.2 D^2 law for droplet evaporation

D^2 law is a well-known principle for droplet evaporation and combustion, which describes that the change of droplet squared diameter over time is linear [243]. The droplet evaporation is implemented in this section for numerical model validation via the D^2 law. The simulation setting is almost the same as those in the previous section,

except that the saturated temperature $T_s = 0.86T_c$ is given to the droplet but a higher temperature $T_v = T_s + 0.0137$ is loaded on the vapour region and the boundaries are kept at the temperature T_v. In addition, for D^2 law the thermalphysical parameters should be constant thus thermal conductivity is chosen to be constant with $\lambda = 2/3$.

Fig. 4-3 gives the transient droplet states with initial diameter $D_0 = 80$ during the evaporation process. It can be clearly seen the diameter of the droplet decreases over time, and the vapour concentration increases around the droplet. The simulated variations of $\left(\frac{D}{D_0}\right)^2$ with respect to time for droplets with different initial diameters are shown in Fig. 4-4 (a). It can be concluded from the figure that after a short period of initial time, the squares of diameter vary linearly over time, which is consistent with the D^2 law. As for the droplet squared diameter variation nonlinear part in the initial time of the simulation, the result is still normal and the phenomenon has been presented in previous experiment study as shown in Fig. 4-4 (b) from Nishiwaki [39].

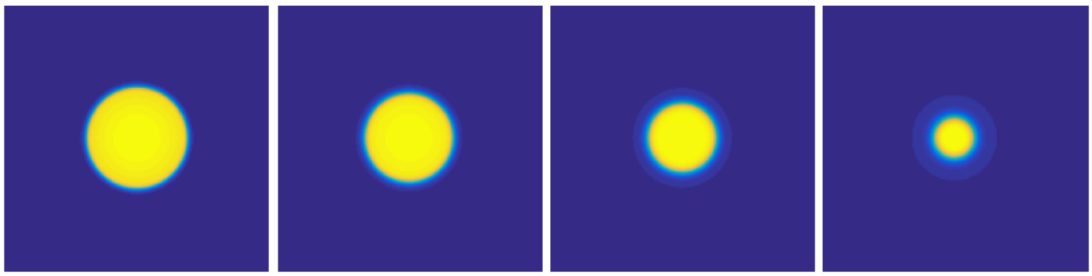

Fig. 4-3 Snapshots of droplet evaporation for $D_0 = 80$ at (a) $t = 10{,}000$ (b) $t = 60{,}000$ (c) $t = 110{,}000$ (d) $t = 16{,}000$.

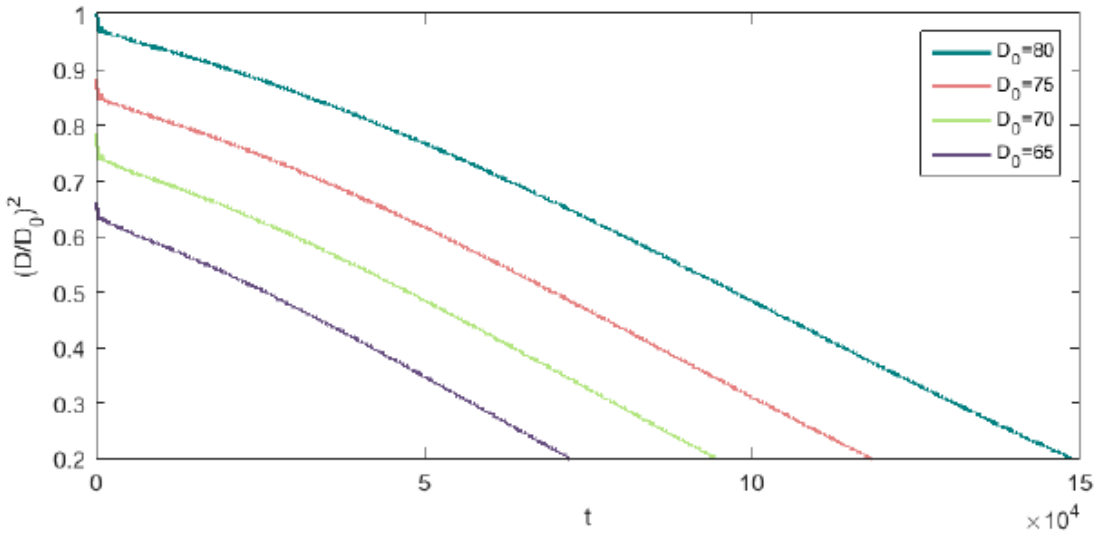

(a)

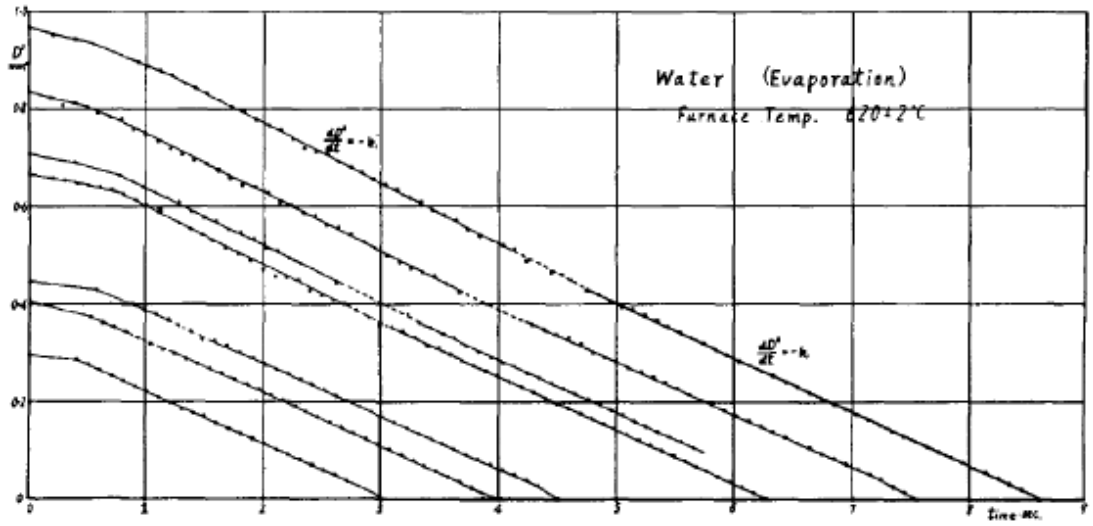

(b)

Fig. 4-4 (a) Simulation of droplets evaporation with different initial diameters (b) Experimental data from Nishiwaki [39], with permission from Elsevier, Copyright 1955.

4.3.3 Three boiling stages

It is well known that there are three distinct boiling stages for pool boiling, i.e. nucleate boiling, transition boiling and film boiling [244]. Study of the three boiling stages is of great significance. Nucleate boiling has been recognized as one of the most effective heat transfer approaches and the critical heat flux for nucleate boiling has long been concerned for heat transfer enhancement. In this work, modelling of the three boiling

stages is accomplished using the modified liquid-vapour phase change thermal LB model by controlling the temperature of heating surface. The computational domain is set as 400×180 with upper half domain for vapour and lower half domain for liquid as initial conditions. The top and bottom boundaries are set as non-slip solid, and periodical boundaries are applied in the x direction. The saturated temperature $T_s = 0.86T_c$ is adopted to all the computational domain except that a higher temperature with superheat ΔT is applied to the bottom solid boundary to heat the saturated liquid. The equilibrium contact angle for a droplet on the solid surface is approximately $44.5°$. Differing from the previous settings, the buoyancy force is considered in this part and the gravity acceleration is taken as $g = 3 \times 10^{-5}$.

Fig. 4-5 - Fig. 4-7 display the nucleate boiling, transition boiling and film boiling respectively. Fig. 4-8 shows the corresponding transient heat fluxes for the three boiling stages calculated by $q(t) = \int_0^{L_x} q_w(x)dx/L_x$ where L_x is the length in x direction and $q_w(x) = -\lambda\left(\frac{\partial T}{\partial y}\right)|_{y=0}$. All the displayed pictures are after 20,000 time steps once the boiling stages are steady. And for transition boiling and film boiling, the superheat values are enhanced on the basis of a steady nucleate boiling stage. The nucleate boiling is simulated under the superheat $\Delta T = 0.0137$. It can be seen that owing to the heating loaded on the bottom solid surface, some nucleation sites are formed. Following that the vapour bubbles are formed, grow, coalesce with each other, depart from the heating surface, rise and break at the liquid-vapour interface. Whilst during the whole process the nucleation sites are clearly separated. The transient heat flux in Fig. 4-8 for this boiling stage is relatively steady and high. However, when the superheat is increased to $\Delta T = 0.02$, the phase change on the heating surface is more complex as many nucleation sites merge into larger vapour films and there are no

apparent individual nucleation sites as shown in Fig. 4-6, and also its transient heat flux becomes unsteady. Finally, the superheat $\Delta T = 0.025$ is loaded on the heating surface and when it runs to steady the whole heating solid surface is covered by a large portion of continuous vapour film. The only heat transfer between the heating solid surface and the bulk liquid are conduction and convection in the vapour phase, which leads to a relatively low heat transfer compared to the other two boiling stages as shown in Fig. 4-8.

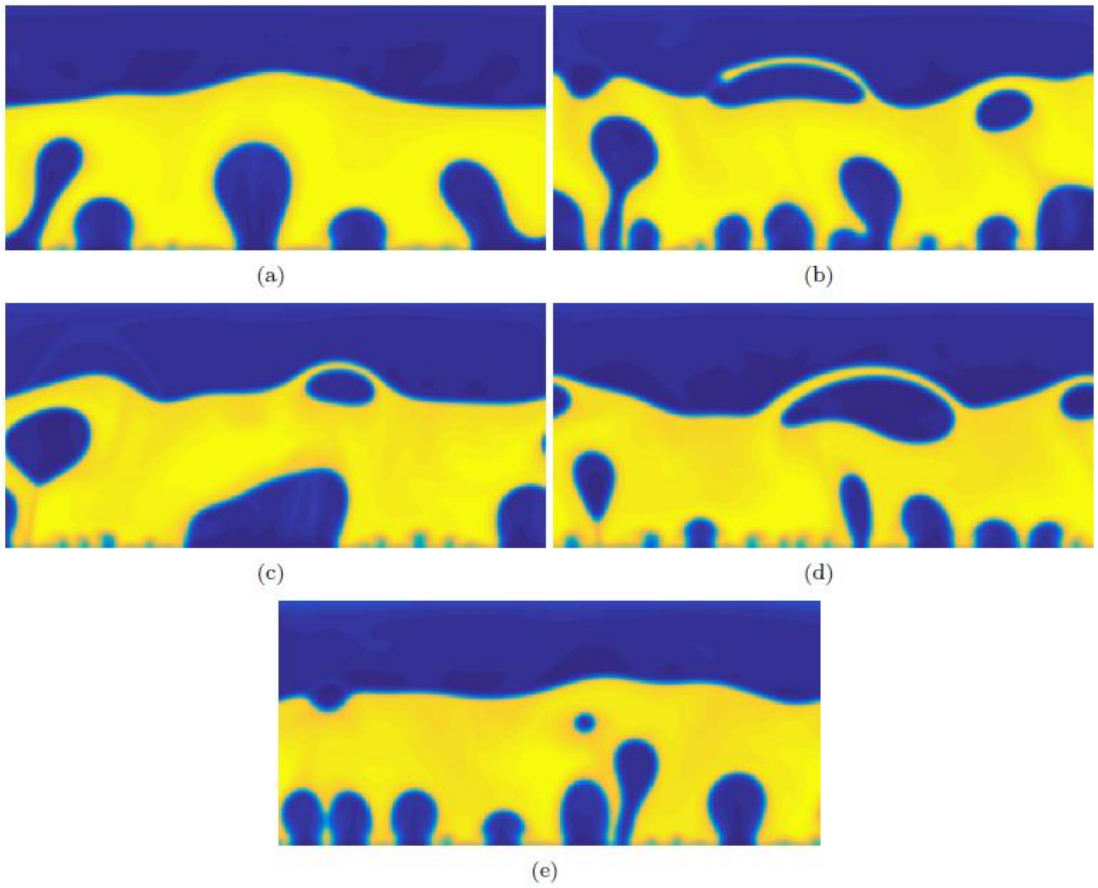

Fig. 4-5 Snapshots of nucleate boiling at $\Delta T = 0.0137$ (a) $t = 20{,}000$ (b) $t = 25{,}000$ (c) $t = 30{,}000$ (d) $t = 35{,}000$ (e) $t = 40{,}000$.

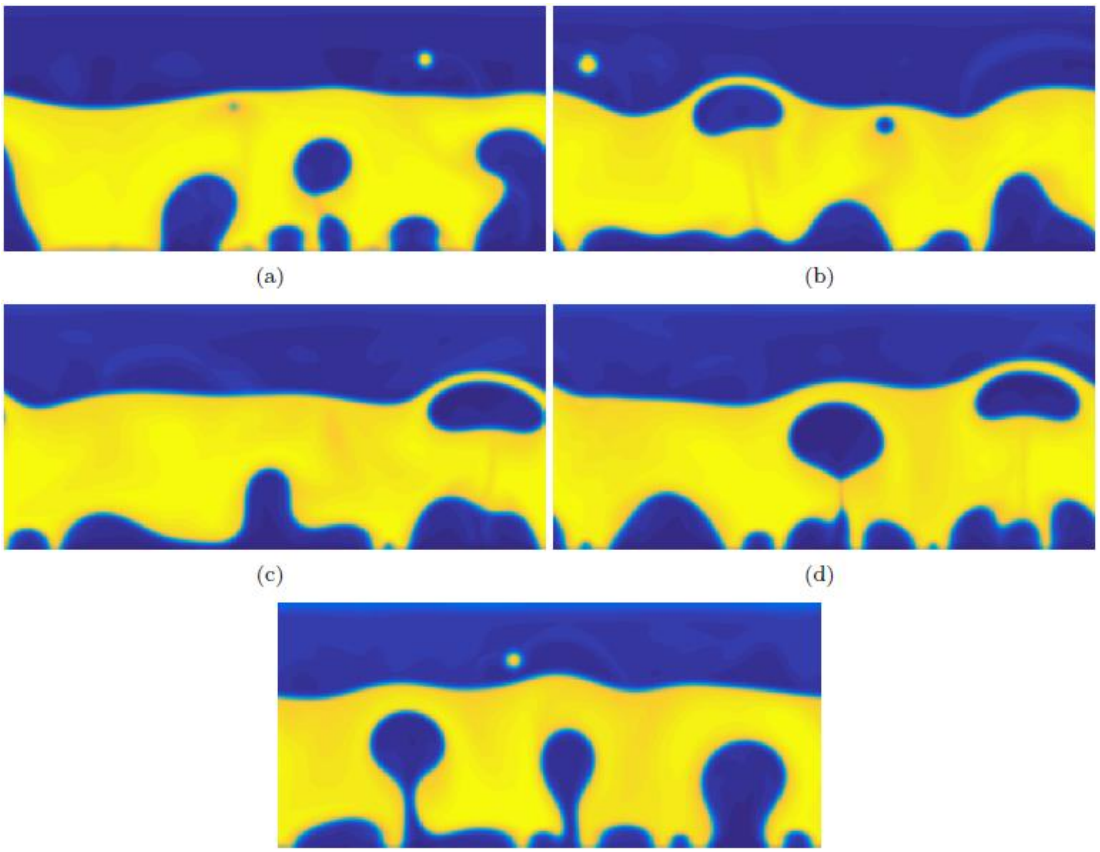

Fig. 4-6 Snapshots of transition boiling at $\Delta T = 0.02$ (a) $t = 20{,}000$ (b) $t = 25{,}000$ (c) $t = 30{,}000$ (d) $t = 35{,}000$ (e) $t = 40{,}000$.

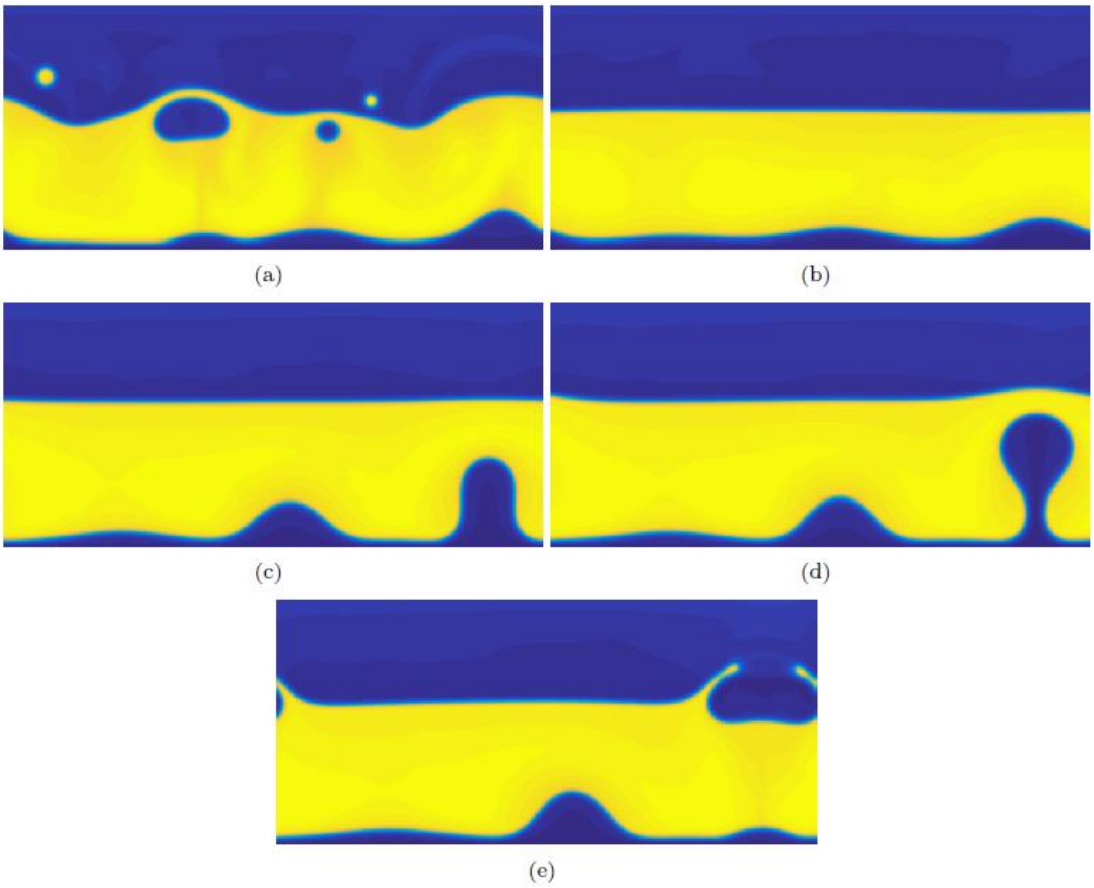

Fig. 4-7 Snapshots of film boiling at $\Delta T = 0.025$ (a) $t = 25{,}000$ (b) $t = 50{,}000$ (c) $t = 70{,}000$ (d) $t = 72{,}500$ (e) $t = 75{,}000$.

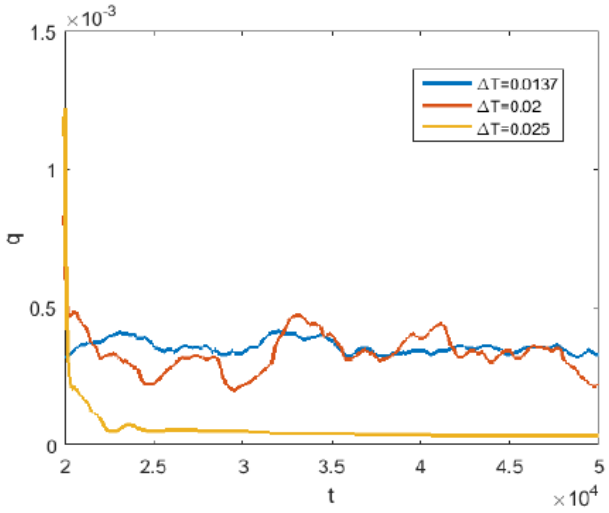

Fig. 4-8 Transient heat fluxes with different superheat conditions.

4.4 Summary

In this work a phase change LB model is modified for simulation of boiling heat transfer. The multiphase model is validated by Maxwell construction for liquid-vapour coexistent densities at the saturated temperature. Then the droplet evaporation process is simulated and the D^2 law is considered. The droplets are in different initial diameters, and the squares of diameter vary linearly over time, which is also in good agreement with experimental results from the previously published paper. Finally, the three boiling stages, i.e. nucleate boiling, transition boiling and film boiling are accomplished with different superheat values acting on the bottom solid heating surface using the present model. The transient heat fluxes are given to show the heat transfer features for the three boiling stages.

Chapter 5: Investigation of Multi-bubble/droplet Coexistence Problem for SCMP Pseudopotential LBM

5.1 Introduction

In the past few decades, the lattice Boltzmann method (LBM) has been developed significantly due to its remarkable advantages compared with conventional CFD methods in mesoscale [212, 221]. Meanwhile it has been applied to a broad range of application areas [113, 245-250], such as single/multi-phase flows, phase change, rarefied gas flows, etc. Among all the members of the LBM community including the colour-gradient LBM [129], the pseudopotential LBM [247], the free-energy LBM [132] and the phase-field LBM [134, 185], the pseudopotential model has shown striking superiority in multiphase flows due to its simplicity, versatility and the distinctive feature that different phases can be segregated automatically on account of the particle interactions. Besides, in comparison with the free-energy and the colour-gradient LBM, the pseudopotential LBM has much better performance in dynamic multiphase flows at large density ratios and relatively high Reynolds numbers [113].

The pseudopotential LBM was firstly introduced by Shan and Chen [130, 131], and the most distinctive feature of this model is the interparticle potential Ψ which is based on the local density. With the pseudopotential treatment, the particles having the same densities can be attracted together, thus causing the phase segregation automatically without any special treatment of interface tracking or capturing techniques. The original definition of the pseudopotential proposed by Shan and Chen is

$$\psi = \rho_0 \left(1 - e^{-\frac{\rho}{\rho_0}}\right) \tag{5-1}$$

where ρ denotes density and ρ_0 is a constant. The interaction force at the position $\mathbf{x}$ and time t acting on a partible from the other surrounding particles for single-component multiphase (SCMP) models can be expressed as

$$\mathbf{F}_{\text{int}}(\mathbf{x}, t) = -G\psi(\mathbf{x}) \sum_\alpha w_\alpha \psi(\mathbf{x} + \mathbf{e}_\alpha \delta_t)\mathbf{e}_\alpha \tag{5-2}$$

where G is a parameter that determines the strength of the interaction force, w_α are the weights used to calculate the isotropic interaction force, and $\mathbf{e}_\alpha$ and δ_t are the discrete lattice velocities and time step, respectively. With Taylor expansion to the interaction force Eq. (5-2), the following non-ideal equation of state (EOS) can be obtained [247]

$$p = \rho {c_s}^2 + \frac{G {c_s}^2}{2} \psi^2 \tag{5-3}$$

with which other EOSs such as van der Waals (vdW) EOS [251], Carnahan-Starling (C-S) EOS [252] and Peng-Robinson (P-R) EOS [253] can be incorporated into the pseudopotential model by replacing the potential Eq. (5-1) with the following definition [254]

$$\psi = \sqrt{\frac{2(p - \rho {c_s}^2)}{G {c_s}^2}} \tag{5-4}$$

Incorporating the realistic EOSs into the pseudopotential LBM is an important and effective way to increase the density ratio of simulation, which has always been a big issue restricting the application of LBM for real multiphase flows.

In recent years, advances for development of the pseudopotential LBM have been focusing on the spurious current [254], thermodynamic inconsistency [255], limited

density and viscosity ratios [256] by adjusting the equation of state (EOS) [253], interaction force term [257] and force scheme [258]. Meanwhile, applications of pseudopotential LBM can be found in a wide range of areas such as boiling heat transfer [259], condensation [223], droplet motions [260], etc. Some excellent latest review works regarding pseudopotential LBM can be found in references [113, 247, 261].

The aim of this work is focusing on the unphysical mass transfer problem of SCMP models, discussing the possible reason and possible way to resolve this problem.

5.2 Problem description

The study shows that the multiple bubbles/droplets cannot coexist stably using the normal SCMP models [228], where only the attractive forces between particles are considered which drive the phase segregation. The reason for the unachievable multi-bubble/droplet system is the unphysical mass transfer which we call “the big eat the small” - the smaller bubbles/droplets shrink and eventually disappear over time while the bigger ones get bigger before a physical coalescence. Chibbaro et al. [257] presented a new model with midrange repulsion forces introduced into the interaction forces by involving the second nearest-neighbouring particles. This repulsive force mimics the impurities on the liquid/vapour interface that prevents the coalescence of contacted droplets/bubbles to achieve multi-bubble/droplet coexistence as shown in Fig. 5-1. However, after testing their model, it is found that the unphysical phenomenon of “the big eat the small” still cannot be eliminated. As shown in Fig. 5-1 (b) and Fig. 5-1 (c), it can be seen that the smaller bubbles still get smaller over time. The reason that there are more small droplets left in Fig. 5-1 (a) than bubbles in Fig.

5-1 (c) at the same time level is that the unphysical phenomenon of mass transfer is much less severe for multi-droplet configurations than the multi-bubble configurations.

(a) (b) (c)

Fig. 5-1 Multi-bubble/droplet configurations in 512×512 computational domains with periodical boundary conditions using the midrange repulsion model, $\rho_l \approx 1.87$, $\rho_v \approx 0.18$, and $\upsilon_l = \upsilon_v = 0.5/3$. (a) multi-droplet system at $t = 20{,}000\delta_t$, $G_1 = -15$, $G_2 = 10.1$ (b) multi-bubble system at $t = 15{,}000\delta_t$, $G_1 = -20$, $G_2 = 15.1$ (c) multi-bubble system at $t = 20{,}000\delta_t$, $G_1 = -20$, $G_2 = 15.1$

Besides the use of SCMP models, multi-component multiphase (MCMP) models are also widely applied, and the interaction force for this model can be written as [130]

$$\mathbf{F}_{\mathrm{int},i}(\mathbf{x},t) = -\psi_i(\mathbf{x}) \sum_{\bar{\imath}} G_{i\bar{\imath}} \sum_{\alpha} w_\alpha \, \psi_{\bar{\imath}}(\mathbf{x} + \mathbf{e}_\alpha \delta_t) \mathbf{e}_\alpha \tag{5-5}$$

where i and $\bar{\imath}$ denote the corresponding components. Using MCMP models to study multiphase flows involving multi-bubble/droplet systems is more popular than SCMP models, and such studies can be found in reference [262-268]. However, the MCMP always suffers the limitation of increasing the density ratio and kinematic viscosity ratio [247], which restricts its application to a large extent.

This work pointed out the problem of "the big eat the small" in SCMP model for the first time and its behaviours in thermal multiphase flow was presented, where it is found by coupling an entropy-based energy equation the unphysical mass transfer can be effectively restrained. In this work, the features of the unphysical mass transfer phenomenon are studied in detail and the possible reason from the viewpoint of algorithm is discussed, to have a better understanding of this problem and lay the foundation for completely sorting it out in further studies.

5.3 Features of the problem

5.3.1 The pseudopotential lattice Boltzmann model

The original Shan-Chen model [130], an improved Bhatnagar-Gross-Krook (BGK) model in 3D with the given code in reference [261], the Gong-Cheng model [269], the midrange repulsion model [257] and the Li Q. improved multiple-relaxation-time (MRT) model [270] are all tested in this study. These models contain the typical non-ideal EOSs, forcing schemes, and collision operators of SCMP pseudopotential LBM. After testing these models, it is found that none of them can get rid of the unphysical mass transfer. In this work the Li Q. model [270] is used to present the study of the unphysical mass transfer features.

An improved forcing scheme has been adopted in this model to adjust the mechanical stability condition so that the thermodynamic inconsistency can be eliminated. The MRT LBM equation can be given as

$$f_\alpha(\mathbf{x}+\mathbf{e}_\alpha\delta_t, t+\delta_t) = f_\alpha(\mathbf{x},t) - (\mathbf{M}^{-1}\mathbf{\Lambda}\mathbf{M})_{\alpha\beta}\left(f_\beta - f_\beta^{eq}\right) + \delta_t F'_\alpha \tag{5-6}$$

$\mathbf{e}_\alpha$, $\mathbf{M}$ and $\mathbf{\Lambda}$ in the D2Q9 scheme can be given as

$$[\mathrm{e}_0, \mathrm{e}_1, \mathrm{e}_2, \mathrm{e}_3, \mathrm{e}_4, \mathrm{e}_5, \mathrm{e}_6, \mathrm{e}_7, \mathrm{e}_8] = \begin{bmatrix} 0 & 1 & 0 & -1 & 0 & 1 & -1 & -1 & 1 \\ 0 & 0 & 1 & 0 & -1 & 1 & 1 & -1 & -1 \end{bmatrix} \tag{5-7}$$

$$\mathbf{M} = \begin{pmatrix} 1 & 1 & 1 & 1 & 1 & 1 & 1 & 1 & 1 \\ -4 & -1 & -1 & -1 & -1 & 2 & 2 & 2 & 2 \\ 4 & -2 & -2 & -2 & -2 & 1 & 1 & 1 & 1 \\ 0 & 1 & 0 & -1 & 0 & 1 & -1 & -1 & 1 \\ 0 & -2 & 0 & 2 & 0 & 1 & -1 & -1 & 1 \\ 0 & 0 & 1 & 0 & -1 & 1 & 1 & -1 & -1 \\ 0 & 0 & -2 & 0 & 2 & 1 & 1 & -1 & -1 \\ 0 & 1 & -1 & 1 & -1 & 0 & 0 & 0 & 0 \\ 0 & 0 & 0 & 0 & 0 & 1 & -1 & 1 & -1 \end{pmatrix} \tag{5-8}$$

$$\mathbf{\Lambda} = \mathrm{diag}\left(\tau_\rho^{-1}, \tau_e^{-1}, \tau_\varsigma^{-1}, \tau_j^{-1}, \tau_q^{-1}, \tau_j^{-1}, \tau_q^{-1}, \tau_\nu^{-1}, \tau_\nu^{-1}\right) \tag{5-9}$$

The details of relaxation times in Eq. (5-9) can be found in reference [239].

The evolution equation including the streaming step and collision step involving an MRT collision operator can be rewritten as follows:

$$\mathbf{m}^* = \mathbf{m} - \mathbf{\Lambda}(\mathbf{m} - \mathbf{m}^{eq}) + \delta_t \left(\mathbf{I} - \frac{\mathbf{\Lambda}}{2}\right)\mathbf{S} \tag{5-10}$$

where $\mathbf{m} = \mathbf{M}\mathbf{f}$, $\mathbf{m}^{eq} = \mathbf{M}\mathbf{f}^{eq}$, and $\mathbf{f}$ and $\mathbf{f}^{eq}$ are the velocity distribution functions and the corresponding equilibrium distribution functions respectively, $\mathbf{I}$ is the unit tenser and $\mathbf{S}$ is the forcing term.

The equilibrium $\mathbf{m}^{eq}$ is given as

$$\mathbf{m}^{eq} = \rho\left(1, -2 + 3|\mathbf{v}|^2, 1 - 3|\mathbf{v}|^2, v_x, -v_x, v_y, -v_y, {v_x}^2 - {v_y}^2, v_x v_y\right) \tag{5-11}$$

where $\mathbf{v} = \left(v_x, v_\mathrm{y}\right)$ is the macroscopic velocity. The macroscopic density and velocity are obtained by

$$\rho = \sum_\alpha f_\alpha \tag{5-12}$$

$$\rho\mathbf{v} = \sum_\alpha \mathbf{e}_\alpha f_\alpha + \frac{\delta_t}{2}\mathbf{F} \tag{5-13}$$

where $\mathbf{F} = \left(F_x, F_y\right)$ is the total force acting on a particle.

The weights in the D2Q9 scheme in Eq. (5-2) is

$$w_\alpha = \left[\frac{4}{3}, \frac{1}{3}, \frac{1}{3}, \frac{1}{3}, \frac{1}{3}, \frac{1}{12}, \frac{1}{12}, \frac{1}{12}, \frac{1}{12}\right] \tag{5-14}$$

The forcing term in Eq. (5-10) is expressed as

$$\mathbf{S} = \begin{bmatrix} 0 \\ 6\mathbf{v}\cdot\mathbf{F} + \frac{\sigma_0|\mathbf{F}_{\mathrm{int}}|^2}{\psi^2\delta_t(\tau_e - 0.5)} \\ -6\mathbf{v}\cdot\mathbf{F} - \frac{\sigma|\mathbf{F}_{\mathrm{int}}|^2}{\psi^2\delta_t(\tau_\varsigma - 0.5)} \\ F_x \\ -F_x \\ F_y \\ -F_y \\ 2\left(v_x F_x - v_y F_y\right) \\ v_x F_y - v_y F_x \end{bmatrix} \tag{5-15}$$

No external forces but the interaction force $\mathbf{F}_{\mathrm{int}}$ is considered in this study, which can be calculated by Eq. (5-2) and Eq. (5-4), thus there is $\mathbf{F} = \mathbf{F}_{\mathrm{int}}$. $\sigma_0 = 1.2$ is applied in this work for the sake of the thermodynamic consistency.

With the realistic non-ideal EOS applied in the SCMP model, this model is verified by comparing the simulation result with the Maxwell construction

$$\int_{V_{m,l}}^{V_{m,v}} p_{EOS}\, dV_m = p_0\left(V_{m,v} - V_{m,l}\right) \tag{5-16}$$

where V_m is the molar volume, and the subscript v and l denote vapour and liquid respectively. When the saturation temperature $T_s = 0.86T_c$, the liquid and vapour densities are $\rho_l \approx 0.65$ and $\rho_v \approx 0.38$ in the two-phase system, which correspond to the coexistence densities calculated by Eq. (5-16). Other fluids properties are set as follows. The kinematic viscosities for liquid and vapour phases are $\nu_l = 0.1$ and $\nu_v = 0.5/3$. The specific heat is taken as constant $c_v = 6$. The thermal conductivity is $\lambda_f =$

$\rho c_v \chi$ with $c_v \chi = 0.028$. For the MCMP simulation, the original Shan-Chen model is applied with $\rho_l \approx 2.01$, $\rho_v \approx 0.02$, and $\nu_l = \nu_v = 0.5/3$, where no non-ideal EOS is considered, therefore the model is verified with the Laplace Law

$$\Delta p = \frac{2\sigma}{r_c} \tag{5-17}$$

where σ is the surface tension and r_c is the radius of curvature. The verification can be seen in Fig. 5-2.

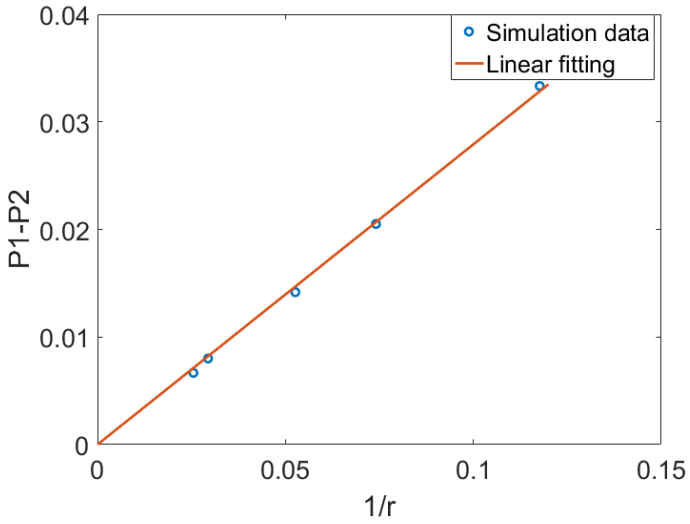

Fig. 5-2 Verification of Laplace Law for the MCMP model

5.3.2 Results and discussion

Why the unphysical mass transfer just occurs in multi-bubble/droplet systems as the process of "the big eat the small"? Is there "the small eat the big"? In this part a specific two-phase system as shown in Fig. 5-3 is tested in a 100×150 computational area. The top and bottom boundaries are solid walls and the left and right boundaries are periodical. The initial states are shown in Fig. 5-3 (a) and Fig. 5-3 (e), where the initial radium of the bubble/droplet is 40, the height of the bottom vapour/liquid region is 10, and no initial velocity is loaded. In such an initial state, either the volume or the area of the liquid/vapour interface of the bottom vapour/liquid region is smaller than that

of the bubble/droplet. However, this time it is the small that "eat" the big, rather than the normal phenomenon "the big eat the small". Therefore, adding the unphysical problem in the regular bubble/droplet systems it can be concluded that it is the bubbles/droplets having bigger interface curvature radii that absorb the ones with smaller interface curvature radii, rather than the volume of the bubble/droplet or the area of the interfaces.

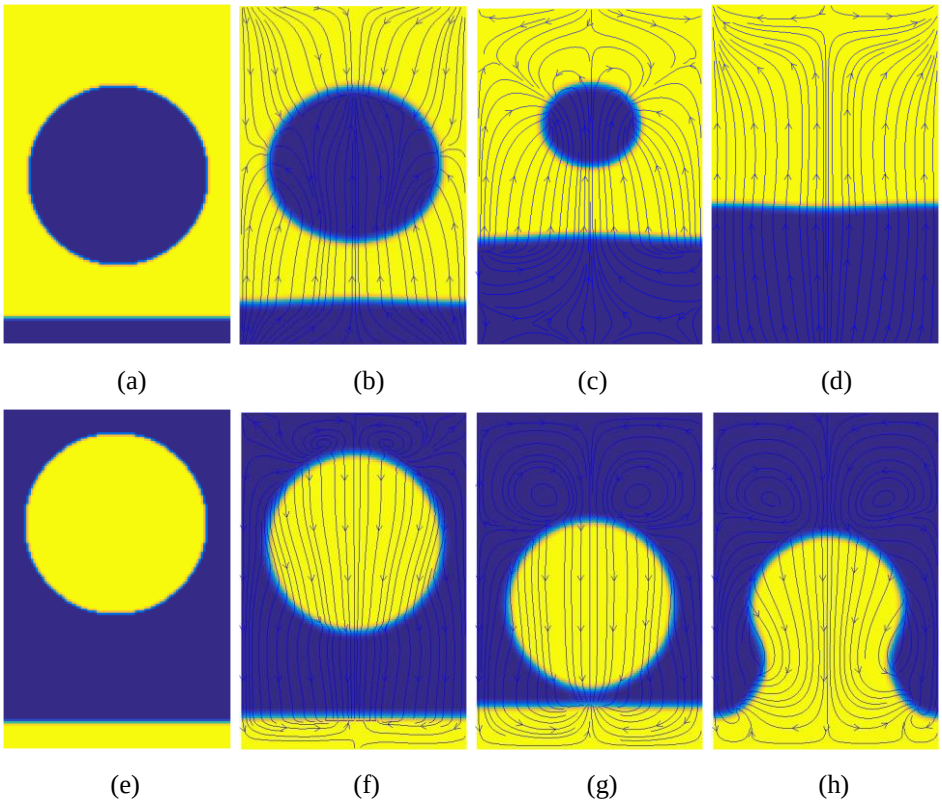

Fig. 5-3 The small vapour/liquid region "eats" the big bubble/droplet (a) bubble system, $t = 0$ (b) bubble system, $t = 1{,}100\delta_t$ (c) bubble system, $t = 2{,}500\delta_t$ (d) bubble system, $t = 3{,}700\delta_t$ (e) droplet system, $t = 0$ (f) droplet system, $t = 4{,}200\delta_t$ (g) droplet system, $t = 9{,}400\delta_t$ (h) droplet system, $t = 10{,}200\delta_t$

From Fig. 5-4 it can be also seen that spurious flow fields are generated between bubbles/droplets. Moreover, the direction of the spurious flow field is exactly the direction of the high-density mass transfer, which means the unphysical mass transfer phenomenon is the transfer of high-density mass. Besides in the normal SCMP pseudopotential LBM only attractive interaction force is considered, and this

interaction force only acts on the area where there is potential gradient, and the interaction force has the same direction as the potential gradient, which can be concluded from Eq. (5-2). Normally the high-density particles have high pseudopotentials, thus it can be in a manner of speaking that the essence of the normal SCMP pseudopotential LBM is the mutual attraction of high-density particles. Adding that the unphysical transfer is related to the curvatures of the two-phase interfaces, and the magnitude of the interaction forces are apparently concerned with the interface curvature – smaller curvature generates larger interaction force, it is most likely that the reason for the unphysical mass transfer is the essential attractive interaction force. To confirm this viewpoint about the reason for the unphysical mass transfer, another example is given in Fig. 5-4, where an annular liquid film is initially placed in a static state. It can be seen that eventually the annular liquid film is agglomerated to a sphere liquid droplet, which is more evident to suggest the high-density mass moving driven by the attraction force.

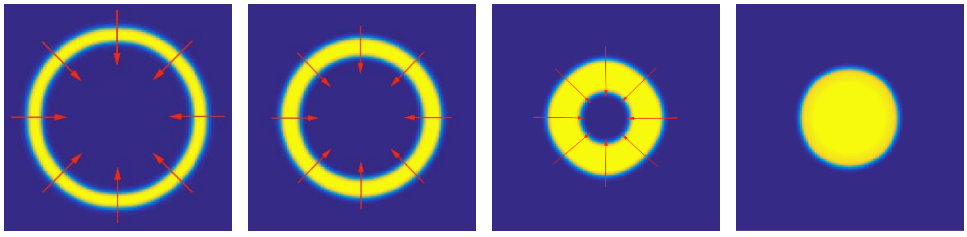

(a) (b) (c) (d)

Fig. 5-4 The evolution of an annular liquid film (a) $t = 41\delta_t$ (b) $t = 521\delta_t$ (c) $t = 1{,}001\delta_t$ (d) $t = 1{,}361\delta_t$

Fig. 5-5 presents the evolution of multi-bubble/droplet system using MCMP model, and there is no unphysical mass transfer observed over time. Fig. 5-6 gives the comparison of densities and spurious currents of the two different components. From Fig. 5-6 (c) and Fig. 5-6 (d), it can be seen that the spurious currents point to opposite directions due to the density distributions of the two components. Apparently, the

spurious currents in this model are mainly caused by the attractive interaction forces, and the attractive forces of the two components pointopposite ways, thus any unphysical effect owing to the attractive interaction force can be counteracted, which should be the reason why there is no such unphysical mass transfer in MCMP LBM.

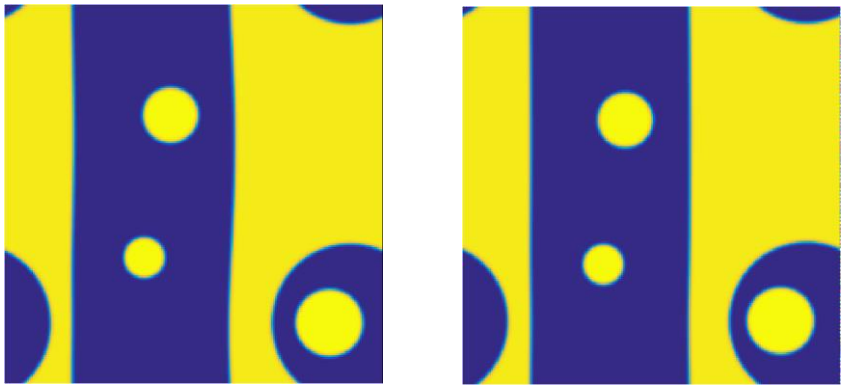

(a) (b)

Fig. 5-5 Multi-bubble/droplet system evolution using MCMP model in a 200×200 area (a) $t = 15{,}000\delta_t$ (b) $t = 20{,}000\delta_t$

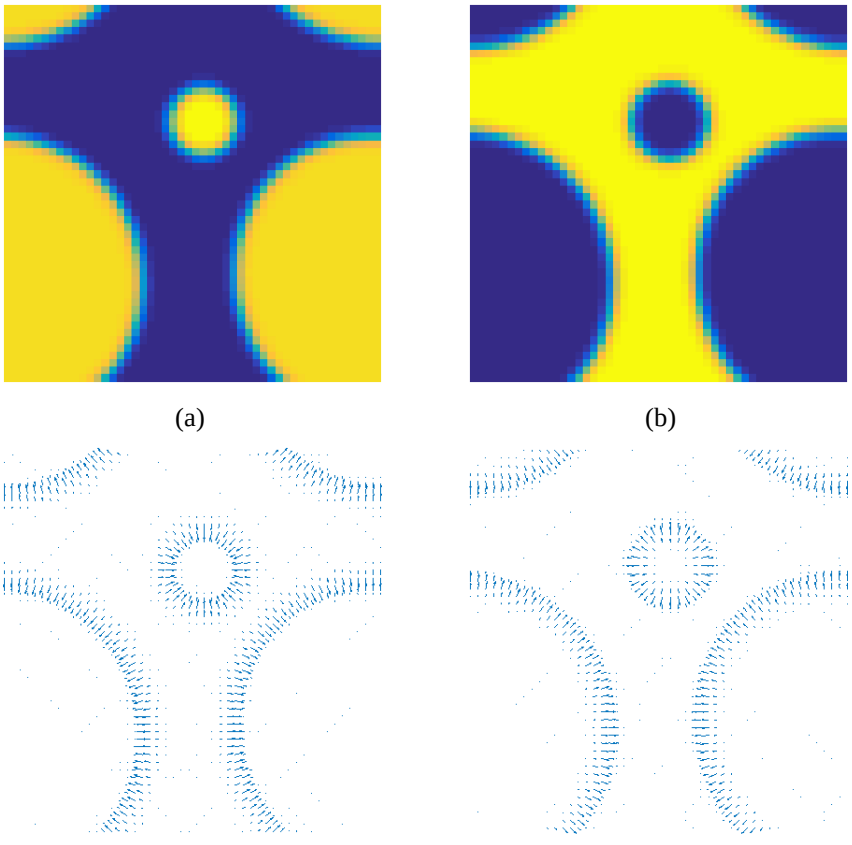

(a) (b)

(c) (d)

Fig. 5-6 Comparison of the two components of MCMP model in a 50×50 area at $t = 2{,}000\delta_t$

Interestingly, for multi-droplet the unphysical mass transfer seems to be similar to the Ostwald ripening, which has been observed in solid solutions or liquid sols describing the change of an inhomogeneous structure over time that, small crystals or sol particles dissolve and redeposit onto larger crystals or sol particles [271]. The reason for Ostwald ripening is that larger particles are more energetically favoured than smaller particles, because molecules on the surface of a particle are energetically less stable than the ones in the interior and smaller particles have larger specific area [272]. Therefore, Ostwald ripening is related to the free energy at the level of molecular scale and particles motion. However, in pseudopotential model the so called "particle" is density distribution function, not real particles and the mechanism for multi-phase flow are gas kinetic theory Boltzmann equation and fluid mechanics Navior-Stokes equations. That is also the reason that we call the problem "unphysical", because in the general immiscible two-phase systems which can be described by Navior-Stokes equation there should not be such phenomenon.

5.4 Thermal equation effect

Another major finding in this study is that the selection of a proper energy equation for thermal LB models can be advantageous for multi-bubble/droplet systems as well. For thermal LB models, without considering the viscous heat dissipation and the compression work, the internal energy equation is given by [113]

$$\partial_t(\rho c_v T) + \nabla \cdot (\rho c_v T \mathbf{v}) = \nabla \cdot \left(\lambda_f \nabla T\right) \tag{5-18}$$

where ρ is the density, c_v is the specific heat capacity, T is the temperature, $\mathbf{v}$ is the velocity vector, λ_f is thermal conductivity and t denotes the time. Furthermore, if c_v is a constant, the internal energy equation can be reduced to

$$\partial_t T + \mathbf{v} \cdot \nabla T = \frac{1}{\rho c_v} \nabla \cdot (\lambda \nabla T) \tag{5-19}$$

Li Q. et al. used another energy equation in their model [240]

$$\partial_t T + \mathbf{v} \cdot \nabla T = \frac{1}{\rho c_v} \nabla \cdot (\lambda \nabla T) - \frac{T}{\rho c_v} \left(\frac{\partial p_{EOS}}{\partial T} \right)_\rho \nabla \cdot \mathbf{v} \tag{5-20}$$

where p_{EOS} is the non-ideal equation of state, and this energy equation is derived from the entropy equation neglecting the viscous heat dissipation

$$\rho T \frac{Ds}{Dt} = \nabla \cdot (\lambda \nabla T) \tag{5-21}$$

with the thermodynamic relation

$$Tds = c_v dT + T \left(\frac{\partial p_{EOS}}{\partial T} \right)_\rho d\left(\frac{1}{\rho} \right) \tag{5-22}$$

where s represents the entropy. In addition, in their work it has also been reported that the thermal lattice scheme can produce a significant error by the forcing term, thus in this work all the thermal equation are solved by the classical fourth-order Runge-Kutta scheme [273].

Through some simple derivation analysis, it is not difficult to see that compared to Eq. (5-20), Eq. (5-19) uses the relationship $e = c_v T$ which is for ideal gas, where e is the internal energy, and the compression work is neglected. Besides, specific heat capacity c_v is assumed as a constant in Eq. (5-19). The entropy-based energy equation Eq. (5-20) is the standard thermal energy equation for nonideal gas.

Through studying thermal LB models using the two energy equations Eq. (5-19) and Eq. (5-20), it is found that it is much more difficult to form a multi-bubble/droplet configuration when applying Eq. (5-19). It should be pointed out that an isothermal

system is equal to a thermal LB model along with the energy equation Eq. (5-19), which means the isothermal SCMP models also suffer the same unphysical mass transfer problem.

The result shows none of the models can get rid of the unphysical mass transfer when coupling the energy equation Eq. (5-19). The following numerical simulation and discussion are based on the Li Q. et al.'s improved MRT model and the details of the model can be found in reference [240]. Following their model, the boundary conditions are set as Zou-He solid boundaries for the top and the bottom and the periodical boundaries for the left and the right to close a 200×100 computational region. For the thermal simulation, the top and bottom boundaries are constant temperature T_s and T_b with a small temperature difference $\Delta T = T_b - T_s = 0.001$ for a simple heat transfer case. It should be noticed that it is the energy equation selection that matters in this study other than the heat transfer cases. First, a single bubble with diameter 40 is simulated to test the coexistence of liquid/vapour densities by the Maxwell construction with the saturation temperature $T_s = 0.86T_c$, where T_c is the critical temperature. The coexistence densities and the Maxwell construction using Ping-Robinson EOS [253] are shown in Fig. 5-7. From the picture it can be seen the simulation result is in good agreement with the theory thermodynamic consistency.

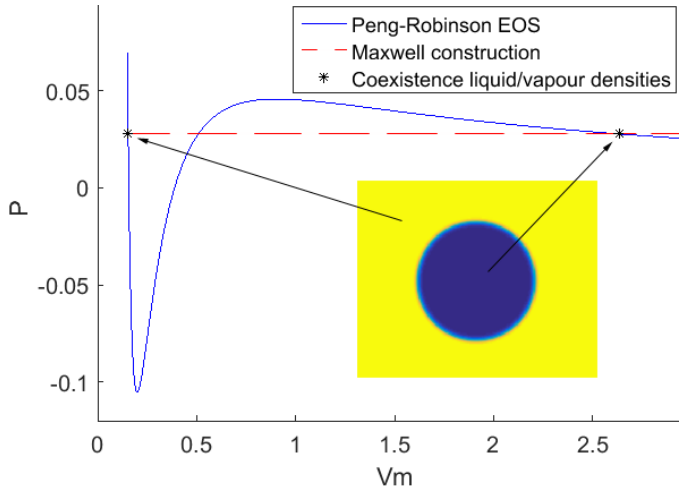

Fig. 5-7 The Maxwell construction with $T_s = 0.86T_c$ for Ping-Robinson EOS

Bubble systems and droplet systems are tested with an initial larger bubble/droplet with diameter 40 and a small one with diameter 20 using the two different energy equations. The radius variation curves of the small bubble/droplets are shown in Fig. 5-8. From the figure it can be seen that the unphysical mass transfer is much severer in bubble systems than droplet systems, which can be explained by the high-density mass attraction force, and the mass transfers faster when the bubble/droplet volume ratio increases. In addition, the problem can be effectively restrained by coupling the entropy-based energy equation Eq. (5-20).

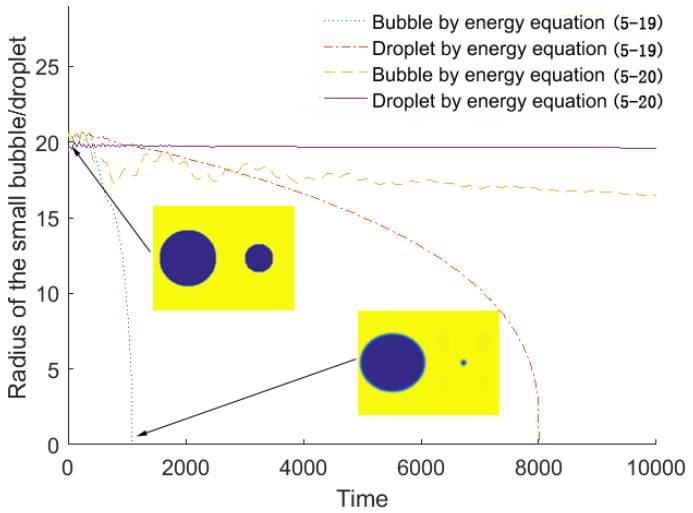

Fig. 5-8 The small bubble/droplets variations with different energy equations

Finally, in Fig. 5-9 the density fields for the two different energy equations are compared. The main difference of the two density fields is that when conducting Eq. (5-20), one layer of high density region appears outside of the bubble/droplet interface, where for Eq. (5-19) it should be the same with liquid/vapour density. This spurious density layer caused the interface nonmonotonic. If the unphysical mass transfer is caused by the spurious currents, this high-density layer might be the reason that disturbs the spurious currents and thereby restrains the phenomenon of "the big eat the small". Although the possible reason has been discussed in this work, the ultimate reason and the way to totally eliminate the unphysical phenomenon for SCMP models still need to be investigated in the future work.

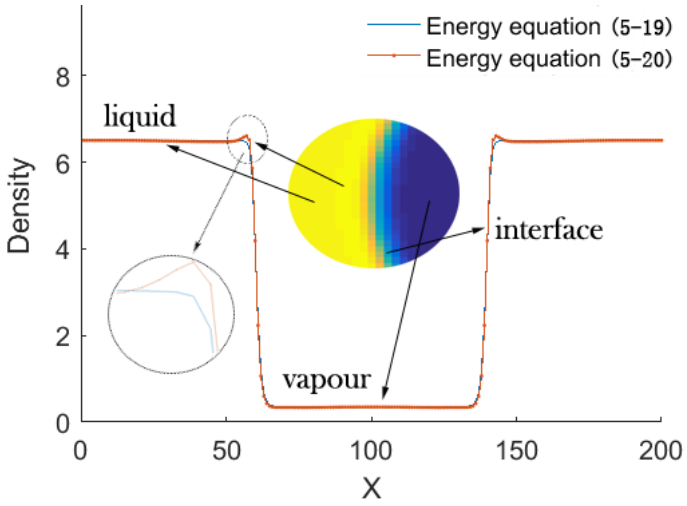

Fig. 5-9 The density variation in the cross section with different energy equations

5.5 Summary

In the present study, the new findings of a critical problem of the conventional thermal/isothermal SCMP pseudopotential LB models are reported. It is the first time this type of problem is identified and reported. After testing a number of typical models involving various forcing schemes, non-ideal equation of states and the relaxation schemes of SCMP LB models with the internal energy-based energy equation, it is

found the multiple bubbles/droplets could not coexist due to the unphysical mass transfer phenomenon, or “the big eat the small”. Meanwhile, this unphysical problem can be effectively restrained with the standard entropy-based energy equation. Although the mass transfer problem cannot be solved in this work, this study points out a reasonable orientation for the further investigation.

Chapter 6: Conclusions and outlook for further work

The subject of this work is the development and applications of the mesoscale numerical simulation method, lattice Boltzmann method. Three practical physical problems in regard to wetting phenomenon, oil/water separation and boiling heat transfer, and one LB model issue for multiphase flow are investigated. Firstly, for wetting phenomenon study, the wetting transitions between Cassie-Baxter state and Wenzel state are studied theoretically and numerically, and the energy curves during wetting transitions are proposed and numerical simulation is carried out for verification. In the second part work of oil/water separation, a multicomponent multiphase LB model coupling electric field is proposed and the oil droplets in water under electric field is studied. Experimental study is also implemented. Then in the boiling heat transfer work, a previous single component multiphase LB model is modified and the three boiling stages are accomplished using this model. Finally, the multi-bubble/droplet coexistence issue was studied for the first time, and the thermal models are considered to improve the model. The detailed conclusions and outlook for further work are given in the following sections.

6.1 Droplet Wetting Transition Study on Biomimetic Surface

In the wetting transition study, the wetting transitions for a droplet on a square-post patterned surface are theoretically analysed. Numerical simulations with a phase field lattice Boltzmann method were carried out, and the results show good agreement with the theoretical analysis. The main finding of this work is that the energy curves during wetting transitions are proposed for Cassie-to-Wenzel transition together with the reverse transition via the theoretical analysis of the free energy changes during the

transitions processes. The energy curves give a clear description of the conditions in which the transitions occur and the energy barriers exist for both transition processes. Gravity effect for wetting transition is considered, and the energy curves illustrate that the gravity can be a driving force to trigger the transition. The irreversibility is discussed based on the energy curves presented. The Wenzel-to-Cassie transition can occur spontaneously only if the inherent contact angle is large enough. It can also be concluded from the curves that different routes of the Cassie-to-Wenzel transition and the reverse transition are the main reason for the irreversibility of wetting transitions. The work is based on the regular square-post patterned surface, which is also the basis of most complicated rough surfaces. Therefore, the presented energy curves can be very helpful to understand the mechanism of complex wetting phenomena.

The numerical model is firstly validated by comparing the apparent contact angles of both homogeneous and heterogeneous wetting states with the famous Wenzel equation and Cassie-Baxter equation, and the simulation results are in good agreement with the theoretical results. Then the Cassie-to-Wenzel wetting transition and the Wenzel-to-Cassie transition processes, the energy barrier and the gravity effect on wetting transition are studied. Following summaries can be drawn from the numerical investigation:

1) For the Cassie-to-Wenzel transition, it takes much more time of the droplet on moving down along the posts side surfaces than soaking the bottom solid surface, which means the energy barrier is mainly on the vertical transition process.
2) The Wenzel-to-Cassie transition can be achieved spontaneously if an initial condition of homogeneous wetting state can be given on a surface with large Young's angle.

3) Cassie-to-Wenzel transition and the reverse transition have different routes: the former occurs mainly in the vertical direction, while the reverse transition is primarily an outer-to-inner process.
4) For the cases tested in the wetting transition work, the wetting transitions are irreversible without any external forces.
5) The two wetting states can coexist on a Wenzel state preferable surface excluding the effect from smaller scale of roughness than the scale of posts for manufactured surfaces, which means the energy barrier exists.
6) Although gravity does not have a significant influence on the shape of the droplet in microscale, it can be a crucial factor to wetting transition.
7) The truncated pyramid shape micro posts structure can improve superhydrophobicity.

The theory in the wetting transition work is based on smooth surfaces, which are difficulty to be implemented in experiment investigation. Therefore, the suitable experiment can be designed and carried out in the future to verify the theoretical model. Moreover, a quantitative analysis is expected to be finished other than the current qualitative analysis. In addition, in the future the numerical model can be used for more analysis on wetting transitions, including changing the dimensions of the patterned surface, finding the real transition critical conditions regardless of the theoretical critical state, studying the depinning of the triple line, and finding the minimum drop volume where the role of gravity can be negligible, etc.

6.2 Enhanced Oil-water Separation under Electric Field

In the oil-water separation work a multicomponent multiphase (MCMP) lattice Boltzmann method is proposed for oil/water two-phase system under electric field by

coupling the electrostatic field equation, which is also resolved in lattice Boltzmann scheme. The numerical model is firstly verified by simulating the single water droplet deformation and double droplets attracting each other in oil under strong electric field and comparing with experiment results. Both numerical and experiment studies are carried out to study the electric field force on oil droplets motions in water. The following are the summaries:

1) The proposed model can accomplish dielectrophoresis force effect for water droplet deformation and double water droplets coalescence.
2) The dielectrophoresis force can promote the coalescence of oil droplets in water.
3) Electroosmosis phenomenon can be observed in oily water in a constrained zone, i.e. two glass slides, and the oil droplets can move in a directed way towards an electrode.

The oil/water mixture involves many complicated physical problems which is quite difficult to be perfectly simulated using numerical model. Improving the numerical tools is still one of the hot topics in the further work. In addition, the way to apply the electric field on a hydrocyclone for DOWS technology needs more deep investigation. Moreover, further work including studying the electric field effect on oil/water surface tension, electric double layer of oil droplets surface and wall surface, the coalescence of oil droplets, the optimum strength of the electric field that leads to max separation, and quantifying the oil/water separation, etc should be focused on.

6.3 Mesoscale Simulation of Boiling Heat Transfer

In the boiling simulation work a phase change LB model is modified. The multiphase model is validated by Maxwell construction for liquid-vapour coexistent densities at

the saturated temperature. Then the droplet evaporation process is simulated and the D^2 law is considered. The droplets are in different initial diameters, and the squares of diameter vary linearly over time, which is also in good agreement with experimental results from the previously published paper. Finally, the three boiling stages, i.e. nucleate boiling, transition boiling and film boiling are accomplished with different superheat values acting on the bottom solid heating surface using the present model. The transient heat fluxes are given to show the heat transfer features for the three boiling stages. Overall, the modified thermal model can be used to capture the basic liquid– vapour phase change features. The results can be summarised as follows:

1) Three boiling stages: nucleate boiling, transition boiling and film boiling can be accomplished using the numerical model.
2) The modified model has a higher accuracy in terms of the pseudo potential calculation.

For the future outlook of this work, first a 3D numerical phase change needs to be built. And then a quantitative composition should be done for verification of the work. Besides, boiling is quite complicated as it involves multiphase flow and phase change. Improved models need to be proposed for a better simulation accuracy. Moreover, the mesoscale phase change model should be used to study the mechanism of boiling heat transfer, including bubble departure ratio, bubble diameter, wettability effect, residual film thickness, etc.

6.4 Investigation of Multi-bubble/droplet Coexistence Problem for SCMP Pseudopotential LBM

In the multi-bubble/droplet coexistence study, the new findings of a critical problem of the conventional thermal/isothermal SCMP pseudopotential LB models are reported.

It is the first time this type of problem is identified and reported. After testing a number of typical models involving various forcing schemes, non-ideal equation of states and the relaxation schemes of SCMP LB models with the internal energy-based energy equation, it is found the multiple bubbles/droplets could not coexist due to the unphysical mass transfer phenomenon, or “the big eat the small”. Meanwhile, this unphysical problem can be effectively restrained with an entropy-based energy equation. Although the mass transfer problem cannot be solved so far, this study points out a reasonable orientation for the further investigation. From the multi-bubble/droplet coexistence study the following summaries can be drawn:

1) The unphysical mass transfer phenomenon exists in most of the thermal SCMP pseudopotential LB models with the presented internal energy-based energy equation, of which the isothermal situation is included.
2) The mass transfer only occurs from the smaller bubble/droplets to the larger ones, but not vice versa.
3) The unphysical mass transfer is much severer in bubble systems than droplet systems, and the mass transfers faster when the bubble/droplet volume ratio increases.
4) The unphysical mass transfer can be effectively impeded by coupling the standard entropy-based energy equation.
5) A high-density layer outside of the bubble/droplet is produced by coupling the entropy-based energy equation, which might be the reason to restrain the unphysical phenomenon.
6) It is the bubbles or droplets having bigger interface curvature radii that absorb the ones with smaller interface curvature radii, and nothing to do with the volume of bubble/droplet or the area of the interface.

7) A spurious flow field of the high-density mass transfer can be generated between two bubbles or droplets.
8) The unphysical mass transfer phenomenon is consistent with the attraction force effect.
9) The unphysical mass transfer can be eliminated using MCMP pseudopotential LBM.

In the current work, the multi-bubble/droplet coexistence problem is reported but the problem has not been resolved. The reason for this issue is still unclear, in the future work deeper investigations should be implemented to further study the mechanism of the problem and resolve this problem to have a broader application of the popular SCMP LB models.

References

1. Bergman, T.L., F.P. Incropera, D.P. DeWitt, and A.S. Lavine, *Fundamentals of heat and mass transfer*. 2011: John Wiley & Sons.
2. Brennen, C.E. and C.E. Brennen, *Fundamentals of multiphase flow*. 2005: Cambridge university press.
3. Launder, B.E. and D.B. Spalding, *Mathematical models of turbulence*. 1972: Academic press.
4. Sagaut, P., *Large eddy simulation for incompressible flows: an introduction*. 2006: Springer Science & Business Media.
5. Moser, R.D., J. Kim, and N.N. Mansour, *Direct numerical simulation of turbulent channel flow up to Re τ= 590.* Physics of fluids, 1999. **11**(4): p. 943-945.
6. Panagiotopoulos, A.Z., *Direct determination of phase coexistence properties of fluids by Monte Carlo simulation in a new ensemble.* Molecular Physics, 1987. **61**(4): p. 813-826.
7. Hoogerbrugge, P. and J. Koelman, *Simulating microscopic hydrodynamic phenomena with dissipative particle dynamics.* EPL (Europhysics Letters), 1992. **19**(3): p. 155.
8. Kresse, G. and J. Hafner, *Ab initio molecular dynamics for liquid metals.* Physical Review B, 1993. **47**(1): p. 558.
9. Karniadakis, G., A. Beskok, and N. Aluru, *Microflows and nanoflows: fundamentals and simulation*. Vol. 29. 2006: Springer Science & Business Media.
10. Guo, Z.L. and C. Zheng, *Theory and applications of lattice Boltzmann method.* Science, Beijing, 2009.

11. Luo, K., J. Xia, and E. Monaco, *Multiscale modeling of multiphase flow with complex interactions.* Journal of Multiscale Modelling, 2009. **1**(01): p. 125-156.

12. Succi, S., *The lattice Boltzmann equation: for fluid dynamics and beyond*. 2001: Oxford university press.

13. Wolf-Gladrow, D.A., *Lattice-gas cellular automata and lattice Boltzmann models: an introduction*. 2004: Springer.

14. Benzi, R., S. Succi, and M. Vergassola, *The lattice Boltzmann equation: theory and applications.* Physics Reports, 1992. **222**(3): p. 145-197.

15. Karlin, I.V., A.N. Gorban, S. Succi, and V. Boffi, *Maximum entropy principle for lattice kinetic equations.* Physical Review Letters, 1998. **81**(1): p. 6.

16. Succi, S., *Lattice Boltzmann across scales: from turbulence to DNA translocation.* The European Physical Journal B, 2008. **64**(3-4): p. 471-479.

17. Chen, S. and G.D. Doolen, *Lattice Boltzmann method for fluid flows.* Annual review of fluid mechanics, 1998. **30**(1): p. 329-364.

18. d'Humieres, D., *Generalized lattice-Boltzmann equations.* Rarefied gas dynamics, 1992.

19. d'Humières, D., *Multiple–relaxation–time lattice Boltzmann models in three dimensions.* Philosophical Transactions of the Royal Society of London A: Mathematical, Physical and Engineering Sciences, 2002. **360**(1792): p. 437-451.

20. Luo, L.-S., W. Liao, X. Chen, Y. Peng, and W. Zhang, *Numerics of the lattice Boltzmann method: Effects of collision models on the lattice Boltzmann simulations.* Physical Review E, 2011. **83**(5): p. 056710.

21. Ginzburg, I., *Equilibrium-type and link-type lattice Boltzmann models for generic advection and anisotropic-dispersion equation.* Advances in water resources, 2005. **28**(11): p. 1171-1195.

22. Ginzburg, I., D. d'Humières, and A. Kuzmin, *Optimal stability of advection-diffusion lattice Boltzmann models with two relaxation times for positive/negative equilibrium.* Journal of Statistical Physics, 2010. **139**(6): p. 1090-1143.

23. Kuzmin, A., I. Ginzburg, and A. Mohamad, *The role of the kinetic parameter in the stability of two-relaxation-time advection–diffusion lattice Boltzmann schemes.* Computers & Mathematics with Applications, 2011. **61**(12): p. 3417-3442.

24. Ansumali, S. and I.V. Karlin, *Single relaxation time model for entropic lattice Boltzmann methods.* Physical Review E, 2002. **65**(5): p. 056312.

25. Boghosian, B.M., J. Yepez, P.V. Coveney, and A. Wager. *Entropic lattice Boltzmann methods*. in *Proceedings of the Royal Society of London A: Mathematical, Physical and Engineering Sciences*. 2001. The Royal Society.

26. Ansumali, S., I. Karlin, C.E. Frouzakis, and K. Boulouchos, *Entropic lattice Boltzmann method for microflows.* Physica A: Statistical Mechanics and its Applications, 2006. **359**: p. 289-305.

27. Chikatamarla, S., S. Ansumali, and I.V. Karlin, *Entropic lattice Boltzmann models for hydrodynamics in three dimensions.* Physical review letters, 2006. **97**(1): p. 010201.

28. Geier, M., A. Greiner, and J.G. Korvink, *Cascaded digital lattice Boltzmann automata for high Reynolds number flow.* Physical Review E, 2006. **73**(6): p. 066705.

29. Chikatamarla, S.S. and I.V. Karlin, *Entropic lattice Boltzmann method for turbulent flow simulations: Boundary conditions.* Physica A: Statistical Mechanics and its Applications, 2013. **392**(9): p. 1925-1930.

30. Lycett-Brown, D. and K.H. Luo, *Multiphase cascaded lattice Boltzmann method.* Computers & Mathematics with Applications, 2014. **67**(2): p. 350-362.

31. Geller, S., S. Uphoff, and M. Krafczyk, *Turbulent jet computations based on MRT and Cascaded Lattice Boltzmann models.* Computers & Mathematics with Applications, 2013. **65**(12): p. 1956-1966.

32. Premnath, K.N. and S. Banerjee, *Incorporating forcing terms in cascaded lattice Boltzmann approach by method of central moments.* Physical Review E, 2009. **80**(3): p. 036702.

33. Guo, Z., C. Zheng, and B. Shi, *Discrete lattice effects on the forcing term in the lattice Boltzmann method.* Physical Review E, 2002. **65**(4): p. 046308.

34. He, X., X. Shan, and G.D. Doolen, *Discrete Boltzmann equation model for nonideal gases.* Physical Review E, 1998. **57**(1): p. R13.

35. Kupershtokh, A. *New method of incorporating a body force term into the lattice Boltzmann equation*. in *Proc. 5th International EHD Workshop, University of Poitiers, Poitiers, France*. 2004.

36. Zheng, L., B. Shi, and Z. Guo, *Multiple-relaxation-time model for the correct thermohydrodynamic equations.* Physical Review E, 2008. **78**(2): p. 026705.

37. Li, Q., K.H. Luo, and X. Li, *Forcing scheme in pseudopotential lattice Boltzmann model for multiphase flows.* Physical Review E, 2012. **86**(1): p. 016709.

38. McCracken, M.E. and J. Abraham, *Multiple-relaxation-time lattice-Boltzmann model for multiphase flow.* Physical Review E, 2005. **71**(3): p. 036701.

39. Shi, X. and S.P. Lim, *A LBM–DLM/FD method for 3D fluid–structure interactions.* Journal of Computational Physics, 2007. **226**(2): p. 2028-2043.

40. Kwon, Y., *Development of coupling technique for LBM and FEM for FSI application.* Engineering computations, 2006. **23**(8): p. 860-875.

41. Han, Y. and P.A. Cundall, *LBM–DEM modeling of fluid–solid interaction in porous media.* International Journal for Numerical and Analytical Methods in Geomechanics, 2013. **37**(10): p. 1391-1407.

42. Luan, H.-B., H. Xu, L. Chen, D.-L. Sun, Y.-L. He, and W.-Q. Tao, *Evaluation of the coupling scheme of FVM and LBM for fluid flows around complex geometries.* International journal of heat and mass transfer, 2011. **54**(9-10): p. 1975-1985.

43. Lee, T. and C.-L. Lin, *A stable discretization of the lattice Boltzmann equation for simulation of incompressible two-phase flows at high density ratio.* Journal of Computational Physics, 2005. **206**(1): p. 16-47.

44. He, X., S. Chen, and R. Zhang, *A lattice Boltzmann scheme for incompressible multiphase flow and its application in simulation of Rayleigh–Taylor instability.* Journal of Computational Physics, 1999. **152**(2): p. 642-663.

45. Pooley, C. and K. Furtado, *Eliminating spurious velocities in the free-energy lattice Boltzmann method.* Physical Review E, 2008. **77**(4): p. 046702.

46. Kalarakis, A., V. Burganos, and A. Payatakes, *Galilean-invariant lattice-Boltzmann simulation of liquid-vapor interface dynamics.* Physical review e, 2002. **65**(5): p. 056702.

47. Reis, T. and T. Phillips, *Lattice Boltzmann model for simulating immiscible two-phase flows.* Journal of Physics A: Mathematical and Theoretical, 2007. **40**(14): p. 4033.

48. Latva-Kokko, M. and D.H. Rothman, *Diffusion properties of gradient-based lattice Boltzmann models of immiscible fluids.* Physical Review E, 2005. **71**(5): p. 056702.

49. Grunau, D., S. Chen, and K. Eggert, *A lattice Boltzmann model for multiphase fluid flows.* Physics of Fluids A: Fluid Dynamics, 1993. **5**(10): p. 2557-2562.

50. Chen, F., A. Xu, G. Zhang, Y. Li, and S. Succi, *Multiple-relaxation-time lattice Boltzmann approach to compressible flows with flexible specific-heat ratio and Prandtl number.* EPL (Europhysics Letters), 2010. **90**(5): p. 54003.

51. Chikatamarla, S.S. and I.V. Karlin, *Complete Galilean invariant lattice Boltzmann models.* Computer physics communications, 2008. **179**(1-3): p. 140-143.

52. Yan-Biao, G., X. Ai-Guo, Z. Guang-Cai, and L. Ying-Jun, *FFT-LB modeling of thermal liquid-vapor system.* Communications in Theoretical Physics, 2012. **57**(4): p. 681.

53. Chen, F., A. Xu, G. Zhang, and Y. Li, *Multiple-relaxation-time lattice Boltzmann model for compressible fluids.* Physics Letters A, 2011. **375**(21): p. 2129-2139.

54. Scagliarini, A., L. Biferale, M. Sbragaglia, K. Sugiyama, and F. Toschi, *Lattice Boltzmann methods for thermal flows: Continuum limit and applications to compressible Rayleigh–Taylor systems.* Physics of Fluids, 2010. **22**(5): p. 055101.

55. Frapolli, N., S. Chikatamarla, and I. Karlin, *Multispeed entropic lattice Boltzmann model for thermal flows.* Physical Review E, 2014. **90**(4): p. 043306.

56. Xu, A.-G., G.-C. Zhang, Y.-B. Gan, F. Chen, and X.-J. Yu, *Lattice Boltzmann modeling and simulation of compressible flows.* Frontiers of Physics, 2012. **7**(5): p. 582-600.

57. Gan, Y., A. Xu, G. Zhang, and Y. Yang, *Lattice BGK kinetic model for high-speed compressible flows: Hydrodynamic and nonequilibrium behaviors.* EPL (Europhysics Letters), 2013. **103**(2): p. 24003.

58. Gan, Y., A. Xu, G. Zhang, P. Zhang, and Y. Li, *Lattice Boltzmann study of thermal phase separation: Effects of heat conduction, viscosity and Prandtl number.* EPL (Europhysics Letters), 2012. **97**(4): p. 44002.

59. Karlin, I., D. Sichau, and S. Chikatamarla, *Consistent two-population lattice Boltzmann model for thermal flows.* Physical Review E, 2013. **88**(6): p. 063310.

60. Huang, R. and H. Wu, *A modified multiple-relaxation-time lattice Boltzmann model for convection–diffusion equation.* Journal of Computational Physics, 2014. **274**: p. 50-63.

61. Chai, Z. and T. Zhao, *Lattice Boltzmann model for the convection-diffusion equation.* Physical Review E, 2013. **87**(6): p. 063309.

62. Chatterjee, D., *An enthalpy-based thermal lattice Boltzmann model for non-isothermal systems.* EPL (Europhysics Letters), 2009. **86**(1): p. 14004.

63. Chen, Q., X. Zhang, and J. Zhang, *Effects of Reynolds and Prandtl numbers on heat transfer around a circular cylinder by the simplified thermal lattice Boltzmann model.* Communications in Computational Physics, 2015. **17**(4): p. 937-959.

64. Mohamad, A., R. Bennacer, and M. El-Ganaoui, *Double dispersion, natural convection in an open end cavity simulation via Lattice Boltzmann Method.* International Journal of Thermal Sciences, 2010. **49**(10): p. 1944-1953.

65. Zhu, M., D. Sun, S. Pan, Q. Zhang, and D. Raabe, *Modelling of dendritic growth during alloy solidification under natural convection.* Modelling and Simulation in Materials Science and Engineering, 2014. **22**(3): p. 034006.

66. Chen, H., S. Kandasamy, S. Orszag, R. Shock, S. Succi, and V. Yakhot, *Extended Boltzmann kinetic equation for turbulent flows.* Science, 2003. **301**(5633): p. 633-636.

67. Eggels, J.G., *Direct and large-eddy simulation of turbulent fluid flow using the lattice-Boltzmann scheme.* International journal of heat and fluid flow, 1996. **17**(3): p. 307-323.

68. Hou, S., J. Sterling, S. Chen, and G. Doolen, *A lattice Boltzmann subgrid model for high Reynolds number flows.* arXiv preprint comp-gas/9401004, 1994.

69. Karlin, I.V., A. Ferrante, and H.C. Öttinger, *Perfect entropy functions of the lattice Boltzmann method.* EPL (Europhysics Letters), 1999. **47**(2): p. 182.

70. Teixeira, C.M., *Incorporating turbulence models into the lattice-Boltzmann method.* International Journal of Modern Physics C, 1998. **9**(08): p. 1159-1175.

71. Yu, H., L.-S. Luo, and S.S. Girimaji, *LES of turbulent square jet flow using an MRT lattice Boltzmann model.* Computers & Fluids, 2006. **35**(8-9): p. 957-965.

72. Amati, G., S. Succi, and R. Piva, *Massively parallel lattice-Boltzmann simulation of turbulent channel flow.* International Journal of Modern Physics C, 1997. **8**(04): p. 869-877.

73. Yu, H., S.S. Girimaji, and L.-S. Luo, *DNS and LES of decaying isotropic turbulence with and without frame rotation using lattice Boltzmann method.* Journal of Computational Physics, 2005. **209**(2): p. 599-616.

74. Mendoza, M. and J. Munoz, *Three-dimensional lattice Boltzmann model for electrodynamics.* Physical Review E, 2010. **82**(5): p. 056708.

75. Dellar, P., *Electromagnetic waves in lattice Boltzmann magnetohydrodynamics.* EPL (Europhysics Letters), 2010. **90**(5): p. 50002.

76. Timm, K., H. Kusumaatmaja, and A. Kuzmin, *The lattice Boltzmann method: principles and practice*. 2016, Springer: Berlin, Germany.

77. He, Y.-L., Q. Liu, Q. Li, and W.-Q. Tao, *Lattice Boltzmann methods for single-phase and solid-liquid phase-change heat transfer in porous media: A review.* International Journal of Heat and Mass Transfer, 2019. **129**: p. 160-197.

78. He, Y., Y. Wang, and Q. Li, *Lattice Boltzmann method: theory and applications.* Science, Beijing, 2009.

79. Yan, Y.Y., Y.Q. Zu, and B. Dong, *LBM, a useful tool for mesoscale modelling of single-phase and multiphase flow.* Applied Thermal Engineering, 2011. **31**(5): p. 649-655.

80. Ye, F., Q. Di, W. Wang, F. Chen, H. Chen, and S. Hua, *Comparative study of two lattice Boltzmann multiphase models for simulating wetting phenomena: implementing static contact angles based on the geometric formulation.* Applied Mathematics and Mechanics, 2018. **39**(4): p. 513-528.

81. Li, M., C. Huber, W. Tao, and J. Wei, *Study on nucleation position and wetting state for dropwise condensation on rough structures with different wettability using multiphase lattice Boltzmann method.* International Journal of Heat and Mass Transfer, 2019. **131**: p. 96-100.

82. Liu, X. and P. Cheng, *Lattice Boltzmann simulation for dropwise condensation of vapor along vertical hydrophobic flat plates.* International Journal of Heat and Mass Transfer, 2013. **64**: p. 1041-1052.

83. Zhou, P., W. Liu, and Z. Liu, *Lattice Boltzmann simulation of nucleate boiling in micro-pillar structured surface.* International Journal of Heat and Mass Transfer, 2019. **131**: p. 1-10.

84. Yang, W., H. Huang, and W. Yan, *Thermal Lattice Boltzmann Simulation of Evaporating Thin Liquid Film for Vapor Generation.* Applied Sciences, 2018. **8**(5): p. 798.

85. Sadeghi, R., M.S. Shadloo, M. Hopp-Hirschler, A. Hadjadj, and U. Nieken, *Three-dimensional lattice Boltzmann simulations of high density ratio two-phase flows in porous media.* Computers & Mathematics with Applications, 2018. **75**(7): p. 2445-2465.

86. Zhao, J., Q. Kang, J. Yao, H. Viswanathan, R. Pawar, L. Zhang, and H. Sun, *The Effect of Wettability Heterogeneity on Relative Permeability of Two‐Phase Flow in Porous Media: A Lattice Boltzmann Study.* Water Resources Research, 2018. **54**(2): p. 1295-1311.

87. Cheng, Z., Z. Ning, Q. Wang, Y. Zeng, R. Qi, L. Huang, and W. Zhang, *The effect of pore structure on non-Darcy flow in porous media using the lattice Boltzmann method.* Journal of Petroleum Science and Engineering, 2019. **172**: p. 391-400.

88. Chen, S., Y.Y. Yan, and W. Gong, *A simple lattice Boltzmann model for conjugate heat transfer research.* International Journal of Heat and Mass Transfer, 2017. **107**: p. 862-870.

89. Ross-Jones, J., M. Gaedtke, S. Sonnick, M. Rädle, H. Nirschl, and M.J. Krause, *Conjugate heat transfer through nano scale porous media to optimize vacuum insulation panels with lattice Boltzmann methods.* Computers & Mathematics with Applications, 2019. **77**(1): p. 209-221.

90. Zhang, D., Q. Cai, O.O. Taiwo, V. Yufit, N.P. Brandon, and S. Gu, *The effect of wetting area in carbon paper electrode on the performance of vanadium redox flow batteries: A three-dimensional lattice Boltzmann study.* Electrochimica Acta, 2018. **283**: p. 1806-1819.

91. Jiang, Z., Z. Qu, and L. Zhou, *Lattice Boltzmann simulation of ion and electron transport during the discharge process in a randomly reconstructed porous electrode of a lithium-ion battery.* International Journal of Heat and Mass Transfer, 2018. **123**: p. 500-513.

92. Jiang, J., D. Li, and R. Dou, *A lattice Boltzmann modeling and analysis of the thermal convection in a lithium-ion battery.* Computers & Mathematics with Applications, 2019.

93. Tang, G., Z. Li, J. Wang, Y. He, and W. Tao, *Electroosmotic flow and mixing in microchannels with the lattice Boltzmann method.* Journal of Applied Physics, 2006. **100**(9): p. 094908.

94. Li, B., W. Zhou, Y. Yan, Z. Han, and L. Ren, *Numerical Modelling of Electroosmotic Driven Flow in Nanoporous Media by Lattice Boltzmann Method.* Journal of Bionic Engineering, 2013. **10**(1): p. 90-99.

95. Zu, Y. and Y. Yan, *Numerical simulation of electroosmotic flow near earthworm surface.* Journal of Bionic Engineering, 2006. **3**(4): p. 179-186.

96. Dong, B., Y.Y. Yan, W. Li, and Y. Song, *Lattice Boltzmann simulation of viscous fingering phenomenon of immiscible fluids displacement in a channel.* Computers & Fluids, 2010. **39**(5): p. 768-779.

97. Dong, B., Y. Yan, and W. Li, *LBM simulation of viscous fingering phenomenon in immiscible displacement of two fluids in porous media.* Transport in porous media, 2011. **88**(2): p. 293-314.

98. Lim, C., C. Shu, X. Niu, and Y. Chew, *Application of lattice Boltzmann method to simulate microchannel flows.* Physics of fluids, 2002. **14**(7): p. 2299-2308.

99. Pravinraj, T. and R. Patrikar, *Modeling and characterization of surface roughness effect on fluid flow in a polydimethylsiloxane microchannel using a fractal based lattice Boltzmann method.* AIP Advances, 2018. **8**(6): p. 065112.

100. Zhang, L., X. Cheng, T. Ku, Y. Song, and D. Zhang, *Lattice Boltzmann study of successive droplets impingement on the non-ideal recessed microchannel for high-resolution features.* International Journal of Heat and Mass Transfer, 2018. **120**: p. 1085-1100.

101. Mohebbi, R., M. Rashidi, M. Izadi, N.A.C. Sidik, and H.W. Xian, *Forced convection of nanofluids in an extended surfaces channel using lattice Boltzmann method.* International Journal of Heat and Mass Transfer, 2018. **117**: p. 1291-1303.

102. Sheikholeslami, M., T. Hayat, T. Muhammad, and A. Alsaedi, *MHD forced convection flow of nanofluid in a porous cavity with hot elliptic obstacle by means of Lattice Boltzmann method.* International Journal of Mechanical Sciences, 2018. **135**: p. 532-540.

103. Sheikholeslami, M., M. Gorji-Bandpy, and D. Ganji, *Lattice Boltzmann method for MHD natural convection heat transfer using nanofluid.* Powder Technology, 2014. **254**: p. 82-93.

104. Sheikholeslami, M. and D.D. Ganji, *Entropy generation of nanofluid in presence of magnetic field using Lattice Boltzmann Method.* Physica A: Statistical Mechanics and its Applications, 2015. **417**: p. 273-286.

105. Xuan, Y. and Z. Yao, *Lattice Boltzmann model for nanofluids.* Heat and mass transfer, 2005. **41**(3): p. 199-205.

106. Lai, H. and C. Ma, *A higher order lattice BGK model for simulating some nonlinear partial differential equations.* Science in China Series G: Physics, Mechanics and Astronomy, 2009. **52**(7): p. 1053-1061.

107. Chai, Z. and B. Shi, *A novel lattice Boltzmann model for the Poisson equation.* Applied mathematical modelling, 2008. **32**(10): p. 2050-2058.

108. Chai, Z., B. Shi, and L. Zheng, *A unified lattice Boltzmann model for some nonlinear partial differential equations.* Chaos, Solitons & Fractals, 2008. **36**(4): p. 874-882.

109. Qian, Y., D. d'Humières, and P. Lallemand, *Lattice BGK models for Navier-Stokes equation.* EPL (Europhysics Letters), 1992. **17**(6): p. 479.

110. Chen, S., H. Chen, D. Martnez, and W. Matthaeus, *Lattice Boltzmann model for simulation of magnetohydrodynamics.* Physical Review Letters, 1991. **67**(27): p. 3776.

111. Bhatnagar, P.L., E.P. Gross, and M. Krook, *A model for collision processes in gases. I. Small amplitude processes in charged and neutral one-component systems.* Physical review, 1954. **94**(3): p. 511.

112. He, X. and L.-S. Luo, *Theory of the lattice Boltzmann method: From the Boltzmann equation to the lattice Boltzmann equation.* Physical Review E, 1997. **56**(6): p. 6811.

113. Li, Q., K.H. Luo, Q.J. Kang, Y.L. He, Q. Chen, and Q. Liu, *Lattice Boltzmann methods for multiphase flow and phase-change heat transfer*. Progress in Energy and Combustion Science, 2015.

114. McNamara, G.R. and G. Zanetti, *Use of the Boltzmann equation to simulate lattice-gas automata.* Physical review letters, 1988. **61**(20): p. 2332.

115. Chen, S., D. Martinez, and R. Mei, *On boundary conditions in lattice Boltzmann methods.* Physics of fluids, 1996. **8**(9): p. 2527-2536.

116. Ziegler, D.P., *Boundary conditions for lattice Boltzmann simulations.* Journal of Statistical Physics, 1993. **71**(5-6): p. 1171-1177.

117. Zou, Q. and X. He, *On pressure and velocity boundary conditions for the lattice Boltzmann BGK model.* Physics of Fluids, 1997. **9**(6): p. 1591.

118. Inamuro, T., M. Yoshino, and F. Ogino, *A non‐slip boundary condition for lattice Boltzmann simulations.* Physics of Fluids, 1995. **7**(12): p. 2928-2930.

119. Zhao-Li, G., Z. Chu-Guang, and S. Bao-Chang, *Non-equilibrium extrapolation method for velocity and pressure boundary conditions in the lattice Boltzmann method.* Chinese Physics, 2002. **11**(4): p. 366.

120. Filippova, O. and D. Hänel, *Grid refinement for lattice-BGK models.* Journal of Computational physics, 1998. **147**(1): p. 219-228.

121. Mei, R., L.-S. Luo, and W. Shyy, *An accurate curved boundary treatment in the lattice Boltzmann method.* Journal of computational physics, 1999. **155**(2): p. 307-330.

122. Lallemand, P. and L.-S. Luo, *Lattice Boltzmann method for moving boundaries.* Journal of Computational Physics, 2003. **184**(2): p. 406-421.

123. Ginzburg, I. and D. d'Humieres, *Multireflection boundary conditions for lattice Boltzmann models.* Physical Review E, 2003. **68**(6): p. 066614.

124. Guo, Z., C. Zheng, and B. Shi, *An extrapolation method for boundary conditions in lattice Boltzmann method.* Physics of Fluids, 2002. **14**(6): p. 2007-2010.

125. Hirt, C.W. and B.D. Nichols, *Volume of fluid (VOF) method for the dynamics of free boundaries.* Journal of computational physics, 1981. **39**(1): p. 201-225.

126. Sethian, J.A., *Level set methods and fast marching methods: evolving interfaces in computational geometry, fluid mechanics, computer vision, and materials science*. Vol. 3. 1999: Cambridge university press.

127. Liu, H., A.J. Valocchi, and Q. Kang, *Three-dimensional lattice Boltzmann model for immiscible two-phase flow simulations.* Physical Review E, 2012. **85**(4): p. 046309.

128. Scardovelli, R. and S. Zaleski, *Direct numerical simulation of free-surface and interfacial flow.* Annual review of fluid mechanics, 1999. **31**(1): p. 567-603.

129. Gunstensen, A.K., D.H. Rothman, S. Zaleski, and G. Zanetti, *Lattice Boltzmann model of immiscible fluids.* Physical Review A, 1991. **43**(8): p. 4320.

130. Shan, X. and H. Chen, *Lattice Boltzmann model for simulating flows with multiple phases and components.* Physical Review E, 1993. **47**(3): p. 1815-1819.

131. Shan, X. and H. Chen, *Simulation of nonideal gases and liquid-gas phase transitions by the lattice Boltzmann equation.* Physical Review E, 1994. **49**(4): p. 2941.

132. Swift, M.R., W. Osborn, and J. Yeomans, *Lattice Boltzmann simulation of nonideal fluids.* Physical review letters, 1995. **75**(5): p. 830.

133. Swift, M.R., E. Orlandini, W. Osborn, and J. Yeomans, *Lattice Boltzmann simulations of liquid-gas and binary fluid systems.* Physical Review E, 1996. **54**(5): p. 5041.

134. Yan, Y.Y. and Y.Q. Zu, *A lattice Boltzmann method for incompressible two-phase flows on partial wetting surface with large density ratio.* Journal of Computational Physics, 2007. **227**(1): p. 763-775.

135. d'Ortona, U., D. Salin, M. Cieplak, R.B. Rybka, and J.R. Banavar, *Two-color nonlinear Boltzmann cellular automata: Surface tension and wetting.* Physical Review E, 1995. **51**(4): p. 3718.

136. Lishchuk, S., C. Care, and I. Halliday, *Lattice Boltzmann algorithm for surface tension with greatly reduced microcurrents.* Physical review E, 2003. **67**(3): p. 036701.

137. Ahrenholz, B., J. Tölke, P. Lehmann, A. Peters, A. Kaestner, M. Krafczyk, and W. Durner, *Prediction of capillary hysteresis in a porous material using lattice-Boltzmann methods and comparison to experimental data and a morphological pore network model.* Advances in Water Resources, 2008. **31**(9): p. 1151-1173.

138. Huang, H., J.-J. Huang, X.-Y. Lu, and M.C. Sukop, *On simulations of high-density ratio flows using color-gradient multiphase lattice Boltzmann models.* International Journal of Modern Physics C, 2013. **24**(04): p. 1350021.

139. Inamuro, T., N. Konishi, and F. Ogino, *A Galilean invariant model of the lattice Boltzmann method for multiphase fluid flows using free-energy approach.* Computer physics communications, 2000. **129**(1-3): p. 32-45.

140. Jacqmin, D., *Calculation of two-phase Navier–Stokes flows using phase-field modeling.* Journal of Computational Physics, 1999. **155**(1): p. 96-127.

141. Li, L., X. Liu, X.J. Dai, L. Li, and Y. Chen, *Surface wetting processing on BNNT films by selective plasma modes.* Chinese science bulletin, 2013. **58**(27): p. 3403-3408.

142. Yao, J., J. Wang, Y. Yu, H. Yang, and Y. Xu, *Biomimetic fabrication and characterization of an artificial rice leaf surface with anisotropic wetting.* Chinese science bulletin, 2012. **57**(20): p. 2631-2634.

143. Yao, Z., P. Hao, X. Zhang, and F. He, *Static and dynamic characterization of droplets on hydrophobic surfaces.* Chinese science bulletin, 2012. **57**(10): p. 1095-1101.

144. Yan, Y., *Physical and numerical modelling of biomimetic approaches of natural hydrophobic surfaces.* Chinese Science Bulletin, 2009. **54**(4): p. 541.

145. Gao, N., Y. Yan, X. Chen, and D.J. Mee, *Nanoparticle-induced morphology and hydrophilicity of structured surfaces.* Langmuir, 2012. **28**(33): p. 12256-12265.

146. Huang, Y., Y. Hu, C. Zhu, F. Zhang, H. Li, X. Lu, and S. Meng, *Long‐Lived Multifunctional Superhydrophobic Heterostructure Via Molecular Self‐Supply.* Advanced Materials Interfaces, 2016. **3**(5): p. 1500727.

147. Koch, K., B. Bhushan, and W. Barthlott, *Multifunctional surface structures of plants: an inspiration for biomimetics.* Progress in Materials Science, 2009. **54**(2): p. 137-178.

148. Zhang, Y.-L., H. Xia, E. Kim, and H.-B. Sun, *Recent developments in superhydrophobic surfaces with unique structural and functional properties.* Soft Matter, 2012. **8**(44): p. 11217-11231.

149. Young, T., *An essay on the cohesion of fluids.* Philosophical Transactions of the Royal Society of London, 1805. **95**: p. 65-87.

150. Wenzel, R.N., *Surface Roughness and Contact Angle.* The Journal of Physical Chemistry, 1949. **53**(9): p. 1466-1467.

151. Cassie, A. and S. Baxter, *Wettability of porous surfaces.* Transactions of the Faraday Society, 1944. **40**: p. 546-551.

152. Patankar, N.A., *Transition between superhydrophobic states on rough surfaces.* Langmuir, 2004. **20**(17): p. 7097-7102.

153. Gao, N. and Y. Yan, *Modeling Superhydrophobic Contact Angles and Wetting Transition.* Journal of Bionic Engineering, 2009. **6**(4): p. 335-340.

154. Yan, Y., N. Gao, and W. Barthlott, *Mimicking natural superhydrophobic surfaces and grasping the wetting process: A review on recent progress in preparing superhydrophobic surfaces.* Advances in colloid and interface science, 2011. **169**(2): p. 80-105.

155. Marmur, A. and E. Bittoun, *When Wenzel and Cassie are right: reconciling local and global considerations.* Langmuir, 2009. **25**(3): p. 1277-1281.

156. Marmur, A., *From hygrophilic to superhygrophobic: theoretical conditions for making high-contact-angle surfaces from low-contact-angle materials.* Langmuir, 2008. **24**(14): p. 7573-7579.

157. Ran, C., G. Ding, W. Liu, Y. Deng, and W. Hou, *Wetting on nanoporous alumina surface: transition between Wenzel and Cassie states controlled by surface structure.* Langmuir, 2008. **24**(18): p. 9952-9955.

158. Koishi, T., K. Yasuoka, S. Fujikawa, T. Ebisuzaki, and X.C. Zeng, *Coexistence and transition between Cassie and Wenzel state on pillared hydrophobic surface.* Proceedings of the National Academy of Sciences, 2009. **106**(21): p. 8435-8440.

159. Bormashenko, E., *Wetting transitions on biomimetic surfaces.* Philos Trans A Math Phys Eng Sci, 2010. **368**(1929): p. 4695-711.

160. Bormashenko, E., *Progress in understanding wetting transitions on rough surfaces.* Adv Colloid Interface Sci, 2015. **222**: p. 92-103.

161. Lafuma, A. and D. Quéré, *Superhydrophobic states.* Nature materials, 2003. **2**(7): p. 457.

162. Jung, Y.C. and B. Bhushan, *Dynamic effects induced transition of droplets on biomimetic superhydrophobic surfaces.* Langmuir, 2009. **25**(16): p. 9208-9218.

163. McHale, G., S. Aqil, N. Shirtcliffe, M. Newton, and H.Y. Erbil, *Analysis of droplet evaporation on a superhydrophobic surface.* Langmuir, 2005. **21**(24): p. 11053-11060.

164. Bormashenko, E., R. Pogreb, G. Whyman, and M. Erlich, *Resonance Cassie–Wenzel wetting transition for horizontally vibrated drops deposited on a rough surface.* Langmuir, 2007. **23**(24): p. 12217-12221.

165. Bahadur, V. and S.V. Garimella, *Electrowetting-based control of droplet transition and morphology on artificially microstructured surfaces.* Langmuir, 2008. **24**(15): p. 8338-8345.

166. Krupenkin, T.N., J.A. Taylor, E.N. Wang, P. Kolodner, M. Hodes, and T.R. Salamon, *Reversible wetting-dewetting transitions on electrically tunable superhydrophobic nanostructured surfaces.* Langmuir, 2007. **23**(18): p. 9128-9133.

167. Zu, Y. and Y. Yan, *Single droplet on micro square-post patterned surfaces–theoretical model and numerical simulation.* Scientific reports, 2016. **6**: p. 19281.

168. Whyman, G. and E. Bormashenko, *Wetting transitions on rough substrates: General considerations.* Journal of Adhesion Science and Technology, 2012. **26**(1-3): p. 207-220.

169. Ren, W., *Wetting transition on patterned surfaces: transition states and energy barriers.* Langmuir, 2014. **30**(10): p. 2879-2885.

170. Pashos, G., G. Kokkoris, and A.G. Boudouvis, *Minimum energy paths of wetting transitions on grooved surfaces.* Langmuir, 2015. **31**(10): p. 3059-3068.

171. Pashos, G., G. Kokkoris, A. Papathanasiou, and A. Boudouvis, *Wetting transitions on patterned surfaces with diffuse interaction potentials embedded in a Young-Laplace formulation.* The Journal of chemical physics, 2016. **144**(3): p. 034105.

172. Prakash, S., E. Xi, and A.J. Patel, *Spontaneous recovery of superhydrophobicity on nanotextured surfaces.* Proceedings of the National Academy of Sciences, 2016. **113**(20): p. 5508-5513.

173. Bico, J., U. Thiele, and D. Quéré, *Wetting of textured surfaces.* Colloids and Surfaces A: Physicochemical and Engineering Aspects, 2002. **206**(1-3): p. 41-46.

174. Bormashenko, E., R. Pogreb, T. Stein, G. Whyman, M. Erlich, A. Musin, V. Machavariani, and D. Aurbach, *Characterization of rough surfaces with vibrated drops.* Physical Chemistry Chemical Physics, 2008. **10**(27): p. 4056-4061.

175. Dupuis, A. and J. Yeomans, *Modeling droplets on superhydrophobic surfaces: equilibrium states and transitions.* Langmuir, 2005. **21**(6): p. 2624-2629.

176. Vrancken, R.J., H. Kusumaatmaja, K. Hermans, A.M. Prenen, O. Pierre-Louis, C.W. Bastiaansen, and D.J. Broer, *Fully reversible transition from Wenzel to Cassie− Baxter states on corrugated superhydrophobic surfaces.* Langmuir, 2009. **26**(5): p. 3335-3341.

177. Kusumaatmaja, H. and J. Yeomans, *Modeling contact angle hysteresis on chemically patterned and superhydrophobic surfaces.* Langmuir, 2007. **23**(11): p. 6019-6032.

178. Kusumaatmaja, H., R. Vrancken, C. Bastiaansen, and J. Yeomans, *Anisotropic drop morphologies on corrugated surfaces.* Langmuir, 2008. **24**(14): p. 7299-7308.

179. Hyväluoma, J. and J. Timonen, *Impact states and energy dissipation in bouncing and non-bouncing droplets.* Journal of Statistical Mechanics: Theory and Experiment, 2009. **2009**(06): p. P06010.

180. Huang, J.J., C. Shu, and Y.T. Chew, *Lattice Boltzmann study of droplet motion inside a grooved channel.* Physics of Fluids (1994-present), 2009. **21**(2): p. 022103.

181. Zhang, J. and D.Y. Kwok, *Contact line and contact angle dynamics in superhydrophobic channels.* Langmuir, 2006. **22**(11): p. 4998-5004.

182. Pearce, J., A. Giustini, R. Stigliano, and P. Jack Hoopes, *Magnetic Heating of Nanoparticles: The Importance of Particle Clustering to Achieve Therapeutic Temperatures.* J Nanotechnol Eng Med, 2013. **4**(1): p. 110071-1100714.

183. Briant, A.J., A.J. Wagner, and J.M. Yeomans, *Lattice Boltzmann simulations of contact line motion. I. Liquid-gas systems.* Phys Rev E Stat Nonlin Soft Matter Phys, 2004. **69**(3 Pt 1): p. 031602.

184. Briant, A.J. and J.M. Yeomans, *Lattice Boltzmann simulations of contact line motion. II. Binary fluids.* Phys Rev E Stat Nonlin Soft Matter Phys, 2004. **69**(3 Pt 1): p. 031603.

185. Inamuro, T., T. Ogata, S. Tajima, and N. Konishi, *A lattice Boltzmann method for incompressible two-phase flows with large density differences.* Journal of Computational Physics, 2004. **198**(2): p. 628-644.

186. Zu, Y.Q. and Y.Y. Yan, *Lattice Boltzmann method for modelling droplets on chemically heterogeneous and microstructured surfaces with large liquid-gas density ratio.* IMA Journal of Applied Mathematics, 2011. **76**(5): p. 743-760.

187. Kim, Y.H., W. Choi, and J.S. Lee, *Water droplet properties on periodically structured superhydrophobic surfaces: a lattice Boltzmann approach to multiphase flows with high water/air density ratio.* Microfluidics and Nanofluidics, 2010. **10**(1): p. 173-185.

188. Tanaka, Y., Y. Washio, M. Yoshino, and T. Hirata, *Numerical simulation of dynamic behavior of droplet on solid surface by the two-phase lattice Boltzmann method.* Computers & Fluids, 2011. **40**(1): p. 68-78.

189. Zu, Y., Y. Yan, J. Li, and Z. Han, *Wetting behaviours of a single droplet on biomimetic micro structured surfaces.* Journal of Bionic Engineering, 2010. **7**(2): p. 191-198.

190. Yoshimitsu, Z., A. Nakajima, T. Watanabe, and K. Hashimoto, *Effects of surface structure on the hydrophobicity and sliding behavior of water droplets.* Langmuir, 2002. **18**(15): p. 5818-5822.

191. Liu, G., L. Fu, A.V. Rode, and V.S. Craig, *Water droplet motion control on superhydrophobic surfaces: exploiting the Wenzel-to-Cassie transition.* Langmuir, 2011. **27**(6): p. 2595-2600.

192. Im, M., H. Im, J.-H. Lee, J.-B. Yoon, and Y.-K. Choi, *A robust superhydrophobic and superoleophobic surface with inverse-trapezoidal microstructures on a large transparent flexible substrate.* Soft Matter, 2010. **6**(7): p. 1401-1404.

193. Cai, T.-m., Z.-h. Jia, H.-n. Yang, and G. Wang, *Investigation of Cassie-Wenzel Wetting transitions on microstructured surfaces.* Colloid and Polymer Science, 2016. **294**(5): p. 833-840.

194. Liu, T.L. and C.J. Kim, *Repellent surfaces. Turning a surface superrepellent even to completely wetting liquids.* Science, 2014. **346**(6213): p. 1096-100.

195. Cahn, J.W., *Critical point wetting.* The Journal of Chemical Physics, 1977. **66**(8): p. 3667-3672.

196. Yan, Y.Y., N. Gao, and W. Barthlott, *Mimicking natural superhydrophobic surfaces and grasping the wetting process: a review on recent progress in preparing superhydrophobic surfaces.* Adv Colloid Interface Sci, 2011. **169**(2): p. 80-105.

197. Patankar, N.A., *Consolidation of hydrophobic transition criteria by using an approximate energy minimization approach.* Langmuir, 2010. **26**(11): p. 8941-5.

198. He, B., N.A. Patankar, and J. Lee, *Multiple equilibrium droplet shapes and design criterion for rough hydrophobic surfaces.* Langmuir, 2003. **19**(12): p. 4999-5003.

199. Whyman, G. and E. Bormashenko, *How to make the Cassie wetting state stable?* Langmuir, 2011. **27**(13): p. 8171-6.

200. Liu, S., Y. Yan, and Y. Gao, *Optimization of geometry parameters with separation efficiency and flow split ratio for downhole oil-water hydrocyclone.* Thermal Science and Engineering Progress, 2018. **8**: p. 370-374.

201. Lu, Y., Z. Li, G. Hailu, D. Xu, H. Wu, and W. Kang, *Study on the oil/water separation performance of a super-hydrophobic copper mesh under downhole*

conditions. Journal of Industrial and Engineering Chemistry, 2019. **72**: p. 310-318.

202. Peachey, B. and C. Matthews, *Downhole oil/water separator development.* Journal of Canadian Petroleum Technology, 1994. **33**(07).

203. Stuebinger, L. and G. Elphingstone Jr, *Multipurpose wells: downhole oil/water separation in the future.* SPE production & Facilities, 2000. **15**(03): p. 191-195.

204. Bybee, K., *A review of downhole separation technology.* Journal of petroleum technology, 2005. **57**(09): p. 48-50.

205. Amini, S., D. Mowla, M. Golkar, and F. Esmaeilzadeh, *Mathematical modelling of a hydrocyclone for the down-hole oil–water separation (DOWS).* Chemical Engineering Research and Design, 2012. **90**(12): p. 2186-2195.

206. Choi, M. *Hydrocyclone produced water treatment for offshore developments*. in *SPE Annual Technical Conference and Exhibition*. 1990. Society of Petroleum Engineers.

207. Bai, Z.-s., H.-l. Wang, and S.-T. Tu, *Oil–water separation using hydrocyclones enhanced by air bubbles.* Chemical Engineering Research and Design, 2011. **89**(1): p. 55-59.

208. Bangash, Y.K. and M. Reyna. *Downhole Oil Water Separation (DOWS) Systems in High-Volume/High HP Application*. in *SPE Latin American and Caribbean Petroleum Engineering Conference*. 2003. Society of Petroleum Engineers.

209. Zu, Y.Q. and Y.Y. Yan, *A numerical investigation of electrohydrodynamic (EHD) effects on bubble deformation under pseudo-nucleate boiling conditions.* International Journal of Heat and Fluid Flow, 2009. **30**(4): p. 761-767.

210. Zhou, N., Y. Gao, W. An, and M. Yang, *Investigation of velocity field and oil distribution in an oil–water hydrocyclone using a particle dynamics analyzer.* Chemical Engineering Journal, 2010. **157**(1): p. 73-79.

211. Liu, Y., Q. Yang, P. Qian, and H.-l. Wang, *Experimental study of circulation flow in a light dispersion hydrocyclone.* Separation and Purification Technology, 2014. **137**: p. 66-73.

212. Cheng, P., X. Quan, S. Gong, L. Dong, and F. Hong. *Recent studies on surface roughness and wettability effects in pool boiling*. in *International Heat Transfer Conference Digital Library*. 2014. Begel House Inc.

213. Dhir, V.K., G.R. Warrier, and E. Aktinol, *Numerical simulation of pool boiling: a review.* Journal of Heat Transfer, 2013. **135**(6): p. 061502.

214. Kunugi, T., *Brief review of latest direct numerical simulation on pool and film boiling.* Nuclear Engineering and Technology, 2012. **44**(8): p. 847-854.

215. Zhang, R. and H. Chen, *Lattice Boltzmann method for simulations of liquid-vapor thermal flows.* Physical Review E, 2003. **67**(6): p. 066711.

216. Hazi, G. and A. Markus, *On the bubble departure diameter and release frequency based on numerical simulation results.* International Journal of Heat and Mass Transfer, 2009. **52**(5): p. 1472-1480.

217. Markus, A. and G. Hazi, *Simulation of evaporation by an extension of the pseudopotential lattice Boltzmann method: a quantitative analysis.* Phys Rev E Stat Nonlin Soft Matter Phys, 2011. **83**(4 Pt 2): p. 046705.

218. Biferale, L., P. Perlekar, M. Sbragaglia, and F. Toschi, *Convection in multiphase fluid flows using lattice Boltzmann methods.* Physical Review Letters, 2012. **108**(10): p. 104502.

219. Gong, S. and P. Cheng, *A lattice Boltzmann method for simulation of liquid–vapor phase-change heat transfer.* International Journal of Heat and Mass Transfer, 2012. **55**(17-18): p. 4923-4927.

220. Gong, S. and P. Cheng, *Lattice Boltzmann simulation of periodic bubble nucleation, growth and departure from a heated surface in pool boiling.* International Journal of Heat and Mass Transfer, 2013. **64**: p. 122-132.

221. Gong, S., P. Cheng, and X. Quan, *Two-dimensional mesoscale simulations of saturated pool boiling from rough surfaces. Part I: Bubble nucleation in a single cavity at low superheats.* International Journal of Heat and Mass Transfer, 2016. **100**: p. 927-937.

222. Gong, S. and P. Cheng, *Two-dimensional mesoscale simulations of saturated pool boiling from rough surfaces. Part II: Bubble interactions above multi-cavities.* International Journal of Heat and Mass Transfer, 2016. **100**: p. 938-948.

223. Liu, X. and P. Cheng, *Lattice Boltzmann simulation of steady laminar film condensation on a vertical hydrophilic subcooled flat plate.* International Journal of Heat and Mass Transfer, 2013. **62**: p. 507-514.

224. Li, Q. and K. Luo, *Effect of the forcing term in the pseudopotential lattice Boltzmann modeling of thermal flows.* Physical Review E, 2014. **89**(5): p. 053022.

225. Li, Q., Q. Kang, M.M. Francois, Y. He, and K. Luo, *Lattice Boltzmann modeling of boiling heat transfer: the boiling curve and the effects of wettability.* International Journal of Heat and Mass Transfer, 2015. **85**: p. 787-796.

226. Li, Q., P. Zhou, and H.J. Yan, *Improved thermal lattice Boltzmann model for simulation of liquid-vapor phase change.* Phys Rev E, 2017. **96**(6-1): p. 063303.

227. Gong, S. and P. Cheng, *Direct numerical simulations of pool boiling curves including heater's thermal responses and the effect of vapor phase's thermal conductivity.* International Communications in Heat and Mass Transfer, 2017. **87**: p. 61-71.

228. Gong, W., S. Chen, and Y. Yan, *A thermal immiscible multiphase flow simulation by lattice Boltzmann method.* International Communications in Heat and Mass Transfer, 2017. **88**: p. 136-138.

229. Zhang, L., T. Wang, Y. Jiang, S. Kim, and C. Guo, *A study of boiling on surfaces with temperature-dependent wettability by lattice Boltzmann method.* International Journal of Heat and Mass Transfer, 2018. **122**: p. 775-784.

230. Dong, Z., W. Li, and Y. Song, *Lattice Boltzmann simulation of growth and deformation for a rising vapor bubble through superheated liquid.* Numerical Heat Transfer, Part A: Applications, 2009. **55**(4): p. 381-400.

231. Zheng, H.W., C. Shu, and Y.T. Chew, *A lattice Boltzmann model for multiphase flows with large density ratio.* Journal of Computational Physics, 2006. **218**(1): p. 353-371.

232. Sun, T. and W. Li, *Three-dimensional numerical simulation of nucleate boiling bubble by lattice Boltzmann method.* Computers & Fluids, 2013. **88**: p. 400-409.

233. Tanaka, Y., M. Yoshino, and T. Hirata, *Lattice Boltzmann simulation of nucleate pool boiling in saturated liquid.* Communications in Computational Physics, 2011. **9**(5): p. 1347-1361.

234. Sattari, E., M. Delavar, E. Fattahi, and K. Sedighi, *Numerical investigation the effects of working parameters on nucleate pool boiling.* International Communications in Heat and Mass Transfer, 2014. **59**: p. 106-113.

235. Begmohammadi, A., M. Farhadzadeh, and M.H. Rahimian, *Simulation of pool boiling and periodic bubble release at high density ratio using lattice Boltzmann method.* International Communications in Heat and Mass Transfer, 2015. **61**: p. 78-87.

236. Safari, H., M.H. Rahimian, and M. Krafczyk, *Extended lattice Boltzmann method for numerical simulation of thermal phase change in two-phase fluid flow.* Physical Review E, 2013. **88**(1): p. 013304.

237. Begmohammadi, A., M. Rahimian, M. Farhadzadeh, and M.A. Hatani, *Numerical simulation of single-and multi-mode film boiling using lattice Boltzmann method.* Computers & Mathematics with Applications, 2016. **71**(9): p. 1861-1874.

238. Sadeghi, R., M.S. Shadloo, M.Y.A. Jamalabadi, and A. Karimipour, *A three-dimensional lattice Boltzmann model for numerical investigation of bubble growth in pool boiling.* International Communications in Heat and Mass Transfer, 2016. **79**: p. 58-66.

239. Lallemand, P. and L.-S. Luo, *Theory of the lattice Boltzmann method: Dispersion, dissipation, isotropy, Galilean invariance, and stability.* Physical Review E, 2000. **61**(6): p. 6546.

240. Li, Q., Q.J. Kang, M.M. Francois, Y.L. He, and K.H. Luo, *Lattice Boltzmann modeling of boiling heat transfer: The boiling curve and the effects of wettability.* International Journal of Heat and Mass Transfer, 2015. **85**: p. 787-796.

241. Liu, H., A.J. Valocchi, Y. Zhang, and Q. Kang, *Phase-field-based lattice Boltzmann finite-difference model for simulating thermocapillary flows.* Physical Review E, 2013. **87**(1): p. 013010.

242. Parola, A., D. Pini, and L. Reatto, *Liquid-vapor transition from a microscopic theory: Beyond the Maxwell construction.* Physical review letters, 2008. **100**(16): p. 165704.

243. Law, C.K., *Recent advances in droplet vaporization and combustion.* Progress in energy and combustion science, 1982. **8**(3): p. 171-201.

244. Nishiwaki, N. *Kinetics of liquid combustion processes: evaporation and ignition lag of fuel droplets*. in *Symposium (International) on Combustion*. 1955. Elsevier.

245. Fei, L. and K.H. Luo, *Consistent forcing scheme in the cascaded lattice Boltzmann method.* Physical Review E, 2017. **96**(5): p. 053307.

246. Gong, W., Y. Zu, S. Chen, and Y. Yan, *Wetting transition energy curves for a droplet on a square-post patterned surface.* Science Bulletin, 2017. **62**(2): p. 136-142.

247. Chen, L., Q. Kang, Y. Mu, Y.-L. He, and W.-Q. Tao, *A critical review of the pseudopotential multiphase lattice Boltzmann model: Methods and applications.* International Journal of Heat and Mass Transfer, 2014. **76**: p. 210-236.

248. Fei, L., K.H. Luo, C. Lin, and Q. Li, *Modeling incompressible thermal flows using a central-moments-based lattice Boltzmann method.* International Journal of Heat and Mass Transfer, 2018. **120**: p. 624-634.

249. Zhang, Y.-H., X. Gu, R. Barber, and D. Emerson, *Modelling thermal flow in the transition regime using a lattice Boltzmann approach.* EPL (Europhysics Letters), 2007. **77**(3): p. 30003.

250. Gong, W., Y. Yan, S. Chen, and D. Giddings, *Numerical Study of Wetting Transitions on Biomimetic Surfaces Using a Lattice Boltzmann Approach with Large Density Ratio.* Journal of Bionic Engineering, 2017. **14**(3): p. 486-496.

251. Van der Waals, J.D., *Over de Continuiteit van den Gas-en Vloeistoftoestand*. Vol. 1. 1873: Sijthoff.

252. Carnahan, N.F. and K.E. Starling, *Equation of state for nonattracting rigid spheres.* The Journal of chemical physics, 1969. **51**(2): p. 635-636.

253. Yuan, P. and L. Schaefer, *Equations of state in a lattice Boltzmann model.* Physics of Fluids, 2006. **18**(4): p. 042101.

254. He, X. and G.D. Doolen, *Thermodynamic foundations of kinetic theory and lattice Boltzmann models for multiphase flows.* Journal of Statistical Physics, 2002. **107**(1-2): p. 309-328.

255. Khajepor, S., J. Wen, and B. Chen, *Multipseudopotential interaction: A solution for thermodynamic inconsistency in pseudopotential lattice Boltzmann models.* Physical Review E, 2015. **91**(2): p. 023301.

256. Xu, A., T. Zhao, L. An, and L. Shi, *A three-dimensional pseudo-potential-based lattice Boltzmann model for multiphase flows with large density ratio and variable surface tension.* International Journal of Heat and Fluid Flow, 2015. **56**: p. 261-271.

257. Chibbaro, S., G. Falcucci, G. Chiatti, H. Chen, X. Shan, and S. Succi, *Lattice Boltzmann models for nonideal fluids with arrested phase-separation.* Physical Review E, 2008. **77**(3): p. 036705.

258. Kupershtokh, A., D. Medvedev, and D. Karpov, *On equations of state in a lattice Boltzmann method*. Computers & Mathematics with Applications, 2009. **58**(5): p. 965-974.

259. Yu, Y., Z.X. Wen, Q. Li, P. Zhou, and H.J. Yan, *Boiling heat transfer on hydrophilic-hydrophobic mixed surfaces: A 3D lattice Boltzmann study*. Applied Thermal Engineering, 2018. **142**: p. 846-854.

260. Liu, X. and P. Cheng, *3D multiphase lattice Boltzmann simulations for morphological effects on self-propelled jumping of droplets on textured superhydrophobic surfaces.* International Communications in Heat and Mass Transfer, 2015. **64**: p. 7-13.

261. Huang, H., M. Sukop, and X. Lu, *Multiphase lattice Boltzmann methods: Theory and application*. 2015: John Wiley & Sons.

262. Sehgal, B., R. Nourgaliev, and T. Dinh, *Numerical simulation of droplet deformation and break-up by lattice-Boltzmann method.* Progress in Nuclear Energy, 1999. **34**(4): p. 471-488.

263. Nekovee, M., P.V. Coveney, H. Chen, and B.M. Boghosian, *Lattice-Boltzmann model for interacting amphiphilic fluids.* Physical Review E, 2000. **62**(6): p. 8282.

264. Dörfler, F., M. Rauscher, J. Koplik, J. Harting, and S. Dietrich, *Micro-and nanoscale fluid flow on chemical channels.* Soft Matter, 2012. **8**(35): p. 9221-9234.

265. Gupta, A. and R. Kumar, *Lattice Boltzmann simulation to study multiple bubble dynamics.* International Journal of Heat and Mass Transfer, 2008. **51**(21-22): p. 5192-5203.

266. Yu, Z., H. Yang, and L.-S. Fan, *Numerical simulation of bubble interactions using an adaptive lattice Boltzmann method.* Chemical Engineering Science, 2011. **66**(14): p. 3441-3451.

267. Zhang, Q., D. Sun, Y. Zhang, and M. Zhu, *Lattice Boltzmann modeling of droplet condensation on superhydrophobic nanoarrays.* Langmuir, 2014. **30**(42): p. 12559-12569.

268. Zhao, H., Z. Ning, Q. Kang, L. Chen, and T. Zhao, *Relative permeability of two immiscible fluids flowing through porous media determined by lattice Boltzmann method.* International Communications in Heat and Mass Transfer, 2017. **85**: p. 53-61.

269. Gong, S. and P. Cheng, *Numerical investigation of droplet motion and coalescence by an improved lattice Boltzmann model for phase transitions and multiphase flows.* Computers & Fluids, 2012. **53**: p. 93-104.

270. Li, Q., K. Luo, and X. Li, *Lattice Boltzmann modeling of multiphase flows at large density ratio with an improved pseudopotential model.* Physical Review E, 2013. **87**(5): p. 053301.

271. McNaught, A.D. and A.D. McNaught, *Compendium of chemical terminology*. Vol. 1669. 1997: Blackwell Science Oxford.

272. Ratke, L. and P.W. Voorhees, *Growth and coarsening: Ostwald ripening in material processing*. 2013: Springer Science & Business Media.

273. Gottlieb, S. and C.-W. Shu, *Total variation diminishing Runge-Kutta schemes.* Mathematics of computation of the American Mathematical Society, 1998. **67**(221): p. 73-85.

Appendix: MATLAB programs

For wetting transitions

```
%%%%%%%%%%%%%%%%%%%%%%%%%%%%%%%%%%%%%%%%%%%%%%%%%%%%%%%%%%%%%%%%%%%%%%%%
wetting.m: Lattice Boltzmann method for modelling droplets on
chemically heterogeneous and microstructured surfaces with large
liquid-gas density ratio
%%%%%%%%%%%%%%%%%%%%%%%%%%%%%%%%%%%%%%%%%%%%%%%%%%%%%%%%%%%%%%%%%%%%%%%%

% Lattice Boltzmann sample in Matlab
% Copyright Wei Gong
% Address: Nottingham NG7 2RD, UK
% E-mail: ezxwg@nottingham.ac.uk

clear, clc

format long;

% global variables
global cycle ep;

maxT  = 200000000; % maximum number of timesteps
Tstep = 100;       % to output computatinal results per 100 timesteps
ep    = 1e-6;      % criterion for determining convergence of velocity
                   % correction
constant;          % constant setting
initialization;    % initial condition setting
equ_fg;            % initialize the distribution functions
f = fn;
g = gn;

for cycle = 0:maxT
    col_fg;                             % collision
    for i = 1:15
        f(i, :, :, :) = ...             % streaming
            circshift(fn(i, :, :, :), [0, ea(1, i), ea(2, i), ea(3,
i)]);
        g(i, :, :, :) = ...             % streaming
            circshift(gn(i, :, :, :), [0, ea(1, i), ea(2, i), ea(3,
i)]);
    end
    f = bounback(f);                    % modified bounce back
    f = peri_b4(f);                    % free flow boundary conditions
    g = peri_b4(g);
% visualization
    if (mod(cycle, Tstep) == 0)
        save(['cyc', num2str(cycle)], 'f', 'g', 'p');
        rhoPlot = reshape(rho(:, ny, :), nx, nz);
        uxPlot   = reshape(ux(:, ny, :), nx, nz);
        uzPlot   = reshape(uz(:, ny, :), nx, nz);
        pPlot   = reshape(p(:, ny, :), nx, nz);
        subplot(2, 2, 1);
        imagesc(flipud(rhoPlot'));
        colorbar
```

```
        title('Density');
        axis equal off; drawnow
        subplot(2, 2, 2);
        quiver(x, z, uxPlot, uzPlot);
        colorbar
        title('Velocity');
        axis equal off; drawnow
        subplot(2, 2, 3);
        imagesc(flipud(pPlot'));
        colorbar
        title('Pressure');
        axis equal off; drawnow
    end
end

%%%%%%%%%%%%%%%%%%%%%%%%%%%%%%%%%%%%%%%%%%%%%%%%%%%%%%%%%%%%%%%%%%%%%%%%%%%%
constant.m: consant setting
%%%%%%%%%%%%%%%%%%%%%%%%%%%%%%%%%%%%%%%%%%%%%%%%%%%%%%%%%%%%%%%%%%%%%%%%%%%%

% global variables
global nx ny nz nxyz sx sy bwx bwy bx by bh phi_l phi_g rho_l rho_g ...
    mu_l mu_g rho wa ea p;

% D3Q19 lattice constants
nx    = 37;         % x length of computational domain
ny    = 37;         % y length of computational domain
nz    = 75;         % z length of computational domain
nxyz = nx*ny*nz;
% Ta_f  = 1;         % dimensionless relaxation time of order parameter
% Ta_g  = 1;           % dimensionless relaxation time of velocity
Ha  = [1 0 0 0 0 0 0 0 0 0 0 0 0 0 0 ];      %H_alpha
wa  = [2/9 1/9 1/9 1/9 1/9 1/9 1/9 1/72 1/72 1/72 1/72 1/72 1/72 1/72 ...
       1/72 1/72];                           %omega_alpha
Fa  = [-7/3 1/3 1/3 1/3 1/3 1/3 1/3 1/24 1/24 1/24 1/24 1/24 1/24 1/24 ...
       1/24 1/24];                           %F_alpha
ea  = [0 1 0 0 -1 0 0 1 -1 1 1 -1 1 -1 -1;   %e_alpha
       0 0 1 0 0 -1 0 1 1 -1 1 -1 -1 1 -1;
       0 0 0 1 0 0 -1 1 1 1 -1 -1 -1 -1 1];

%parameters for grid distribution on micro post
sx  = 4;          %start x position of micro post
sy  = 4;          %start y position of micro post
bwx = 10;         %distance between two posts in x direction
bwy = 10;         %distance between two posts in y direction
bx  = 5;          %length of post in x direction
by  = 5;          %length of post in y direction
bh  = 5;          %length of post in z direction

% General flow constants
% reference length scale: 1e-6m
% reference time scale: 1e-8s
% reference mass scale: 1e-18kg
k_f   = 0.05;     % k, surface tension parameter
rho_l = 1000;     % dimensionless density of bulk liquid phase
rho_g = 1.29;     % dimensionless density of bulk gas phase
phi_l = 0.4;      % order parameter of bulk liquid phase
phi_g = 0.1;      % order parameter of bulk gas phase
mu_l  = 10;       % dimensionless dynamic viscosity of liquid phase
mu_g  = 1.935e-1;% dimensionless dynamic viscosity of gas phase
Di    = 60;           % diameter of the droplet
```

```
th    = 3;            % initial thickness of the liquid-gas interface
Rin   = (Di - th)/2;  % initial inner radius of the droplet
Rout  = (Di + th)/2;  % initial outer radius of the droplet
uinz   = -1e-5; % initial dimensionless velocity of droplet in z
deriction
theta_Y = 130*pi/180;                                    % Young's angle
gamma   = acos((sin(theta_Y))^2);                        % gamma
Omega      =  -2*sqrt(cos(gamma/3)*(1  -  cos(gamma/3))); %  wetting
potential
lambda  = -Omega*k_f*(phi_l - phi_g)/th;           % parameter related
to
                                                         % Omega
beta    = 8*k_f/((phi_l - phi_g)^2*th^2);          % constant relating
to
                                                           %    interfacial
thickness
sigma_lg = k_f*2/3*(phi_l - phi_g)^2/th; % initial surface tension
ga       = 9.8e-10; % dimensionless gravitational acceleration
crx      = nx - 0.5;    % x coodinate of droplet centre
cry      = ny - 0.5;    % y coodinate of droplet centre
crz      = 40;      % z coodinate of droplet centre
phi  = zeros(nx, ny, nz);     % order parameter
rho  = zeros(nx, ny, nz);     % density
mu   = zeros(nx, ny, nz);     % viscosity
ux   = zeros(nx, ny, nz);     % x velocity
uy   = zeros(nx, ny, nz);     % y velocity
fn   = zeros(15, nx, ny, nz); % f distribution function
gn   = zeros(15, nx, ny, nz); % g distribution function
f    = zeros(15, nx, ny, nz);
g    = zeros(15, nx, ny, nz);

R_sq = zeros(nx, ny, nz);
x    = zeros(nx, ny, nz);
y    = zeros(nx, ny, nz);
z    = zeros(nx, ny, nz);
d1_phi  = zeros(3, nx, ny, nz);
d2_phi  = zeros(nx, ny, nz);
rhoPlot = zeros(nx, nz);
uPlot   = zeros(nx, nz);
p       = zeros(nx, ny, nz);

%%%%%%%%%%%%%%%%%%%%%%%%%%%%%%%%%%%%%%%%%%%%%%%%%%%%%%%%%%%%%%%%%%%%%%%%
initialization.m: initial condition setting
%%%%%%%%%%%%%%%%%%%%%%%%%%%%%%%%%%%%%%%%%%%%%%%%%%%%%%%%%%%%%%%%%%%%%%%%

% global variables
global xxs yys solid solids xr xl yf yb;

%initialize the distribution of order parameter and velocity
[x, y, z]  = ...     % get coordinate of matrix indices
                    meshgrid(1:nx, 1:ny, 1:nz);
R_sq       = (x - crx).^2 + (y - cry).^2 + (z - crz).^2;

phi        = (phi_l + phi_g)/2 + (phi_g - phi_l)/2.* ...
    sin(pi.*((sqrt(R_sq) - Rin)./(Rout - Rin) - 0.5));
uz         = uinz/2 - uinz/2.* ...
    sin(pi.*((sqrt(R_sq) - Rin)./(Rout - Rin) - 0.5));

ini_droplet_inner        = ... % initial location of the inner droplet
                           R_sq < Rin^2;
```

```
phi(ini_droplet_inner)    = phi_l;
uz(ini_droplet_inner)     = uinz;

ini_droplet_outer        = ... % initial location of the outer droplet
                             R_sq > Rout^2;
phi(ini_droplet_outer)    = phi_g;
uz(ini_droplet_outer)     = 0;


%initialize the distribution of density
rho = (phi - phi_g)./(phi_l - phi_g).*(rho_l - rho_g) + rho_g;

%initialize the distribution of viscosity
mu = (rho - rho_g)./(rho_l - rho_g).*(mu_l - mu_g) + mu_g;

%find the solid boundary
xx = ... % x coordinate of micro posts
    [4:9 14:19 24:29 34:36];
yy = ... % y coordinate of micro posts
    [4:9 14:19 24:29 34:36];
xxs = ...% x coordinate of micro posts inner points
    [5:8 15:18 25:28 35:36];
yys = ...% y coordinate of micro posts inner points
    [5:8 15:18 25:28 35:36];
xr  = (sx + bx):bwx:nx;      % x right coordinates
xl  = sx:bwx:nx;             % x left coordinates
yb  = (sy + by):bwy:ny;      % y back coordinates
yf  = sy:bwy:ny;             % y front coordinates

solid = (z <= bh + 1) & (ismember(x, xx)) & (ismember(y, yy));
solid(:, :, 1) = 1;
solids = (z > 1) & (z <= bh + 1) & (ismember(x, xx)) & (ismember(y,
yy));
clear xx yy R_sq Di Rin Rout uinz crx cry crz x y z ...
    ini_droplet_interface ini_droplet_inner ini_droplet_outer;

[z, x]  = meshgrid(1:nz, 1:nx);

%%%%%%%%%%%%%%%%%%%%%%%%%%%%%%%%%%%%%%%%%%%%%%%%%%%%%%%%%%%%%%%%%%%%%%%
equ_fg.m: calculate equilibrium states of distribution functions
%%%%%%%%%%%%%%%%%%%%%%%%%%%%%%%%%%%%%%%%%%%%%%%%%%%%%%%%%%%%%%%%%%%%%%%

% the first order of partial derivative of phi
d1_phi = zeros(3, nx, ny, nz);          % all points
d1_phi(1, :, :, :) = fst_partd(1, phi); % x
d1_phi(2, :, :, :) = fst_partd(2, phi); % y
d1_phi(3, :, :, :) = fst_partd(3, phi); % z

d1_phi(3, 2:(nx - 1), 2:(ny - 1), 1) = lambda/k_f;  % z = 1
d1_phi(3, 2:(nx - 1), 2:(ny - 1), 3) = ...          % z = 3
    (3*phi(2:(nx - 1), 2:(ny - 1), 3) - ...
    4*phi(2:(nx - 1), 2:(ny - 1), 2) + ...
    phi(2:(nx - 1), 2:(ny - 1), 1))/2;

% treatment of wetting boundaries on the micro-post paterned surface
d1_phi(3, xr, yys, 1) = ...                         % right-down line
    lambda/k_f/sqrt(2);
d1_phi(1, xr, yys, 1) = ...
    lambda/k_f/sqrt(2);
```

```
d1_phi(3, xr, yys, 3) = ...
    (3*phi(xr, yys, 3) - ...
    4*phi(xr, yys, 2) + ...
    phi(xr, yys, 1))/2;
d1_phi(1, xr + 2, yys, 1) = ...
    (3*phi(xr + 2, yys, 1) - ...
    4*phi(xr + 1, yys, 1) + ...
    phi(xr, yys, 1))/2;

d1_phi(3, xxs, yb, 1) = ...                          % back-down line
    lambda/k_f/sqrt(2);
d1_phi(2, xxs, yb, 1) = ...
    lambda/k_f/sqrt(2);
d1_phi(3, xxs, yb, 3) = ...
    (3*phi(xxs, yb, 3) - ...
    4*phi(xxs, yb, 2) + ...
    phi(xxs, yb, 1))/2;
d1_phi(2, xxs, yb + 2, 1) = ...
    (3*phi(xxs, yb + 2, 1) - ...
    4*phi(xxs, yb + 1, 1) + ...
    phi(xxs, yb, 1))/2;

d1_phi(3, xl, yys, 1) = ...                          % left-down line
    lambda/k_f/sqrt(2);
d1_phi(1, xl, yys, 1) = ...
    -lambda/k_f/sqrt(2);
d1_phi(3, xl, yys, 3) = ...
    (3*phi(xl, yys, 3) - ...
    4*phi(xl, yys, 2) + ...
    phi(xl, yys, 1))/2;
d1_phi(1, xl - 2, yys, 1) = ...
    -(3*phi(xl - 2, yys, 1) - ...
    4*phi(xl - 1, yys, 1) + ...
    phi(xl, yys, 1))/2;

d1_phi(3, xxs, yf, 1) = ...                          % front-down line
    lambda/k_f/sqrt(2);
d1_phi(2, xxs, yf, 1) = ...
    -lambda/k_f/sqrt(2);
d1_phi(3, xxs, yf, 3) = ...
    (3*phi(xxs, yf, 3) - ...
    4*phi(xxs, yf, 2) + ...
    phi(xxs, yf, 1))/2;
d1_phi(2, xxs, yf - 2, 1) = ...
    -(3*phi(xxs, yf - 2, 1) - ...
    4*phi(xxs, yf - 1, 1) + ...
    phi(xxs, yf, 1))/2;

d1_phi(1, xr, yys, 2:bh) = ...                       % right surface
    lambda/k_f;
d1_phi(1, xr + 2, yys, 2:bh) = ...
    (3*phi(xr + 2, yys, 2:bh) - ...
    4*phi(xr + 1, yys, 2:bh) + ...
    phi(xr, yys, 2:bh))/2;

d1_phi(2, xxs, yb, 2:bh) = ...                       % back surface
    lambda/k_f;
d1_phi(2, xxs, yb + 2, 2:bh) = ...
    (3*phi(xxs, yb + 2, 2:bh) - ...
    4*phi(xxs, yb + 1, 2:bh) + ...
```

```
    phi(xxs, yb, 2:bh))/2;

d1_phi(1, xl, yys, 2:bh) = ...                          % left surface
    -lambda/k_f;
d1_phi(1, xl - 2, yys, 2:bh) = ...
    -(3*phi(xl - 2, yys, 2:bh) - ...
    4*phi(xl - 1, yys, 2:bh) + ...
    phi(xl, yys, 2:bh))/2;

d1_phi(2, xxs, yf, 2:bh) = ...                          % front surface
    -lambda/k_f;
d1_phi(2, xxs, yf - 2, 2:bh) = ...
    -(3*phi(xxs, yf - 2, 2:bh) - ...
    4*phi(xxs, yf - 1, 2:bh) + ...
    phi(xxs, yf, 2:bh))/2;

d1_phi(3, xxs, yys, bh + 1) = ...                       % up surface
    lambda/k_f;
d1_phi(3, xxs, yys, bh + 3) = ...
    (3*phi(xxs, yys, bh + 3) - ...
    4*phi(xxs, yys, bh + 2) + ...
    phi(xxs, yys, bh + 1))/2;

% the second order of partial derivative of phi
d2_phi = snd_partd(phi);                                % all points

d2_phi(2:(nx - 1), 2:(ny - 1), 1) = ...                 % bottom surface
    phi(3:nx, 2:(ny - 1), 1) - ...
    2*phi(2:(nx - 1), 2:(ny - 1), 1) + ...
    phi(1:(nx - 2), 2:(ny - 1), 1) + ...
    phi(2:(nx - 1), 3:ny, 1) - ...
    2*phi(2:(nx - 1), 2:(ny - 1), 1) + ...
    phi(2:(nx - 1), 1:(ny - 2), 1) + ...
    reshape((-3*d1_phi(3, 2:(nx - 1), 2:(ny - 1), 1) + ...
    4*d1_phi(3, 2:(nx - 1), 2:(ny - 1), 2) - ...
    d1_phi(3, 2:(nx - 1), 2:(ny - 1), 3)), length(2:(nx - 1)), ...
    length(2:(ny - 1)))/2;

d2_phi(xr, yys, 1) = ...                                % right-down line
    reshape((-3*d1_phi(1, xr, yys, 1) + ...
    4*d1_phi(1, xr + 1, yys, 1) - ...
    d1_phi(1, xr + 2, yys, 1)), length(xr), length(yys))/2 + ...
    phi(xr, yys + 1, 1) - ...
    2*phi(xr, yys, 1) + ...
    phi(xr, yys - 1, 1) + ...
    reshape((-3*d1_phi(3, xr, yys, 1) + ...
    4*d1_phi(3, xr, yys, 2) - ...
    d1_phi(3, xr, yys, 3)), length(xr), length(yys))/2;

d2_phi(xxs, yb, 1) = ...                                % back-down line
    reshape((-3*d1_phi(2, xxs, yb, 1) + ...
    4*d1_phi(2, xxs, yb + 1, 1) - ...
    d1_phi(2, xxs, yb + 2, 1)), length(xxs), length(yb))/2 + ...
    phi(xxs + 1, yb, 1) - ...
    2*phi(xxs, yb, 1) + ...
    phi(xxs - 1, yb, 1) + ...
    reshape((-3*d1_phi(3, xxs, yb, 1) + ...
    4*d1_phi(3, xxs, yb, 2) - ...
    d1_phi(3, xxs, yb, 3)), length(xxs), length(yb))/2;
```

```
d2_phi(xl, yys, 1) = ...                                % left-down line
    -reshape((-3*d1_phi(1, xl, yys, 1) + ...
    4*d1_phi(1, xl - 1, yys, 1) - ...
    d1_phi(1, xl - 2, yys, 1)), length(xl), length(yys))/2 + ...
    phi(xl, yys + 1, 1) - ...
    2*phi(xl, yys, 1) + ...
    phi(xl, yys - 1, 1) + ...
    reshape((-3*d1_phi(3, xl, yys, 1) + ...
    4*d1_phi(3, xl, yys, 2) - ...
    d1_phi(3, xl, yys, 3)), length(xl), length(yys))/2;

d2_phi(xxs, yf, 1) = ...                                % front-down line
    -reshape((-3*d1_phi(2, xxs, yf, 1) + ...
    4*d1_phi(2, xxs, yf - 1, 1) - ...
    d1_phi(2, xxs, yf - 2, 1)), length(xxs), ...
    length(yf))/2 + ...
    phi(xxs + 1, yf, 1) - ...
    2*phi(xxs, yf, 1) + ...
    phi(xxs - 1, yf, 1) + ...
    reshape((-3*d1_phi(3, xxs, yf, 1) + ...
    4*d1_phi(3, xxs, yf, 2) - ...
    d1_phi(3, xxs, yf, 3)), length(xxs), length(yf))/2;

d2_phi(xr, yys, 2:bh) = ...                             % right surface
    phi(xr, yys + 1, 2:bh) - ...
    2*phi(xr, yys, 2:bh) + ...
    phi(xr, yys - 1, 2:bh) + ...
    phi(xr, yys, 3:(bh + 1)) - ...
    2*phi(xr, yys, 2:bh) + ...
    phi(xr, yys, 1:(bh -1)) + ...
    reshape((-3*d1_phi(1, xr, yys, 2:bh) + ...
    4*d1_phi(1, xr + 1, yys, 2:bh) - ...
    d1_phi(1, xr + 2, yys, 2:bh)), ...
    length(xr), length(yys), length(2:bh))/2;

d2_phi(xxs, yb, 2:bh) = ...                             % back surface
    phi(xxs + 1, yb, 2:bh) - ...
    2*phi(xxs, yb, 2:bh) + ...
    phi(xxs - 1, yb, 2:bh) + ...
    phi(xxs, yb, 3:(bh + 1)) - ...
    2*phi(xxs, yb, 2:bh) + ...
    phi(xxs, yb, 1:(bh -1)) + ...
    reshape((-3*d1_phi(2, xxs, yb, 2:bh) + ...
    4*d1_phi(2, xxs, yb + 1, 2:bh) - ...
    d1_phi(2, xxs, yb + 2, 2:bh)), length(xxs), ...
    length(yb), length(2:bh))/2;

d2_phi(xl, yys, 2:bh) = ...                             % left surface
    phi(xl, yys + 1, 2:bh) - ...
    2*phi(xl, yys, 2:bh) + ...
    phi(xl, yys - 1, 2:bh) + ...
    phi(xl, yys, 3:(bh + 1)) - ...
    2*phi(xl, yys, 2:bh) + ...
    phi(xl, yys, 1:(bh - 1)) + ...
    -reshape((-3*d1_phi(1, xl, yys, 2:bh) + ...
    4*d1_phi(1, xl - 1, yys, 2:bh) - ...
    d1_phi(1, xl - 2, yys, 2:bh)), ...
    length(xl), length(yys), length(2:bh))/2;

d2_phi(xxs, yf, 2:bh) = ...                              % front surface
```

```
    phi(xxs + 1, yf, 2:bh) - ...
    2*phi(xxs, yf, 2:bh) + ...
    phi(xxs - 1, yf, 2:bh) + ...
    phi(xxs, yf, 3:(bh + 1)) - ...
    2*phi(xxs, yf, 2:bh) + ...
    phi(xxs, yf, 1:(bh -1)) + ...
    -reshape((-3*d1_phi(2, xxs, yf, 2:bh) + ...
    4*d1_phi(2, xxs, yf - 1, 2:bh) - ...
    d1_phi(2, xxs, yf - 2, 2:bh)), ...
    length(xxs), length(yf), length(2:bh))/2;

d2_phi(xxs, yys, bh + 1) = ...                          % up surface
    phi(xxs + 1, yys, bh + 1) - ...
    2*phi(xxs, yys, bh + 1) + ...
    phi(xxs - 1, yys, bh + 1) + ...
    phi(xxs, yys + 1, bh + 1) - ...
    2*phi(xxs, yys, bh + 1) + ...
    phi(xxs, yys - 1, bh + 1) + ...
    reshape((-3*d1_phi(3, xxs, yys, bh + 1) + ...
    4*d1_phi(3, xxs, yys, bh + 2) - ...
    d1_phi(3, xxs, yys, bh + 3)), length(xxs), length(yys))/2;

sGp = ...              % square of magnititude of d1_phi
    d1_phi(1,   :,   :,   :).^2   +   d1_phi(2,   :,   :,   :).^2   +
d1_phi(3, :, :, :).^2;
sGp = reshape(sGp, nx, ny, nz);
P0  = beta.*(phi - phi_l).*(phi - phi_g).* ...
    (3*phi.^2 - phi.*phi_l - phi.*phi_g - phi_l*phi_g) - ...
    k_f.*phi.*d2_phi - k_f/6.*sGp;

u11 = fst_partd(1, ux);  % deltau
u12 = fst_partd(2, ux);
u13 = fst_partd(3, ux);
u21 = fst_partd(1, uy);
u22 = fst_partd(2, uy);
u23 = fst_partd(3, uy);
u31 = fst_partd(1, uz);
u32 = fst_partd(2, uz);
u33 = fst_partd(3, uz);

uu11 = u11 + u11;              % deltau + udelta
uu12 = u12 + u21;
uu13 = u13 + u31;
uu21 = uu12;
uu22 = u22 + u22;
uu23 = u23 + u32;
uu31 = uu13;
uu32 = uu23;
uu33 = u33 + u33;

muuu11 = mu.*uu11;             % mu(deltau + udelta)
muuu12 = mu.*uu12;
muuu13 = mu.*uu13;
muuu21 = mu.*uu21;
muuu22 = mu.*uu22;
muuu23 = mu.*uu23;
muuu31 = mu.*uu31;
muuu32 = mu.*uu32;
muuu33 = mu.*uu33;
```

```
dmuuu1 = ...                    % delta_mu(deltau + udelta)
    fst_partd(1, muuu11) + fst_partd(2, muuu21) + fst_partd(3, muuu31);
dmuuu2 = ...
    fst_partd(1, muuu12) + fst_partd(2, muuu22) + fst_partd(3, muuu32);
dmuuu3 = ...
    fst_partd(1, muuu13) + fst_partd(2, muuu23) + fst_partd(3, muuu33);

Gp11 = 9/2* ...                 % G(phi)
    reshape(d1_phi(1, :, :, :).*d1_phi(1, :, :, :), nx, ny, nz) -
3/2.*sGp;
Gp12 = 9/2* ...
    reshape(d1_phi(1, :, :, :).*d1_phi(2, :, :, :), nx, ny, nz);
Gp13 = 9/2* ...
    reshape(d1_phi(1, :, :, :).*d1_phi(3, :, :, :), nx, ny, nz);
Gp21 = 9/2* ...
    reshape(d1_phi(2, :, :, :).*d1_phi(1, :, :, :), nx, ny, nz);
Gp22 = 9/2* ...
    reshape(d1_phi(2, :, :, :).*d1_phi(2, :, :, :), nx, ny, nz) -
3/2.*sGp;
Gp23 = 9/2* ...
    reshape(d1_phi(2, :, :, :).*d1_phi(3, :, :, :), nx, ny, nz);
Gp31 = 9/2* ...
    reshape(d1_phi(3, :, :, :).*d1_phi(1, :, :, :), nx, ny, nz);
Gp32 = 9/2* ...
    reshape(d1_phi(3, :, :, :).*d1_phi(2, :, :, :), nx, ny, nz);
Gp33 = 9/2* ...
    reshape(d1_phi(3, :, :, :).*d1_phi(3, :, :, :), nx, ny, nz) -
3/2.*sGp;

u_sqr = ux.^2 + uy.^2 + uz.^2; % u square
sGr = -2/3.*k_f./rho.*sGp;

for i = 1:15

    eau = ea(1, i).*ux + ea(2, i).*uy + ea(3, i).*uz;
    eaGpea = ...                % e_alpha times G_phi times e_alpha
        ea(1, i).*ea(1, i).*Gp11 + ea(1, i).*ea(2, i).*Gp12 + ...
        ea(1, i).*ea(3, i).*Gp13 + ea(2, i).*ea(1, i).*Gp21 + ...
        ea(2, i).*ea(2, i).*Gp22 + ea(2, i).*ea(3, i).*Gp23 + ...
        ea(3, i).*ea(1, i).*Gp31 + ea(3, i).*ea(2, i).*Gp32 + ...
        ea(3, i).*ea(3, i).*Gp33;
    eadu2ea = ...               % e_alpha times deltau2 times e_alpha
        ea(1, i).*ea(1, i).*uu11 + ea(1, i).*ea(2, i).*uu12 + ...
        ea(1, i).*ea(3, i).*uu13 + ea(2, i).*ea(1, i).*uu21 + ...
        ea(2, i).*ea(2, i).*uu22 + ea(2, i).*ea(3, i).*uu23 + ...
        ea(3, i).*ea(1, i).*uu31 + ea(3, i).*ea(2, i).*uu32 + ...
        ea(3, i).*ea(3, i).*uu33;

    fn(i, :, :, :) = ...        % f_eq
        Ha(i).*phi    +    Fa(i).*P0    +    3*wa(i).*phi.*eau    +
wa(i).*k_f.*eaGpea;

    gn(i, :, :, :) = ...        % g_eq
        wa(i).*(1 + 3.*eau + 9/2*eau.*eau - 3/2*u_sqr + 3/4*eadu2ea)
+ ...
        wa(i).*k_f./rho.*eaGpea + Fa(i).*sGr;

end

fn = peri_b4(fn);
```

```
gn = peri_b4(gn);

%%%%%%%%%%%%%%%%%%%%%%%%%%%%%%%%%%%%%%%%%%%%%%%%%%%%%%%%%%%%%%%%%%%%%%%%
col_fg.m: implement the collision step of the lattices
%%%%%%%%%%%%%%%%%%%%%%%%%%%%%%%%%%%%%%%%%%%%%%%%%%%%%%%%%%%%%%%%%%%%%%%%

% calculate order paremeter and velocity on the basis of distribution
% functions
phi = reshape(sum(f), nx, ny, nz);
phi(xxs, yys, 1:bh) = phi_g;
phi(:, :, nz - 1) = phi_g;
phi = peri_b3s(phi);

ux = reshape(ea(1, :)*reshape(g, 15, nxyz), nx, ny, nz);
uy = reshape(ea(2, :)*reshape(g, 15, nxyz), nx, ny, nz);
uz = reshape(ea(3, :)*reshape(g, 15, nxyz), nx, ny, nz);

ux(solid) = 0;
uy(solid) = 0;
uz(solid) = 0;

ux = peri_b3vx(ux);
uy = peri_b3vy(uy);
uz = peri_b3vz(uz);

% update the value of density and viscosity
[rho, mu] = cal_rhomu(phi);

clear d1_phi d2_phi dmuuea dmuuu1 dmuuu2 dmuuu3 eadu2ea eaGpea eau
F ...
    Gp11 Gp12 Gp13 Gp21 Gp22 Gp23 Gp31 Gp32 Gp33 muuu11 muuu12
muuu13 ...
    muuu21 muuu22 muuu23 muuu31 muuu32 muuu33 sGp sGr u11 u12 u13
u21 ...
    u22 u23 u31 u32 u33 u_sqr uu11 uu12 uu13 uu21 uu22 uu23 uu31
uu32 ...
    uu33;

% iteration for velocity correction
[ux, uy, uz] = iter_u(ux, uy, uz);

equ_fg;

for i = 1:15

    dmuuea = ...                % delta_mu(deltau + udelta)_ea
        dmuuu1*ea(1, i) + dmuuu2*ea(2, i) + dmuuu3*ea(3, i);
    F = -3*wa(i)*ea(3, i)*ga.*(1 - rho_g./rho);
    F(:, :, 1) = 0;

    gn(i, :, :, :) = ...        % g_eq
       reshape(gn(i, :, :, :), nx, ny, nz) + 3*wa(i).*dmuuea./rho +
F;

end

gn = peri_b4(gn);
```

```
function [ f ] = bounback( f )
%%%%%%%%%%%%%%%%%%%%%%%%%%%%%%%%%%%%%%%%%%%%%%%%%%%%%%%%%%%%%%%%%%%%%%%%%%%%
%%%
% bounback.m: modified bounce back
%
%%%%%%%%%%%%%%%%%%%%%%%%%%%%%%%%%%%%%%%%%%%%%%%%%%%%%%%%%%%%%%%%%%%%%%%%%%%%
%%%

% global variables
    global nx ny bh xxs yys xr xl yf yb;

    f(8, 2:(nx - 1), 2:(ny - 1), 1) = f(12, 2:(nx - 1), 2:(ny - 1),
1);
    f(4, 2:(nx - 1), 2:(ny - 1), 1) = f(7, 2:(nx - 1), 2:(ny - 1), 1);
    f(15, 2:(nx - 1), 2:(ny - 1), 1) = ...
        (f(2, 2:(nx - 1), 2:(ny - 1), 1) - ...
        f(5, 2:(nx - 1), 2:(ny - 1), 1) + ...
        f(3, 2:(nx - 1), 2:(ny - 1), 1) - ...
        f(6, 2:(nx - 1), 2:(ny - 1), 1))/2 + ...
        f(11, 2:(nx - 1), 2:(ny - 1), 1);
    f(9, 2:(nx - 1), 2:(ny - 1), 1) = ...
        (-f(3, 2:(nx - 1), 2:(ny - 1), 1) + ...
        f(6, 2:(nx - 1), 2:(ny - 1), 1))/2 + ...
        f(13, 2:(nx - 1), 2:(ny - 1), 1);
    f(10, 2:(nx - 1), 2:(ny - 1), 1) = ...
        (-f(2, 2:(nx - 1), 2:(ny - 1), 1) + ...
        f(5, 2:(nx - 1), 2:(ny - 1), 1))/2 + ...
        f(14, 2:(nx - 1), 2:(ny - 1), 1);

    f(10, xr, yf, bh + 1) = f(14, xr, yf, bh + 1);

    f(8, xr, yb, bh + 1) = f(12, xr, yb, bh + 1);

    f(9, xl, yb, bh + 1) = f(13, xl, yb, bh + 1);

    f(15, xl, yf, bh + 1) = f(11, xl, yf, bh + 1);

    f(4, xr, yf, 1) = f(7, xr, yf, 1);
    f(10, xr, yf, 1) = ...
        (f(3, xr, yf, 1) - f(6, xr, yf, 1) - ...
        f(2, xr, yf, 1) + f(5, xr, yf, 1))/2 + ...
        f(9, xr, yf, 1) + f(14, xr, yf, 1) - f(13, xr, yf, 1);
    f(15, xr, yf, 1) = ...
        (f(2, xr, yf, 1) - f(5, xr, yf, 1))/2 - ...
        f(9, xr, yf, 1) + f(13, xr, yf, 1) + f(11, xr, yf, 1);
    f(8, xr, yf, 1) = ...
        (-f(3, xr, yf, 1) + f(6, xr, yf, 1))/2 + ...
        f(12, xr, yf, 1) - f(9, xr, yf, 1) + f(13, xr, yf, 1);

    f(4, xr, yb, 1) = f(7, xr, yb, 1);
    f(10, xr, yb, 1) = ...
        (f(3, xr, yb, 1) - f(6, xr, yb, 1))/2 - ...
        f(15, xr, yb, 1) + f(11, xr, yb, 1) + f(14, xr, yb, 1);
    f(9, xr, yb, 1) = ...
        (f(2, xr, yb, 1) - f(5, xr, yb, 1))/2 - ...
        f(15, xr, yb, 1) + f(13, xr, yb, 1) + f(11, xr, yb, 1);
    f(8, xr, yb, 1) = ...
        (-f(2, xr, yb, 1) + f(5, xr, yb, 1) - ...
        f(3, xr, yb, 1) + f(6, xr, yb, 1))/2 + ...
        f(12, xr, yb, 1) + f(15, xr, yb, 1) - f(11, xr, yb, 1);
```

```
f(4, xl, yb, 1) =  f(7, xl, yb, 1);
f(15, xl, yb, 1) = ...
    (f(3, xl, yb, 1) - f(6, xl, yb, 1))/2 - ...
    f(10, xl, yb, 1) + f(11, xl, yb, 1) + f(14, xl, yb, 1);
f(9, xl, yb, 1) = ...
    (f(2, xl, yb, 1) - f(5, xl, yb, 1) - ...
    f(3, xl, yb, 1) + f(6, xl, yb, 1))/2 + ...
    f(10, xl, yb, 1) - f(14, xl, yb, 1) + f(13, xl, yb, 1);
f(8, xl, yb, 1) = ...
    (-f(2, xl, yb, 1) + f(5, xl, yb, 1))/2 + ...
    f(12, xl, yb, 1) - f(10, xl, yb, 1) + f(14, xl, yb, 1);

f(4, xl, yf, 1) = f(7, xl, yf, 1);
f(15, xl, yf, 1) = ...
    (f(3, xl, yf, 1) - f(6, xl, yf, 1) + ...
    f(2, xl, yf, 1) - f(5, xl, yf, 1))/2 + ...
    f(8, xl, yf, 1) - f(12, xl, yf, 1) + f(11, xl, yf, 1);
f(9, xl, yf, 1) = ...
    (-f(3, xl, yf, 1) + f(6, xl, yf, 1))/2 - ...
    f(8, xl, yf, 1) + f(12, xl, yf, 1) + f(13, xl, yf, 1);
f(10, xl, yf, 1) = ...
    (-f(2, xl, yf, 1) + f(5, xl, yf, 1))/2 - ...
    f(8, xl, yf, 1) + f(12, xl, yf, 1) + f(14, xl, yf, 1);

f(10, xr, yys, bh + 1) = f(14, xr, yys, bh + 1);
f(8, xr, yys, bh + 1) = f(12, xr, yys, bh + 1);

f(9, xxs, yb, bh + 1) = f(13, xxs, yb, bh + 1);
f(8, xxs, yb, bh + 1) = f(12, xxs, yb, bh + 1);

f(9, xl, yys, bh + 1) = f(13, xl, yys, bh + 1);
f(15, xl, yys, bh + 1) = f(11, xl, yys, bh + 1);

f(10, xxs, yf, bh + 1) = f(14, xxs, yf, bh + 1);
f(15, xxs, yf, bh + 1) = f(11, xxs, yf, bh + 1);

f(4, xr, yys, 1) = f(7, xr, yys, 1);
f(2, xr, yys, 1) = ...
    2*(-f(13, xr, yys, 1) + f(9, xr, yys, 1) + ...
    f(15, xr, yys, 1) - f(11, xr, yys, 1)) + f(5, xr, yys, 1);
f(10, xr, yys, 1) = ...
    (f(3, xr, yys, 1) - f(6, xr, yys, 1))/2 - ...
    f(15, xr, yys, 1) + f(11, xr, yys, 1) + f(14, xr, yys, 1);
f(8, xr, yys, 1) = ...
    (-f(3, xr, yys, 1) + f(6, xr, yys, 1))/2 + ...
    f(12, xr, yys, 1) - f(9, xr, yys, 1) + f(13, xr, yys, 1);

f(4, xxs, yb, 1) = f(7, xxs, yb, 1);
f(9, xxs, yb, 1) = ...
    (f(2, xxs, yb, 1) - f(5, xxs, yb, 1))/2 - ...
    f(15, xxs, yb, 1) + f(13, xxs, yb, 1) + f(11, xxs, yb, 1);
f(8, xxs, yb, 1) = ...
    (-f(2, xxs, yb, 1) + f(5, xxs, yb, 1))/2 + ...
    f(12, xxs, yb, 1) - f(10, xxs, yb, 1) + f(14, xxs, yb, 1);
f(3, xxs, yb, 1) = ...
    2*(-f(11, xxs, yb, 1) + f(15, xxs, yb, 1) + ...
    f(10, xxs, yb, 1) - f(14, xxs, yb, 1)) + f(6, xxs, yb, 1);

f(4, xl, yys, 1) = f(7, xl, yys, 1);
```

```
f(5, xl, yys, 1) = ...
    2*(-f(14, xl, yys, 1) + f(8, xl, yys, 1) + ...
    f(10, xl, yys, 1) - f(12, xl, yys, 1)) + f(2, xl, yys, 1);
f(15, xl, yys, 1) = ...
    (f(3, xl, yys, 1) - f(6, xl, yys, 1))/2 - ...
    f(10, xl, yys, 1) + f(11, xl, yys, 1) + f(14, xl, yys, 1);
f(9, xl, yys, 1) = ...
    (-f(3, xl, yys, 1) + f(6, xl, yys, 1))/2 + ...
    f(12, xl, yys, 1) - f(8, xl, yys, 1) + f(13, xl, yys, 1);

f(4, xxs, yf, 1) = f(7, xxs, yf, 1);
f(15, xxs, yf, 1) = ...
    (f(2, xxs, yf, 1) - f(5, xxs, yf, 1))/2 - ...
    f(9, xxs, yf, 1) + f(13, xxs, yf, 1) + f(11, xxs, yf, 1);
f(10, xxs, yf, 1) = ...
    (-f(2, xxs, yf, 1) + f(5, xxs, yf, 1))/2 - ...
    f(8, xxs, yf, 1) + f(12, xxs, yf, 1) + f(14, xxs, yf, 1);
f(6, xxs, yf, 1) = ...
    2*(-f(13, xxs, yf, 1) + f(8, xxs, yf, 1) + ...
    + f(9, xxs, yf, 1) - f(12, xxs, yf, 1)) + f(3, xxs, yf, 1);

f(13, xr, yf, 2:bh) = f(9, xr, yf, 2:bh);
f(10, xr, yf, 2:bh) = f(14, xr, yf, 2:bh);

f(8, xr, yb, 2:bh) = f(12, xr, yb, 2:bh);
f(11, xr, yb, 2:bh) = f(15, xr, yb, 2:bh);

f(9, xl, yb, 2:bh) = f(13, xl, yb, 2:bh);
f(14, xl, yb, 2:bh) = f(10, xl, yb, 2:bh);

f(12, xl, yf, 2:bh) = f(8, xl, yf, 2:bh);
f(15, xl, yf, 2:bh) = f(11, xl, yf, 2:bh);

f(2, xr, yys, 2:bh) = f(5, xr, yys, 2:bh);
f(8, xr, yys, 2:bh) = f(12, xr, yys, 2:bh);
f(11, xr, yys, 2:bh) = ...
    (-f(3, xr, yys, 2:bh) + f(6, xr, yys, 2:bh))/2 + ...
    f(15, xr, yys, 2:bh);
f(10, xr, yys, 2:bh) = ...
    (-f(4, xr, yys, 2:bh) + f(7, xr, yys, 2:bh))/2 + ...
    f(14, xr, yys, 2:bh);
f(13, xr, yys, 2:bh) = ...
    (f(3, xr, yys, 2:bh) - f(6, xr, yys, 2:bh) + ...
    f(4, xr, yys, 2:bh) - f(7, xr, yys, 2:bh))/2 + ...
    f(9, xr, yys, 2:bh);

f(3, xxs, yb, 2:bh) = f(6, xxs, yb, 2:bh);
f(8, xxs, yb, 2:bh) = f(12, xxs, yb, 2:bh);
f(9, xxs, yb, 2:bh) = ...
    (-f(4, xxs, yb, 2:bh) + f(7, xxs, yb, 2:bh))/2 + ...
    f(13, xxs, yb, 2:bh);
f(14, xxs, yb, 2:bh) = ...
    (f(2, xxs, yb, 2:bh) - f(5, xxs, yb, 2:bh) + ...
    f(4, xxs, yb, 2:bh) - f(7, xxs, yb, 2:bh))/2 + ...
    f(10, xxs, yb, 2:bh);
f(11, xxs, yb, 2:bh) = ...
    (-f(2, xxs, yb, 2:bh) + f(5, xxs, yb, 2:bh))/2 + ...
    f(15, xxs, yb, 2:bh);

f(5, xl, yys, 2:bh) = f(2, xl, yys, 2:bh);
```

```
    f(12, xl, yys, 2:bh) = f(8, xl, yys, 2:bh);
    f(15, xl, yys, 2:bh) = ...
        (f(3, xl, yys, 2:bh) - f(6, xl, yys, 2:bh))/2 + ...
        f(11, xl, yys, 2:bh);
    f(14, xl, yys, 2:bh) = ...
        (f(4, xl, yys, 2:bh) - f(7, xl, yys, 2:bh))/2 + ...
        f(10, xl, yys, 2:bh);
    f(9, xl, yys, 2:bh) = ...
        (-f(3, xl, yys, 2:bh) + f(6, xl, yys, 2:bh) - ...
        f(4, xl, yys, 2:bh) + f(7, xl, yys, 2:bh))/2 + ...
        f(13, xl, yys, 2:bh);

    f(12, xxs, yf, 2:bh) = f(8, xxs, yf, 2:bh);
    f(6, xxs, yf, 2:bh) = f(3, xxs, yf, 2:bh);
    f(15, xxs, yf, 2:bh) = ...
        (f(2, xxs, yf, 2:bh) - f(5, xxs, yf, 2:bh))/2 + ...
        f(11, xxs, yf, 2:bh);
    f(13, xxs, yf, 2:bh) = ...
        (f(4, xxs, yf, 2:bh) - f(7, xxs, yf, 2:bh))/2 + ...
        f(9, xxs, yf, 2:bh);
    f(10, xxs, yf, 2:bh) = ...
        (-f(4, xxs, yf, 2:bh) + f(7, xxs, yf, 2:bh) - ...
        f(2, xxs, yf, 2:bh) + f(5, xxs, yf, 2:bh))/2 + ...
        f(14, xxs, yf, 2:bh);

    f(8, xxs, yys, bh + 1) = f(12, xxs, yys, bh + 1);
    f(4, xxs, yys, bh + 1) = f(7, xxs, yys, bh + 1);
    f(15, xxs, yys, bh + 1) = ...
        (f(2, xxs, yys, bh + 1) - f(5, xxs, yys, bh + 1) + ...
        f(3, xxs, yys, bh + 1) - f(6, xxs, yys, bh + 1))/2 + ...
        f(11, xxs, yys, bh + 1);
    f(9, xxs, yys, bh + 1) = ...
        (-f(3, xxs, yys, bh + 1) + f(6, xxs, yys, bh + 1))/2 + ...
        f(13, xxs, yys, bh + 1);
    f(10, xxs, yys, bh + 1) = ...
        (-f(2, xxs, yys, bh + 1) + f(5, xxs, yys, bh + 1))/2 + ...
        f(14, xxs, yys, bh + 1);

end

function [ fb ] = peri_b4( fb )
%%%%%%%%%%%%%%%%%%%%%%%%%%%%%%%%%%%%%%%%%%%%%%%%%%%%%%%%%%%%%%%%%%%%%%%%%%%
peri_b.m: boundary conditions at the boundaries of cubic computational
domain for 4-D matrix
%%%%%%%%%%%%%%%%%%%%%%%%%%%%%%%%%%%%%%%%%%%%%%%%%%%%%%%%%%%%%%%%%%%%%%%%%%%

% global variables
global nx ny nz;

fb(:, 1, :, :) = fb(:, 2, :, :);
fb(:, nx, :, :) = fb([1 5 3 4 2 6 7 9 8 15 14 13 12 11 10], nx -
1, :, :);
fb(:, :, 1, :) = fb(:, :, 2, :);
fb(:, :, ny, :) = fb([1 2 6 4 5 3 7 10 15 8 13 14 11 12 9], :, ny -
1, :);
fb(:, :, :, nz) = fb(:, :, :, nz - 1);

end

function [ ux, uy, uz ] = iter_u( ux, uy, uz )
```

```
%%%%%%%%%%%%%%%%%%%%%%%%%%%%%%%%%%%%%%%%%%%%%%%%%%%%%%%%%%%%%%%%%%%%%%%%
iter_u.m: iteration for velocity correction
%%%%%%%%%%%%%%%%%%%%%%%%%%%%%%%%%%%%%%%%%%%%%%%%%%%%%%%%%%%%%%%%%%%%%%%%

% global variables
global nx ny nz nxyz solid solids p rho ep wa ea cycle;

% partial derivative
ux_x = fst_partd(1, ux);
uy_y = fst_partd(2, uy);
uz_z = fst_partd(3, uz);

% boundary conditions
ux_x = peri_b3vx(ux_x);
uy_y = peri_b3vy(uy_y);
uz_z = peri_b3vz(uz_z);

h   = reshape(wa'*reshape(p, 1, nxyz), 15, nx, ny, nz); % h_alpha
sGp = reshape(-(ux_x + uy_y + uz_z)/3, 1, nxyz);
nu  = reshape(ones(15, 1)*reshape(1./(1./rho + 0.5), 1, nxyz), ...
    15, nx, ny, nz);

t = 0;
%  iteration
while(1)
    t = t + 1;
    pn = p;
    hn = ...                    % collision
        h - nu.*(h - reshape(wa'*reshape(pn, 1, nxyz), 15, nx, ny,
nz)) ...
        + reshape(wa'*sGp, 15, nx, ny, nz);
%     for i = 1:15
%         h(i, :, :, :) = ...   % streaming
%             circshift(hn(i, :, :, :), [0, ea(1, i), ea(2, i), ea(3,
i)]);
%     end
    for i = 1:15
        h(i, 2:(nx - 1), 2:(ny - 1), 2:(nz - 1)) = ...
            hn(i, (2:(nx - 1)) - ea(1, i), (2:(ny - 1)) - ea(2, i), ...
            (2:(nz - 1)) - ea(3, i));
    end
    h = peri_b4(h);             % boundary condition
    p = reshape(sum(h), nx, ny, nz);
    p(solids) = 0;
    p = peri_b3s(p);
    m = max(max(max(abs((pn(2:(nx - 1), 2:(ny - 1), 2:(nz - 1)) - ...
        p(2:(nx - 1), 2:(ny - 1), 2:(nz - 1)))./ ...
        rho(2:(nx - 1), 2:(ny - 1), 2:(nz - 1))))));
    if m < ep
        break;
    end
%     disp([cycle, t]);
%     disp(m);
%     if (mod(t, 100)==1)
%         ptPlot = reshape(p(:, ny/2, :), nx, nz);
%         subplot(2, 2, 4);
%         imagesc(flipud(ptPlot'));
%         colorbar
%         title('Pressure iteration');
%         axis equal off; drawnow
```

```
%     end
end
disp([cycle, t]);
disp(m);

% velocity correction
p_x = fst_partd(1, p); % partial derivative of pressure
p_y = fst_partd(2, p);
p_z = fst_partd(3, p);

p_x = peri_b3vx(p_x);
p_y = peri_b3vy(p_y);
p_z = peri_b3vz(p_z);

ux = ux - p_x./rho;
uy = uy - p_y./rho;
uz = uz - p_z./rho;

ux(solid) = 0;
uy(solid) = 0;
uz(solid) = 0;

ux = peri_b3vx(ux);
uy = peri_b3vy(uy);
uz = peri_b3vz(uz);

end

function [ fst_p ] = fst_partd( I, La )
%%%%%%%%%%%%%%%%%%%%%%%%%%%%%%%%%%%%%%%%%%%%%%%%%%%%%%%%%%%%%%%%%%%%%%%%%%%%
fst_partd.m: calculate the first order partial derivative of variables
%%%%%%%%%%%%%%%%%%%%%%%%%%%%%%%%%%%%%%%%%%%%%%%%%%%%%%%%%%%%%%%%%%%%%%%%%%%%

% global variables
global nx ny nz bh xxs yys xr xl yf yb;

fst_p = zeros(nx, ny, nz);

switch I % select the direction: x, y or z
    case 1 % partial derivative in x direction
        fst_p(2:(nx - 1), 2:(ny - 1), 1:(nz - 1)) = ... % all points
            (La(3:nx, 2:(ny - 1), 1:(nz - 1)) - ...
            La(1:(nx - 2), 2:(ny - 1), 1:(nz - 1)))/2;
        fst_p(xr, yys, 1:bh) = ...                      % right surface
            La(xr + 1, yys, 1:bh) - La(xr, yys, 1:bh);
        fst_p(xl, yys, 1:bh) = ...                       % left surface
            La(xl, yys, 1:bh) - La(xl - 1, yys, 1:bh);

    case 2 % partial derivative in y direction
        fst_p(2:(nx - 1), 2:(ny - 1), 1:(nz - 1)) = ... % all points
            (La(2:(nx - 1), 3:ny, 1:(nz - 1)) - ...
            La(2:(nx - 1), 1:(ny - 2), 1:(nz - 1)))/2;
        fst_p(xxs, yb, 1:bh) = ...                       % back surface
            La(xxs, yb + 1, 1:bh) - La(xxs, yb, 1:bh);
        fst_p(xxs, yf, 1:bh) = ...                      % front surface
            La(xxs, yf, 1:bh) - La(xxs, yf - 1, 1:bh);

    case 3 % partial derivative in z direction
        fst_p(2:(nx - 1), 2:(ny - 1), 2:(nz - 1)) = ... % all points
```

```
            (La(2:(nx - 1), 2:(ny - 1), 3:nz) - ...
            La(2:(nx - 1), 2:(ny - 1), 1:(nz - 2)))/2;
        fst_p(2:(nx - 1), 2:(ny - 1), 1) = ...              % bottom
surface
            La(2:(nx - 1), 2:(ny - 1), 2) - ...
            La(2:(nx - 1), 2:(ny - 1), 1);
        fst_p(xxs, yys, bh + 1) = ...                       % up surface
            La(xxs, yys, bh + 2) - ...
            La(xxs, yys, bh + 1);

end

end

function [ snd_p ] = snd_partd( La )
%%%%%%%%%%%%%%%%%%%%%%%%%%%%%%%%%%%%%%%%%%%%%%%%%%%%%%%%%%%%%%%%%%%%%%%%
snd_partd.m: calculate the second order partial derivative of
variables
%%%%%%%%%%%%%%%%%%%%%%%%%%%%%%%%%%%%%%%%%%%%%%%%%%%%%%%%%%%%%%%%%%%%%%%%

% global variables
global nx ny nz bh xxs yys xr xl yf yb;

snd_p = zeros(nx, ny, nz);

snd_p(2:(nx - 1), 2:(ny - 1), 2:(nz - 1)) = ...     % all points
    La(3:nx, 2:(ny - 1), 2:(nz - 1)) + ...
    La(1:(nx - 2), 2:(ny - 1), 2:(nz - 1)) + ...
    La(2:(nx - 1), 3:ny, 2:(nz - 1)) + ...
    La(2:(nx - 1), 1:(ny - 2), 2:(nz - 1)) + ...
    La(2:(nx - 1), 2:(ny - 1), 3:nz) + ...
    La(2:(nx - 1), 2:(ny - 1), 1:(nz - 2)) - ...
    La(2:(nx - 1), 2:(ny - 1), 2:(nz - 1)).*6;

snd_p(2:(nx - 1), 2:(ny - 1), 1) = ...              % bottom surface
    La(3:nx, 2:(ny - 1), 1) + ...
    La(1:(nx - 2), 2:(ny - 1), 1) + ...
    La(2:(nx - 1), 3:ny, 1) + ...
    La(2:(nx - 1), 1:(ny - 2), 1) - ...
    La(2:(nx - 1), 2:(ny - 1), 1).*4 + ...
    La(2:(nx - 1), 2:(ny - 1), 1) + ...
    La(2:(nx - 1), 2:(ny - 1), 3) - ...
    La(2:(nx - 1), 2:(ny - 1), 2).*2;

snd_p(xr, yys, 1) = ...                             % right-down line
    La(xr + 2, yys, 1) + ...
    La(xr, yys, 1) - ...
    La(xr + 1, yys, 1).*2 + ...
    La(xr, yys + 1, 1) + ...
    La(xr, yys - 1, 1) - ...
    La(xr, yys, 1).*2 + ...
    La(xr, yys, 1) + ...
    La(xr, yys, 3) - ...
    La(xr, yys, 2).*2;

snd_p(xxs, yb, 1) = ...                             % back-down line
    La(xxs + 1, yb, 1) + ...
    La(xxs - 1, yb, 1) - ...
    La(xxs, yb, 1).*2 + ...
    La(xxs, yb + 2, 1) + ...
```

```
    La(xxs, yb, 1) - ...
    La(xxs, yb + 1, 1).*2 + ...
    La(xxs, yb, 1) + ...
    La(xxs, yb, 3) - ...
    La(xxs, yb, 2).*2;

snd_p(xl, yys, 1) = ...                                 % left-down line
    La(xl - 2, yys, 1) + ...
    La(xl, yys, 1) - ...
    La(xl - 1, yys, 1).*2 + ...
    La(xl, yys + 1, 1) + ...
    La(xl, yys - 1, 1) - ...
    La(xl, yys, 1).*2 + ...
    La(xl, yys, 1) + ...
    La(xl, yys, 3) - ...
    La(xl, yys, 2).*2;

snd_p(xxs, yf, 1) = ...                                 % front-down line
    La(xxs + 1, yf, 1) + ...
    La(xxs - 1, yf, 1) - ...
    La(xxs, yf, 1).*2 + ...
    La(xxs, yf - 2, 1) + ...
    La(xxs, yf, 1) - ...
    La(xxs, yf - 1, 1).*2 + ...
    La(xxs, yf, 1) + ...
    La(xxs, yf, 3) - ...
    La(xxs, yf, 2).*2;

snd_p(xr, yys, 2:bh) = ...                              % right surface
    La(xr + 2, yys, 2:bh) + ...
    La(xr, yys, 2:bh) - ...
    La(xr + 1, yys, 2:bh).*2 + ...
    La(xr, yys + 1, 2:bh) + ...
    La(xr, yys - 1, 2:bh) - ...
    La(xr, yys, 2:bh).*2 + ...
    La(xr, yys, (2:bh) + 1) + ...
    La(xr, yys, (2:bh) - 1) - ...
    La(xr, yys, 2:bh).*2;

snd_p(xxs, yb, 2:bh) = ...                              % back surface
    La(xxs + 1, yb, 2:bh) + ...
    La(xxs - 1, yb, 2:bh) - ...
    La(xxs, yb, 2:bh).*2 + ...
    La(xxs, yb + 2, 2:bh) + ...
    La(xxs, yb, 2:bh) - ...
    La(xxs, yb + 1, 2:bh).*2 + ...
    La(xxs, yb, (2:bh) + 1) + ...
    La(xxs, yb, (2:bh) - 1) - ...
    La(xxs, yb, 2:bh).*2;

snd_p(xl, yys, 2:bh) = ...                              % left surface
    La(xl - 2, yys, 2:bh) + ...
    La(xl, yys, 2:bh) - ...
    La(xl - 1, yys, 2:bh).*2 + ...
    La(xl, yys + 1, 2:bh) + ...
    La(xl, yys - 1, 2:bh) - ...
    La(xl, yys, 2:bh).*2 + ...
    La(xl, yys, (2:bh) + 1) + ...
    La(xl, yys, (2:bh) - 1) - ...
    La(xl, yys, 2:bh).*2;
```

```
snd_p(xxs, yf, 2:bh) = ...                              % front surface
    La(xxs + 1, yf, 2:bh) + ...
    La(xxs - 1, yf, 2:bh) - ...
    La(xxs, yf, 2:bh).*2 + ...
    La(xxs, yf - 2, 2:bh) + ...
    La(xxs, yf, 2:bh) - ...
    La(xxs, yf - 1, 2:bh).*2 + ...
    La(xxs, yf, (2:bh) + 1) + ...
    La(xxs, yf, (2:bh) - 1) - ...
    La(xxs, yf, 2:bh).*2;

snd_p(xxs, yys, bh + 1) = ...                           % up surface
    La(xxs + 1, yys, bh + 1) + ...
    La(xxs - 1, yys, bh + 1) + ...
    La(xxs, yys + 1, bh + 1) + ...
    La(xxs, yys - 1, bh + 1) - ...
    La(xxs, yys, bh + 1).*4 + ...
    La(xxs, yys, bh + 1) + ...
    La(xxs, yys, bh + 3) - ...
    La(xxs, yys, bh + 2).*2;

end

function [ fb ] = peri_b3s( fb )
%%%%%%%%%%%%%%%%%%%%%%%%%%%%%%%%%%%%%%%%%%%%%%%%%%%%%%%%%%%%%%%%%%%%%%%%%%%%
peri_b.m: boundary conditions at the boundaries of cubic computational
domain for 4-D matrix
%%%%%%%%%%%%%%%%%%%%%%%%%%%%%%%%%%%%%%%%%%%%%%%%%%%%%%%%%%%%%%%%%%%%%%%%%%%%

% global variables
global nx ny nz;

fb(:, :, nz) = fb(:, :, nz - 1);
fb(1, :, :) = fb(2, :, :);
fb(nx, :, :) = fb(nx - 1, :, :);
fb(:, 1, :) = fb(:, 2, :);
fb(:, ny, :) = fb(:, ny - 1, :);

end

function [ fb ] = peri_b3vx( fb )
%%%%%%%%%%%%%%%%%%%%%%%%%%%%%%%%%%%%%%%%%%%%%%%%%%%%%%%%%%%%%%%%%%%%%%%%%%%%
peri_b.m: boundary conditions at the boundaries of cubic computational
domain for 4-D matrix
%%%%%%%%%%%%%%%%%%%%%%%%%%%%%%%%%%%%%%%%%%%%%%%%%%%%%%%%%%%%%%%%%%%%%%%%%%%%

% global variables
global nx ny nz;

fb(1, :, :) = fb(2, :, :);
fb(nx, :, :) = -fb(nx - 1, :, :);
fb(:, 1, :) = fb(:, 2, :);
fb(:, ny, :) = fb(:, ny - 1, :);
fb(:, :, nz) = fb(:, :, nz - 1);

end

function [ fb ] = peri_b3vy( fb )
```

```
%%%%%%%%%%%%%%%%%%%%%%%%%%%%%%%%%%%%%%%%%%%%%%%%%%%%%%%%%%%%%%%%%%%%%%%%%%%%
peri_b.m: boundary conditions at the boundaries of cubic computational
domain for 4-D matrix
%%%%%%%%%%%%%%%%%%%%%%%%%%%%%%%%%%%%%%%%%%%%%%%%%%%%%%%%%%%%%%%%%%%%%%%%%%%%

% global variables
global nx ny nz;

fb(1, :, :) = fb(2, :, :);
fb(nx, :, :) = fb(nx - 1, :, :);
fb(:, 1, :) = fb(:, 2, :);
fb(:, ny, :) = -fb(:, ny - 1, :);
fb(:, :, nz) = fb(:, :, nz - 1);

end

function [ fb ] = peri_b3vz( fb )
%%%%%%%%%%%%%%%%%%%%%%%%%%%%%%%%%%%%%%%%%%%%%%%%%%%%%%%%%%%%%%%%%%%%%%%%%%%%
peri_b.m: boundary conditions at the boundaries of cubic computational
domain for 4-D matrix
%%%%%%%%%%%%%%%%%%%%%%%%%%%%%%%%%%%%%%%%%%%%%%%%%%%%%%%%%%%%%%%%%%%%%%%%%%%%

% global variables
global nx ny nz;

fb(nx, :, :) = fb(nx - 1, :, :);
fb(:, 1, :) = fb(:, 2, :);
fb(:, ny, :) = fb(:, ny - 1, :);
fb(:, :, nz) = fb(:, :, nz - 1);
fb(1, :, :) = fb(2, :, :);

end

%%%%%%%%%%%%%%%%%%%%%%%%%%%%%%%%%%%%%%%%%%%%%%%%%%%%%%%%%%%%%%%%%%%%%%%%%%%%
plot3D.m: for 3D view
%%%%%%%%%%%%%%%%%%%%%%%%%%%%%%%%%%%%%%%%%%%%%%%%%%%%%%%%%%%%%%%%%%%%%%%%%%%%

clear, clc

constant;
initialization;

load cyc860000;

phi = reshape(sum(f), nx, ny, nz);
phi(xxs, yys, 1:bh) = phi_g;
phi(:, :, nz - 1) = phi_g;
phi = peri_b3s(phi);

rho = (phi - phi_g)./(phi_l - phi_g).*(rho_l - rho_g) + rho_g;

airRegion  = phi < phi_g;      % air region
rho(airRegion) = rho_g;

liqRegion  = phi > phi_l;      % liquid region
rho(liqRegion) = rho_l;

rho(solid) = 0;
```

```
rho(:, :, 2) = 0;
rho = peri_b3s(rho);
rho = cat(1, rho(1:(nx - 1), :, :), flipud(rho(1:(nx - 1), :, :)));
rho = cat(2, rho(:, 1:(ny - 1), :), fliplr(rho(:, 1:(ny - 1), :)));


[X, Y, Z]  = ...     % get coordinate of matrix indices
                   meshgrid(1:72, 1:72, 1:75);
V = rho;
fv=isosurface(X,Y,Z,V,500);
p=patch(fv);
set(p,'FaceColor','red','EdgeColor','none');
view(3)
hold on
fv=isosurface(X,Y,Z,V,0);
p=patch(fv);
set(p,'FaceColor','blue','EdgeColor','none');
view(3)
camlight
lighting gouraud
xlabel('X');
ylabel('Y');
zlabel('Z');
axis equal tight
hold off

%%%%%%%%%%%%%%%%%%%%%%%%%%%%%%%%%%%%%%%%%%%%%%%%%%%%%%%%%%%%%%%%%%%%%%%%%%%%%%%
% plotrho.m: for 2D view
%%%%%%%%%%%%%%%%%%%%%%%%%%%%%%%%%%%%%%%%%%%%%%%%%%%%%%%%%%%%%%%%%%%%%%%%%%%%%%%

clear, clc

constant;
initialization;

load cyc860000;

phi = reshape(sum(f), nx, ny, nz);
phi(xxs, yys, 1:bh) = phi_g;
phi(:, :, nz - 1) = phi_g;
phi = peri_b3s(phi);

rho = (phi - phi_g)./(phi_l - phi_g).*(rho_l - rho_g) + rho_g;

airRegion  = phi < phi_g;     % air region
rho(airRegion) = rho_g;

liqRegion  = phi > phi_l;     % liquid region
rho(liqRegion) = rho_l;

rho(xxs, yys, 1:bh) = (rho_l + rho_g)/2;
rho = peri_b3s(rho);
rhoPlot = reshape(rho(:, ny, :), nx, nz);
rhoPlot = [rhoPlot(1:(nx - 1), :); flipud(rhoPlot(1:(nx - 1), :))];

imagesc(flipud(rhoPlot'));
colorbar;
axis equal;
hold on;
```

```
contour(flipud(rhoPlot'), 1000);
```

For “the big eat the small” problem

```
%%%%%%%%%%%%%%%%%%%%%%%%%%%%%%%%%%%%%%%%%%%%%%%%%%%%%%%%%%%%%%%%%%%%%%%%
shrinkage.m: the main program for simulating droplet motion on
surfaces with Shan Chen lattice Boltzmann model
%%%%%%%%%%%%%%%%%%%%%%%%%%%%%%%%%%%%%%%%%%%%%%%%%%%%%%%%%%%%%%%%%%%%%%%%

% Shan Chen Lattice Boltzmann sample in Matlab
% Copyright Wei Gong
% Address: Nottingham NG7 2RD, UK
% E-mail: wei.gong@nottingham.ac.uk
% Reference: Li, Qing, et al. "Lattice Boltzmann modeling of boiling
heat transfer: The boiling curve and the effects of wettability."
International Journal of Heat and Mass Transfer 85 (2015): 787-796.

clear, clc

global g;

format long;

t_max = single(1000001);     % maximum iteration
Nwri  = single(100);         % output data frequency

constant;          % constant setting
initialization;    % initial condition setting

% iteration (first 100 iters, without gravity)
g = single(0);
for time = single(1:100)

    disp(time);
    % streaming
    for i = 1:9
        ff(i, :, :) = ...
            circshift(fe(i, :, :), [0, ex(i), ey(i)]);
    end
    % Zou-He boundary conditions
    ff = zouhe(ff);
    % macro parameters
    macrop;
    % interaction forces
    [S, Fx, Fy] = forces( p, ff );
    % collision
    collision;
    % visualization
    visua;
end

% iteration (after 100 iters, with gravity)
% g = single(3e-5);
for time = single(101:t_max)

    if ismember(time, [102:100:20000])
```

```
        time;
    end

    disp(time);
    % streaming
    for i = 1:9
        ff(i, :, :) = ...
            circshift(fe(i, :, :), [0, ex(i), ey(i)]);
    end
    % Zou-He boundary conditions
    ff = zouhe(ff);
    % macro parameters
    macrop;
    % interaction forces
    [S, Fx, Fy] = forces( p, ff );
    % collision
    collision;
    % visualization
    visua;
end

%%%%%%%%%%%%%%%%%%%%%%%%%%%%%%%%%%%%%%%%%%%%%%%%%%%%%%%%%%%%%%%%%%%%%%%%%%%%%%%
constant.m: consant setting
%%%%%%%%%%%%%%%%%%%%%%%%%%%%%%%%%%%%%%%%%%%%%%%%%%%%%%%%%%%%%%%%%%%%%%%%%%%%%%%

global lx ly lxy R b cv rho rho_a lambda cc c_squ tau_e tau_t ux uy ...
    ex ey sigm ome Tc p;

% D2Q9 lattice constants
lx     = single(200);        % x length of computational domain
ly     = single(150);        % y length of computational domain
lxy    = lx*ly;
cc     = single(1);          % lattice speeds
c_squ  = cc*cc/3;            % square of sound speed
ex     = single([0 1 0 -1 0 1 -1 -1 1]);                  % velocity
scheme
ey     = single([0 0 1 0 -1 1 1 -1 -1]);
M      = single([ 1  1  1  1  1  1  1  1  1;
                 -4 -1 -1 -1 -1  2  2  2  2;
                  4 -2 -2 -2 -2  1  1  1  1;
                  0  1  0 -1  0  1 -1 -1  1;
                  0 -2  0  2  0  1 -1 -1  1;
                  0  0  1  0 -1  1  1 -1 -1;
                  0  0 -2  0  2  1  1 -1 -1;
                  0  1 -1  1 -1  0  0  0  0;
                  0  0  0  0  0  1 -1  1 -1]);
Minv   = single([ 4 -4  4  0  0  0  0  0  0;   % inverse matrix
                  4 -1 -2  6 -6  0  0  9  0;
                  4 -1 -2  0  0  6 -6 -9  0;
                  4 -1 -2 -6  6  0  0  9  0;
                  4 -1 -2  0  0 -6  6 -9  0;
                  4  2  1  6  3  6  3  0  9;
                  4  2  1 -6 -3  6  3  0 -9;
                  4  2  1 -6 -3 -6 -3  0  9;
                  4  2  1  6  3 -6 -3  0 -9])/36;
sigm   = single(1.2);

% parameters in YUAN C-S EOS
a   = single(3/49);
b   = single(2/21);
```

```
R   = single(1);
ome = single(0.344);
Tc  = 0.0778/0.45724*a/(b*R);    % critical temperature
Ts  = 0.86*Tc;                   % initial temperature
dT  = single(0.0137);
Tb  = Ts + dT;

% General flow parameters
rho_l  = single(6.4989);         % density
rho_v  = single(0.3797);
rho_a  = (rho_l + rho_v)/2;      % average density
nu_l   = single(0.1);            % viscosity
nu_v   = single(0.5/3);
tau_l  = 3*nu_l + 0.5;           % relaxation time
tau_v  = 3*nu_v + 0.5;
tau_e  = single(1/1.1);
tau_t  = single(1/1.1);
A     = single([1 1/tau_e 1/tau_t 1 1.1 1 1.1 1 1]'*ones(1, lxy));   %
orthogonal transformation matrix
cv     = single(6);                      % heat capacity
rho    = single(zeros(1, lxy));
p      = single(zeros(1, lxy));          % pressure
phi    = single(zeros(1, lxy));
ux     = single(zeros(1, lxy));          % velocity
uy     = single(zeros(1, lxy));
T      = single(zeros(1, lxy));          % temperature
Fx     = single(zeros(1, lxy));
Fy     = single(zeros(1, lxy));
lambda = single(zeros(lx, ly));          % heat conductivity
m      = single(zeros(9, lxy));
me     = single(zeros(9, lxy));
ff     = single(zeros(9, lx, ly));       % distribution function
fe     = single(zeros(9, lx, ly));       % distribution function

%%%%%%%%%%%%%%%%%%%%%%%%%%%%%%%%%%%%%%%%%%%%%%%%%%%%%%%%%%%%%%%%%%%%%%%%%%%%
initialization.m: initialize wall nodes and densities
%%%%%%%%%%%%%%%%%%%%%%%%%%%%%%%%%%%%%%%%%%%%%%%%%%%%%%%%%%%%%%%%%%%%%%%%%%%%

global obst obst_b obst_u;

[y, x]    = meshgrid(1:ly, 1:lx);

% wall nodes and fluid nodes
obst_b = (y == 1);
obst_u = (y == ly);
obst   = ((y == 1)|(y == ly));
flui   = (ismember(y, 2:(ly - 1)));

% liquid-vopor system
rho = reshape(rho, lx, ly);
rho(:, 1:10)  = rho_v;
rho(:, 14:108)   = rho_v;
rho(:, 112:ly)  = rho_v;
rho(:, 11:13)  = ones(lx, 1)*linspace(rho_v, rho_v, 3);
rho(:, 109:111)  = ones(lx, 1)*linspace(rho_v, rho_v, 3);

% % initial bubble
% rho(((x - lx/2).^2 + (y - ly/2).^2) < 60^2) = rho_l;
% rho(((x - lx/2).^2 + (y - ly/2).^2) < 50^2) = rho_v;
rho(((x - lx/4).^2 + (y - ly/2).^2) < 40^2) = rho_l;
```

```
rho(((x - 3*lx/4).^2 + (y - ly/2).^2) < 20^2) = rho_l;
% rho(((x - lx/2).^2 + (y - ly/3).^2) < 30^2) = rho_v;

rho = reshape(rho, 1, lxy);
T   = reshape(T, lx, ly);
T(obst_u)      = Ts;
T(flui)        = Ts;
T(obst_b)      = Ts; % for debug use without temperature field
% T(obst_b)      = Tb;
% % small temperature fluctuations
%   T(1:4:lx,   2)        =   T(1:4:lx,   2)   +   (linspace(0.3,   0,
length(1:4:lx)))'*Ts;
%   T(2:4:lx,   2)        =   T(2:4:lx,   2)   +   (linspace(0.3,   0,
length(2:4:lx)))'*Ts;
%   T(3:4:lx,   2)        =   T(3:4:lx,   2)   -   (linspace(0.3,   0,
length(3:4:lx)))'*Ts;
%   T(4:4:lx,   2)        =   T(4:4:lx,   2)   -   (linspace(0.3,   0,
length(4:4:lx)))'*Ts;
% T((round(lx/2) - 2):(round(lx/2) + 2), 1) = Tb;
T = reshape(T, 1, lxy);
A([8 9], (rho > rho_a))  = 1/tau_l;
A([8 9], (rho <= rho_a)) = 1/tau_v;
lambda = 0.028*reshape(rho, lx, ly);
phi       =  (1  +  (0.37464  +  1.54226*ome  -  0.26992*ome^2)*(1  -
sqrt(Ts/Tc))).^2;
p      = rho.*R.*Ts./(1 - b.*rho) - ...
       a.*phi.*rho.^2./(1 + 2.*b.*rho - b^2.*rho.^2);

% distribution function
u_squ = ux.^2 + uy.^2;
me(1, :) = ones(1, lxy);
me(2, :) = -2 + 3*u_squ;
me(3, :) = 1 - 3*u_squ;
me(4, :) = ux;
me(5, :) = -ux;
me(6, :) = uy;
me(7, :) = -uy;
me(8, :) = ux.^2 - uy.^2;
me(9, :) = ux.*uy;
me       = ones(9, 1)*rho.*me;

fe = reshape(Minv*me, 9, lx, ly);
ff = fe;

clear flui dT

function [ ff ] = zouhe( ff )
%%%%%%%%%%%%%%%%%%%%%%%%%%%%%%%%%%%%%%%%%%%%%%%%%%%%%%%%%%%%%%%%%%%%%%%%%%%
zouhe.m: Zou-He boundary condition
%%%%%%%%%%%%%%%%%%%%%%%%%%%%%%%%%%%%%%%%%%%%%%%%%%%%%%%%%%%%%%%%%%%%%%%%%%%

global obst_b obst_u

ff(3, obst_b) = ff(5, obst_b);
ff(6, obst_b) = ff(8, obst_b) + (ff(4, obst_b) - ff(2, obst_b))/2;
ff(7, obst_b) = ff(9, obst_b) + (ff(2, obst_b) - ff(4, obst_b))/2;

ff(5, obst_u) = ff(3, obst_u);
ff(8, obst_u) = ff(6, obst_u) + (ff(2, obst_u) - ff(4, obst_u))/2;
ff(9, obst_u) = ff(7, obst_u) + (ff(4, obst_u) - ff(2, obst_u))/2;
```

```
end

%%%%%%%%%%%%%%%%%%%%%%%%%%%%%%%%%%%%%%%%%%%%%%%%%%%%%%%%%%%%%%%%%%%%%%%%%%%%
macrop.m: calculate all the macro parameters
%%%%%%%%%%%%%%%%%%%%%%%%%%%%%%%%%%%%%%%%%%%%%%%%%%%%%%%%%%%%%%%%%%%%%%%%%%%%

% T      = RK(T, rho, ux, uy);
rho    = reshape(sum(ff), 1, lxy);
phi        =  (1  +  (0.37464  +  1.54226*ome  -  0.26992*ome^2)*(1  -
sqrt(T/Tc))).^2;
p      = rho.*R.*T./(1 - b.*rho) - ...
       a.*phi.*rho.^2./(1 + 2.*b.*rho - b.^2.*rho.^2);
lambda = 0.028*reshape(rho, lx, ly);

function [S, Fx, Fy] = forces( p, ff )
%%%%%%%%%%%%%%%%%%%%%%%%%%%%%%%%%%%%%%%%%%%%%%%%%%%%%%%%%%%%%%%%%%%%%%%%%%%%
forces.m: calculate the interaction force between fluid nodes and the
interaction force between solid and fluid nodes
%%%%%%%%%%%%%%%%%%%%%%%%%%%%%%%%%%%%%%%%%%%%%%%%%%%%%%%%%%%%%%%%%%%%%%%%%%%%

global lx ly lxy rho cc c_squ g tau_e tau_t ux uy ex ey sigm obst;

G = -1;
w = single([4/3 1/3 1/3 1/3 1/3 1/12 1/12 1/12 1/12]);
S = single(zeros(9, lxy));
psx_re = zeros(9, lx, ly);

psx = sqrt(abs(2.*(p - rho.*c_squ)./G./cc./cc));
psx = reshape(psx, lx, ly);
for i = 1:9
      psx_re(i, :, :) = circshift(psx, [-ex(i), -ey(i)]);
end
psx = reshape(psx, 1, lxy);
psx_re = reshape(psx_re, 9, lxy);
Fmx = -G.*psx.*(w*(psx_re.*(ex'*ones(1, lxy))));
Fmy = -G.*psx.*(w*(psx_re.*(ey'*ones(1, lxy))));
Fmx(obst) = 0;
Fmy(obst) = 0;

Fbx = zeros(1, lxy);
Fby = (rho - mean(rho)).*(-g);

Fx = Fmx + Fbx;
Fy = Fmy + Fby;

ux     = (ex*reshape(ff, 9, lxy) + Fx/2)./rho;
uy     = (ey*reshape(ff, 9, lxy) + Fy/2)./rho;
uF      = ux.*Fx + uy.*Fy;
Fm2     = Fmx.^2 + Fmy.^2;
psx2    = psx.^2;
S(1, :) = 0;
S(2, :) = 6*uF + sigm*Fm2./psx2./(tau_e - 0.5);
S(3, :) = -6*uF - sigm*Fm2./psx2./(tau_t - 0.5);
S(4, :) = Fx;
S(5, :) = -Fx;
S(6, :) = Fy;
S(7, :) = -Fy;
S(8, :) = 2*(ux.*Fx - uy.*Fy);
```

```
S(9, :) = ux.*Fy + uy.*Fx;

end

%%%%%%%%%%%%%%%%%%%%%%%%%%%%%%%%%%%%%%%%%%%%%%%%%%%%%%%%%%%%%%%%%%%%%%%%%%%%
collision.m: cillision step
%%%%%%%%%%%%%%%%%%%%%%%%%%%%%%%%%%%%%%%%%%%%%%%%%%%%%%%%%%%%%%%%%%%%%%%%%%%%

A([8 9], (rho > rho_a))  = 1/tau_l;
A([8 9], (rho <= rho_a)) = 1/tau_v;

u_squ = ux.^2 + uy.^2;
me(1, :) = ones(1, lxy);
me(2, :) = -2 + 3*u_squ;
me(3, :) = 1 - 3*u_squ;
me(4, :) = ux;
me(5, :) = -ux;
me(6, :) = uy;
me(7, :) = -uy;
me(8, :) = ux.^2 - uy.^2;
me(9, :) = ux.*uy;
me       = ones(9, 1)*rho.*me;

m  = M*reshape(ff, 9, lxy);
ms = m - A.*(m - me) + (1 - A/2).*S;

fe = reshape(Minv*ms, 9, lx, ly);
% fe(:, obst) = ff(:, obst); % no collision on boundary nodes

%%%%%%%%%%%%%%%%%%%%%%%%%%%%%%%%%%%%%%%%%%%%%%%%%%%%%%%%%%%%%%%%%%%%%%%%%%%%
visua.m: visualization
%%%%%%%%%%%%%%%%%%%%%%%%%%%%%%%%%%%%%%%%%%%%%%%%%%%%%%%%%%%%%%%%%%%%%%%%%%%%

if (mod(time, Nwri) == 1)
    save(['time', num2str(time)], 'fn');
    subplot(2, 2, 1);
    imagesc(flipud(reshape(rho, lx, ly)'));
    colorbar
    title('Density');
    axis equal off; drawnow
    subplot(2, 2, 2);
    quiver(x, y, reshape(ux, lx, ly), reshape(uy, lx, ly));
    colorbar
    title('Velocity');
    axis equal off; drawnow
    subplot(2, 2, 3);
    imagesc(flipud(reshape(p, lx, ly)'));
    colorbar
    title('Pressure');
    axis equal off; drawnow
    subplot(2, 2, 4);
    imagesc(flipud(reshape(T, lx, ly)'));
    colorbar
    title('Temperature');
    axis equal off; drawnow
    saveas(gcf,['time', num2str(time)],'png')
end

function [ T_new ] = RK( T_old, rho, ux, uy )
%%%%%%%%%%%%%%%%%%%%%%%%%%%%%%%%%%%%%%%%%%%%%%%%%%%%%%%%%%%%%%%%%%%%%%%%%%%%
```

```
RK.m: calculate the temperature distribution using fourth-order Runge-
Kutta scheme
%%%%%%%%%%%%%%%%%%%%%%%%%%%%%%%%%%%%%%%%%%%%%%%%%%%%%%%%%%%%%%%%%%%%%%%

global lx ly lxy R b cv lambda obst p;

ux     = reshape(ux, lx, ly);
uy     = reshape(uy, lx, ly);
T_old  = reshape(T_old, lx, ly);
rho    = reshape(rho, lx, ly);
p      = reshape(p, lx, ly);

h1 = K(T_old);
h1(obst) = 0;  % boundary temperature keep constant
h2 = K(T_old + h1/2);
h2(obst) = 0;
h3 = K(T_old + h2/2);
h3(obst) = 0;
h4 = K(T_old + h3);
h4(obst) = 0;
T_new = reshape(T_old + (h1 + 2*h2 + 2*h3 + h4)/6, 1, lxy);

    function Kt = K(T)
        Kt = -(ux.*partx(T) + uy.*party(T)) + part2(T)./rho./cv - ...
             (partx(ux) + party(uy)).*T.*R./cv./(1 - b.*rho);
%            Kt = -(ux.*partx(T) + uy.*party(T)) + part2(T)./rho./cv
- ...
%              (partx(ux) + party(uy))./cv./rho.*p;
    end

    function px = partx(fx)
        % df/dx
        fxl = circshift(fx, [1, 0]);
        fxr = circshift(fx, [-1, 0]);
        px  = (fxr - fxl)/2;
    end

    function py = party(fy)
        % df/dy
        fyu = circshift(fy, [0, -1]);
        fyd = circshift(fy, [0, 1]);
        py  = (fyu - fyd)/2;
    end

    function p2 = part2(f)
        % d(lambda*df/dx)/dx + d(lambda*df/dy)/dy
        fxl = circshift(f, [1, 0]);
        fxr = circshift(f, [-1, 0]);
        fyu = circshift(f, [0, -1]);
        fyd = circshift(f, [0, 1]);
        lal = circshift(lambda, [1, 0]);
        lar = circshift(lambda, [-1, 0]);
        lau = circshift(lambda, [0, -1]);
        lad = circshift(lambda, [0, 1]);
        p2  = (lambda + lar)./2.*(fxr - f) - ...
              (lambda + lal)./2.*(f - fxl) + ...
              (lambda + lau)./2.*(fyu - f) - ...
              (lambda + lad)./2.*(f - fyd);
    end
```

```
    p = reshape(p, 1, lxy);

end

%%%%%%%%%%%%%%%%%%%%%%%%%%%%%%%%%%%%%%%%%%%%%%%%%%%%%%%%%%%%%%%%%%%%%%%%%%%%
solveEOS.m: to solve the EOS for the coexisting densities
%%%%%%%%%%%%%%%%%%%%%%%%%%%%%%%%%%%%%%%%%%%%%%%%%%%%%%%%%%%%%%%%%%%%%%%%%%%%

clear, clc;

a   = 3/49;
b   = 2/21;
R   = 1;
ome = 0.344;
Tc  = 0.0778/0.45724*a/(b*R);
T   = 0.86*Tc;
V   = [0.15:0.0001:3.5];
phi = (1 + (0.37464 + 1.54226*ome - 0.26992*ome^2)*(1 - sqrt(T/Tc)))^2;
p   = R*T./(V - b) - a*phi./(V.^2 + 2*b.*V - b^2);

plot(V, p, 'b');
hold on;

title('Peng-Robinson EOS');
xlabel('Vm');
ylabel('P');

P = 0.025;
deltaP = 0.025/2;
S1 = 1;
S2 = 0;
S = (S1 - S2)/S1;
while(abs(S) > 0.00000001)
    Vm = solve('R*T/(Vm - b) - a*phi/(Vm^2 + 2*b*Vm - b^2) - P', 'Vm');
    % to get solutions
    Vm1 = double(vpa(real(subs(Vm(1)))));
    Vm2 = double(vpa(real(subs(Vm(2)))));
    Vm3 = double(vpa(real(subs(Vm(3)))));
    V1  = min([Vm1 Vm2 Vm3]);
    V2  = max([Vm1 Vm2 Vm3]);

    fcs = @(Vm) R*T./(Vm - b) - a*phi./(Vm.^2 + 2*b.*Vm - b^2);
    S1  = integral(fcs, V1, V2);
    % S1 is the integration area
    S2 = P*(V2 - V1);
    % S2 is a rectangular area
    if(S1 > S2)
        P = P + deltaP;
    else
        P = P - deltaP;
    end
    deltaP = deltaP/2;
    P
    S = (S1 - S2)/S1;
    S
end
P
V1
V2
rho1 = 1/V2
```

```
rho2 = 1/V1
plot(V, P*ones(1, length(V)), 'r');
plot([V1 V2], [P P], 'ko');
hold off;
```